EFFECT OF CRACKS ON THE TRANSPORT CHARACTERISTICS OF CRACKED CONCRETE

A Thesis Submitted to the College of

Graduate Studies and Research

In Partial Fulfillment of the Requirements

For the Degree of Master of Science

In the Department of Civil and Geological Engineering

University of Saskatchewan

Saskatoon

By

GANG LI

PERMISSION TO USE

In presenting this thesis in partial fulfilment of the requirements for a Postgraduate degree from the University of Saskatchewan, I agree that the Libraries of this University may make it freely available for inspection. I further agree that permission for copying of this thesis in any manner, in whole or in part, for scholarly purposes may be granted by the professor or professors who supervised my thesis work or, in their absence, by the Head of the Department or the Dean of the College in which my thesis work was done. It is understood that any copying or publication or use of this thesis or parts thereof for financial gain shall not be allowed without my written permission. It is also understood that due recognition shall be given to me and to the University of Saskatchewan in any scholarly use which may be made of any material in my thesis.

Requests for permission to copy or to make other use of material in this thesis in whole or part should be addressed to:

Head of the Department of Civil and Geological Engineering,

University of Saskatchewan

57 Campus Drive Saskatoon, Saskatchewan

Canada, S7N 5A9

ABSTRACT

Cracks in reinforced concrete structures can occur as a result of many phenomena such as fresh concrete bleeding, restrained shrinkage, thermal gradients, freeze-thaw cycles, alkali-aggregate reactions, and can also be induced by external loading. Thus, concrete becomes more vulnerable to the processes of deterioration by corrosion of reinforcement. The corrosion rate of cracked reinforced concrete in different exposure conditions has been studied by some researchers. However, it is not clear how the presence of cracks affects the corrosion-determining factors, which control the corrosion pattern at the crack. The objective of this project was to develop an understanding of the effects of cracking on the transport characteristics under wetting and drying cycles.

In this project, flexural loading induced natural cracks, and parallel-wall artificial cracks were studied. The infiltration properties of those cracks were evaluated by the tension infiltrometry technique. The saturation conditions around the crack were monitored with the Time Domain Reflectometry (TDR) technique. A numerical simulation was carried out to model the evolution of saturation in the cracked beams; in the model two crack modeling approaches were employed and compared.

The infiltration test showed that the presence of both artificial and natural cracks (0.3 mm and 1.0 mm) dramatically increased the permeability of concrete. The value of hydraulic conductivity was increased by up to 5 orders of magnitude at the location of the crack.

The evolution of water saturation of the cracked concrete under wetting and drying conditions was analyzed as colour-scaled images and the water saturation contours were compared for different crack openings. For the artificial crack samples, a deviation from the expected "perfectly symmetric" flow regime around a straight crack was observed. This was probably caused by the micro cracks induced during the shim pull-out process or a non-uniform compaction around the shim insertion. For the natural cracks, in the drying phase, smaller cracks seemed to have better water storage. Hence, the water saturation decreased at a slightly slower rate. The crack behaved like an open surface that was exposed to the environment. Application

of the same material properties to the open surface and the crack surface did not bring a large error for the water flow simulations.

A hysteresis phenomenon has been found during the identification of the Van Genuchten material parameters using an inverse modelling approach, with $K_s=5\times10^{-10}$ m/s, $\alpha=4.33\times10^{-4}$, for the wetting phase, n=1.32 and for the drying phase, n=2.0.

The simulation results suggest that for the simple flexural crack, the 1D crack line averaged from the front and back crack lines is capable of representing the crack in the wetting and drying scenario. The crack could be modelled as “free surface” or “equivalent porous medium”.

ACKNOWLEDGEMENT

I would like to express my gratitude to my supervisor, Dr. Moh Boulfiza for his persistent encouragement and valuable advice throughout my graduate studies. This research topic has been revised a couple of times with his help and finally has come to completion.

I really need to thank Dr. Leon Wegner and Dr. Lisa Feldman, the members of my advisory committee, for their expertise and valuable comments throughout my study and thesis writing.

I want to give my special thanks to Dr. Bing Si from the Department of Soil Science and Henry Chau from Soil Science Laboratory for their effective tutoring and suggestions on the Time Domain Reflectometry and infiltrometry technique facilitation.

I am grateful for the financial support provided by the China Scholarship Council and the Department of Civil and Geological Engineering, University of Saskatchewan.

Finally, I also would like to thank Brennan Pokoyoway, Structural Engineering Laboratory, Dale Pavier Geotechnical Laboratory, Daniel Vessey, Engineering Shop and my fellow graduate students. This project cannot possible be practically finished without their help.

Table of Contents

List of Figures

List of Tables

List of Symbols and Abbreviations

Symbols

J'_{sat}	Advective flux of chloride ions in saturated case, kg/m^{2}s
J'_{unsat}	Advective flux of chloride ions in unsaturated case, kg/m^{2}s
h_0	Suction at the disk surface, cm
h_0, h_1	Initial and final water heads, cm
p_l	Pressure of fluid, Pa
C_1, C_2	Parameters from the curve fitting of cumulative infiltration vs. the square root of time, ms^{-1} and ms$^{-1/2}$
C_u, C_d	Upstream and downstream chloride concentration, mole/m^3
D_a	Apparent diffusion coefficient, m^2/s
D_e	Chloride effective diffusion coefficient, m^2/s
D_{eff}	Effective chloride diffusion coefficient, m^2/s
H_p	Pressure head, m
K^{cr}	Hydraulic conductivity of a crack, cm/s
K_p	Geometric constant of a probe, m/cm
K_r^{cr}	Relative conductivity of a crack
L_a	Apparent probe length, m
M_c	Mass of container, g
M_{cds}	Mass of container and oven dry specimen, g
M_{cms}	Mass of container and moist specimen, g
M_s	Mass of oven dry specimen, ($M_s = M_{cds} - M_c$), g
M_w	Mass of water($M_w = M_{cms} - M_{cds}$), g
S_e	Effective saturation, 1
S_l	Saturation of the liquid phase,1
S_{lr}	Residual saturation, 1
V_0	Signal amplitude from the TDR instrument, V
V_∞	Signal amplitude at the distant point, V
V_R	Signal amplitude after reflection from the end of the probe, V
V_T	Signal amplitude after partial reflection from the beginning of the probe, V

V_p	Ratio of velocity of signal propagation
Z_L	Total impedance, Ω
Z_u	Characteristic impedance of a cable tester, Ω
f_T	Temperature correction coefficient
k_r	Relative permeability,1
k_s	Intrinsic permeability at full saturation, m^2
p_s	Saturated vapor pressure of water at a prescribed temperature,Pa
p_v	Partial pressure of water vapour in an air-water mixture, Pa
r_0	Disk radius of the infiltrometer, cm
w_0	Most probable value of crack width, m
w_s	The threshold width for saturation, m
θ_s	Volumetric water content at full saturation/ porosity, m^3/m^3
ρ_∞	Reflection coefficient at a distant point from the first reflection point
ρ_l	Density of fluid, kg/m^3
σ_a	Electrical conductivity of solution, dS/cm
σ_s	Electrical conductivity of solid phase, dS/cm
a,b	Empirical constant
C_{crit}	Critical chloride content, % mass of concrete/cement
d	Rod diameter, mm
g	Gravitational acceleration, m/s^2
I	Cumulative infiltration volume, ml
s	Rod spacing, mm
η	Fluid's dynamic viscosity, Pa·s
κ	Dielectric constant
Ψ	Matric potential
A	Cross sectional area of specimen, cm^2
A'	Cross sectional area of pipette, cm^2
C	Concentration of chloride, kg/m^3
D	Elevation head, m
Erf	Error function

J	Flux of chloride, kg/m^{2}s
K	Hydraulic conductivity, cm/s
L	Length of the probe, m
Q	The volume of water flow, cm^3
c	Speed of light in free space, m/s
k	Intrinsic permeability of the porous medium, m^2
m	Genuchten parameter m, 1
n	Genuchten parameter n, 1
p	Pressure, Pa
r	Distance from axis of rotation, cm
t	Time, s
v	Signal velocity, m/s
w	water content, %
$\boldsymbol{u}$	Darcy velocity or specific discharge vector, m/s
α	Genuchten parameter α, 1
θ	Volumetric water content, m^3/m^3
ω	Rotation speed, radians/s

Abbreviations

ACI	American Concrete Institute
ASTM	American Society for Testing and Materials
EDX	Energy Dispersive X-Ray
EMPA	Electron probe microanalysis
RCPT	Rapid Chloride Permeability Test
RH	Relative Humidity
SCC	Steady-state centrifugation
SCE	Standard Calomel Electrode
SD	Standard Deviation
SE	Standard Error
SEM	Scanning Electron microscope
SHE	Standard Hydrogen Electrode
SSD	Saturated Surface Dry
TDR	Time Domain Reflectometry

1 Introduction

Reinforced concrete is a versatile, economical, and durable building material, which has been successfully used in residential and industrial construction, and infrastructure. In most cases, reinforced concrete structures would be in good condition throughout their service life. However, in some cases, corrosion of the rebar may prematurely occur in reinforced concrete structures due to flawed design, improper material selection, poor construction, or severe environment (Bakhshi, 2011; Broomfield, 2007).

Reinforced concrete corrosion damage is a multibillion-dollar problem in North America and many other countries, as well as being a major factor to the deterioration of infrastructure. It is estimated that in the US, there is $150 billion lost because of corrosion damage on the highway bridges caused by deicing and sea salt (Broomfield, 2007). The annual cost of bridge deck repairs in the US is estimated at $50-$200 million with substructures and other components requiring $100 million a year and an additional $50-150 million a year on parking garages (Transportation Research Board, 1991). According to a recent study (Koch, 2002), the direct cost of corrosion was $8.3 billion a year on US highway bridges, within which $4.0 billion was spent on the capital cost and maintenance of reinforced concrete highway bridge decks and substructures. The indirect cost was 10 times more than the direct cost. Therefore, early prediction of corrosion has become a very valuable topic for construction engineers. A successful prediction would help to carry out preventive action and avoid unnecessary expensive repair and reconstruction.

Previous research on corrosion of steel reinforcement in concrete has primarily focused on the initiation and the propagation process of corrosion in uncracked concrete. The factors affecting corrosion and the techniques for determining the rate of corrosion of reinforced concrete have been extensively studied. In the early research, it was implicitly assumed that concrete cracking is the result of expansive stresses due to the formation of corrosion products. The alkalinity of concrete provides the microenvironment needed to generate and maintain a passive layer on steel, which protects it against corrosion. As a result, in the absence of cracks, the steel reinforcements in concrete structures are usually found to have a prolonged corrosion initiation period. This behaviour has been observed both in the field and in laboratory studies.

However, in the field, most cases of premature reinforced concrete corrosion are typically found associated with cracked concrete cover. Many phenomena, such as fresh concrete bleeding, restrained shrinkage, thermal gradients, freeze-thaw cycles, alkali-aggregate reactions, and external loading, may cause cracking problems in reinforced concrete structures. Thus, "concrete becomes more vulnerable to the processes of deterioration by corrosion of reinforcement as it gradually loses its water tightness during its service lifespan" (Gowripalan et al., 2000). In most cases, cracks do not affect the load-carrying capacity of the concrete structure (Mindess & Young, 1981); however, they may adversely affect its durability by providing easier access to oxygen, carbon dioxide, water and other aggressive agents, such as chloride ions in marine environments or from the use of deicing salts, which allows the corrosion process to initiate earlier and propagate much faster than in the case of uncracked concrete. This process is a typical reason why many reinforced concrete structures fail to reach their design life without intervention (repairs or rehabilitation).

The corrosion process of the rebar has two distinct periods: the initiation period and the propagation period (Ervin, 2007). The initiation period begins with the construction of a reinforced concrete (RC) structure and ends with the onset of the passive layer destruction and initiation of corrosion. Although only a little work has been carried out to study the corrosion of steel reinforcement in cracked concrete, the presence of a crack has been shown to affect the corrosion behaviour by changing the initiation period. The effect of macrocracks (0.1-0.8 mm wide at the exposed surface) on the chloride threshold level depends on the exposure conditions, the cover thickness, and the crack size (Pettersson, 1996). Macrocracks in concrete generally serve as fast pathways for the ingress of chlorides and lead to premature corrosion. Many findings (Alekseev et al., 1993; Frederiksen, 1993; Jaffer & Hansson, 2009; Pettersson, 1996) support this fact that cracking leads to a reduction of the initiation period of corrosion. The corrosion rate depends on the quality of concrete and the various environmental conditions to which the concrete structures are exposed: Alekseev et al. (1993) have found that the corrosion rate started high, but rapidly decreased and approached the active corrosion rate typically found in uncracked concrete. Frederiksen (1993) and Jaffer & Hansson (2009) observed low corrosion activity in cracks with widths up to 0.4 mm, for cross sectional cracks in the splash zone. Pettersson (1996) observed that, for high performance concrete with crack widths up to 0.8 mm

and a concrete cover of 30 mm, the active corrosion rate will become so small that it may be considered as practically harmless for partly submerged high performance concrete.

The limited amount of previous research on corrosion in cracked concrete has been restricted to measuring either potentials (for assessing the likelihood of corrosion) or corrosion rates in either field structures or preconditioned samples (often subjected to wetting/drying cycles) in the lab, without monitoring of the distribution around the crack of any of the environmental parameters known to be at the root of the corrosion process (water saturation, oxygen, and chlorides distribution levels). These parameters can affect not only the rate of corrosion but also the type of corrosion itself (microcell vs. macrocell). The saturation condition at the crack also affects the ingress of harmful chemical species, such as chlorides and oxygen. Although there seems to be a general consensus that the rate of steel corrosion at a crack location is determined by both the macrocell and microcell corrosion processes, a clear understanding of the role of each mechanism, its contribution to the total corrosion rate and its dependence on the local microenvironment (moisture, oxygen, and chlorides profiles) created by the very existence of a crack are not clear yet.

Most of the research that has been reported on how cracks affect the permeability of concrete treats cracks as a "smeared model" and evaluates the overall effect of cracks on the permeability. There was only limited amount of research where a crack is treated as a discrete object.

In some studies (Mangat & Gurusamy, 1987; Raharinaivo et al., 1986), the crack width and exposure conditions were clearly studied during loading but the samples were unloaded prior to salt exposure. It is possible that a crack may recover significantly after unloading. Since crack characteristics were not studied during the environmental exposure, there was no evidence supporting the relationship between crack width and the transport characteristics under exposure conditions.

In two other studies (Aldea et al., 1999; Wang et al., 1997), the cracks were generated in a concrete disk (short cylinder) and kept open throughout the permeability studies. However, the setting of the water penetration test was not very comparable with the water-penetrating-through-cracks. Those cracks were created on a concrete disk, and permeability was tested on the disk

surface, which is perpendicular to the crack lines. However, in real concrete structures it is more likely the case that water penetrates along the crack. In addition, the crack pattern does not resemble the crack in the real case. As pointed out by Wang et al., (1997), the cracks generated by the splitting tests may be identical in widths through the crack walls, while in real structures, the curvature of flexural members or the gradient of stress distribution will result in narrower crack widths at the level of the steel than at the surface. Furthermore, before the steady flow is formed, the water flow is not measured during the process of water penetration, so water flow in partially saturated concrete is not studied.

Therefore, the effects of cracks on the transport characteristics of cracked concrete needs to be studied with a more practical scenario where the crack lines are perpendicular to the surface and water penetrates and drains through the crack under wetting and drying phases.

1.1 Objectives

The objectives of the work in this study were to develop an understanding of the effects of cracking on the transport characteristics of two main chemical species (water and chloride ions) known to play major roles in the corrosion process of metallic reinforcements under wetting and drying phases.

The specific sub-objectives of this research project were:

(1) To measure the infiltration properties of different types of cracks, and find out how the types of cracks (artificial and natural cracks) and crack size affect the infiltration.

(2) To develop a Time Domain Reflectometry (TDR) test for monitoring the evolution of water saturation around the crack over time and find the effects of crack type and size on the water flow.

(3) To assess the possibility of monitoring the change in electrical conductivity to measure the chloride ions ingress into concrete using a TDR technique.

(4) To use the Finite Element Method to simulate the water penetration with different crack model formulations, and propose an efficient modelling approach.

In this project, two types of cracks were generated: load-induced flexural cracks, and artificial cracks (made by inserting plastic shims at the time of casting). The infiltration or suction properties of those cracks were evaluated by tension infiltrometry. The saturation condition, the moisture and salinity distribution of concrete at the crack were monitored with Time Domain Reflectometry (TDR).

1.2 Scope

In this project, only artificial cracks and load induced cracks by flexure were considered; no shrinkage or corrosion induced cracks were considered. Only static cracks were studied, and corrosion rates were not measured.

2 Literature review

2.1 Overview of the corrosion problem in reinforced concrete

Steel reinforcement embedded in concrete is protected from corrosion both by physical and chemical barriers (Aligizaki, 1999). Concrete contains a highly alkaline pore solution (pH 12~13) within its hardened cement paste. The pore solution can also contain a significant amount of dissolved oxygen, especially near the surface. The high alkalinity of the pore solution is due to the presence of sodium, potassium and calcium hydroxides produced by the hydration of cement particles with mixing water. In this alkaline environment, a protective iron oxide film forms and maintains the steel bars in passive condition with a very low corrosion rate. This protected state of steel in concrete against corrosion, known as passivity, requires a minimum pH value of approximately 11.5 to be maintained. The quality and the thickness of concrete cover have been shown to affect the stability of the passive layer around the reinforcement. The loss of passivity is often a result of the loss of alkalinity of the surrounding concrete due to carbonation or the presence of chloride ions.

2.1.1 Nature of steel corrosion in concrete

Concrete is a porous material with high alkalinity (pH about 12.5). In addition, concrete has a very complex microstructure of cement hydration products and porous structure with various sizes of pores. Mass transport of water and ions through concrete is a slow process usually governed by the diffusion mechanism (Gjorv et al., 1987). Corrosion of steel in concrete is an electrochemical reaction. The anodic reaction is the dissolution of iron into solution and the cathodic reaction is the reduction of oxygen (see Equation 2.1-2.2).

$$\text{Anodic reaction: } Fe(s) \rightarrow Fe^{2+} + 2e^{-} \qquad (2.1)$$

The standard electrode potential of this reaction is -0.44 V vs. SHE (Standard Hydrogen Electrode) or -0.682 V vs. SCE (Saturated Calomel Electrode).

$$\text{Cathodic reaction: } O_2(g) + 2H_2O + 4e^{-} \rightarrow 4(OH)^{-}(aq) \qquad (2.2)$$

The standard electrode potential of this reaction is 0.401 V (vs. SHE) or 0.159 V (vs. SCE). In the absence of oxygen and at a pH value less than 9, the reduction reaction occurs with an evolution of hydrogen as shown below:

$$2H_2O+2e^- \rightarrow H_2(g)+2(OH)^- \quad (2.3)$$

The standard electrode potential of this reaction is -0.828 V (vs. SHE) or -1.070 V (vs. SCE).

After oxidation, iron will change to different types of oxides, depending on the availability of oxygen, e.g., $Fe(OH)_3$, FeO(OH), HFeOOH, $HFeO_2$, $FeSO_3$, and especially black rust Fe_3O_4 as given in the following equations (Vesikari, 1988):

$$3Fe(s)+8(OH)^-(aq) \rightarrow Fe_3O_4+8e^- +4H_2O \quad (2.4)$$

$$4Fe(OH)_2+2H_2O+O_2(g) \rightarrow 4Fe(OH) \quad (2.5)$$

$$Fe^{2+}(aq)+2(OH)^- (aq) \rightarrow Fe(OH)_2 \quad (2.6)$$

There are three main types of iron corrosion products characterized by different colours (Aligizaki 1999): Red rust [$Fe(OH)_3$, Fe_2O_3], Black rust (Fe_3O_4) and Green rust (formed when chloride is present).

2.1.2 **Environmental factors that affect corrosion**

2.1.2.1 Carbonation

Carbonation leads to a decrease in the alkalinity of concrete, and hence causes an overall drop in the pH of the concrete surrounding the steel. Carbonation involves the diffusion of carbon dioxide (CO_2) from the surrounding air into concrete. The reaction of CO_2 with the cement paste compounds in the presence of water results in the consumption of $Ca(OH)_2$, and hence, an overall decrease in the pH (Schiessl, 1988). This is given as:

$$Ca(OH)_2 +CO_2 (g) \rightarrow CaCO_3 +H_2O \quad (2.7)$$

Since concrete is a porous material, the diffusion of CO_2 into concrete is determined by the pore structure of the hardened mortar matrix and the humidity inside concrete. If the concrete pores are dry, diffusion of CO_2 does not result in fast carbonation. On the other hand, if the pores are filled with water, carbonation does not take place because of the low diffusion rate of CO_2 in water (diffusion rate of CO_2 is about 10^4 times lower in water than in air). If the pores are only partly filled with water, which is normally the case close to the concrete surface, carbonation proceeds relatively fast to the depth at which the concrete pores are filled with water.

2.1.2.2 Chloride attack

In reinforced concrete structures, chloride ions come from two main sources. Firstly, they can come from the ingredients of the mix materials such as mixing water, aggregate, or admixture. Secondly, they can come from the environment due to the penetration of deicing salts, seawater etc. into concrete. A variety of models have been developed to describing the mechanisms of pitting corrosion. One of the most recent models, called point defect model (Figure 2.1), was developed by Macdonald (1992). It assumes that the chloride ions attack the passive layer, acting as a catalyst to corrosion. It causes the passive layer to break down and allow the corrosion process to take place prematurely.

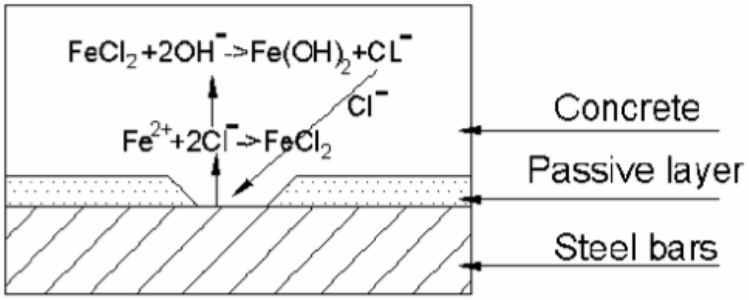

Figure 2.1 Point defect model of pitting corrosion (Macdonald, 1992)

Reinforcement corrosion in concrete can only occur when the chloride content at the steel surface has reached a certain threshold value (Page & Treadaway, 1982). In the literature, this value is often referred to as critical chloride content or chloride threshold value (C_{crit}). Angst et al. (2009) point out that there are two ways of defining C_{crit} (Figure 2.2): From a scientific point of

view, the critical chloride content is defined as the chloride content required for starting the depassivation of the steel (Definition 1 in Figure 2.2), while from a practical engineering point of view, C_{crit} is usually defined as the chloride content when visible or "beyond-acceptable" deterioration can be observed (Definition 2 in Figure 2.2). In the literature, findings of the critical chloride content by the two definitions are often mixed, and the value varies according to the materials and the exposure environmental conditions, such as electrochemical potential of steel alloy, pH value and oxygen content, which affect the steel bar corrosion. The reported critical concentration values vary within a large range. Angst et al. (2009) reviewed a large number of published results from 1955 to 2008, and found that the reported values range from 0.04 to 8.34% total chloride by weight of cement; the corresponding Cl^-/ OH^- ratios can vary from 0.01 to 45. Due to the very wide range of up to three orders of magnitude, it is not possible to select or assume a reliable chloride threshold value.

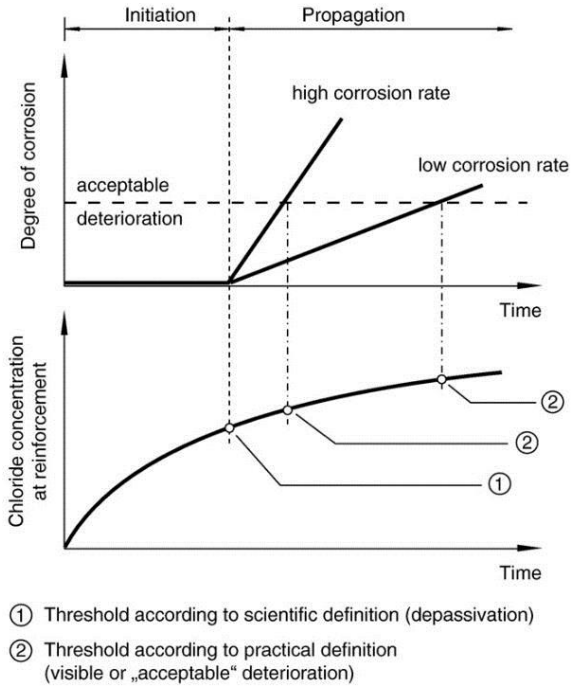

Figure 2.2 Definition of critical chloride content (Angst et al., 2009).

2.1.3 **Effect of cracks on corrosion**

Cracks are often induced in concrete structures by means of loads and other causes such as restrained shrinkage, thermal gradients, etc. They may adversely affect the durability by

providing easier access to oxygen, carbon dioxide, water and other aggressive agents such as chloride ions in marine environments or from the use of deicing salts, which allows the corrosion process to initiate earlier and propagate much faster and with a much higher corrosion rate than in the case of uncracked concrete.

When a crack occurs in reinforced concrete, the main transport mechanism for chloride ingress in cracked concrete then can change from diffusion to advection due to the relative ease of saturation of the crack. Therefore, the chloride will attack the passive layer of steel at the crack zone and lead to corrosion much earlier than away from the crack. Furthermore, a macrocell will be typically formed by a small anode at the crack, and a larger cathode around the crack.

The presence of a crack has been shown to bring spatial variations in the potential along the rebar (Arya & Vassie, 1995; Schiessl & Raupach, 1997). The effect of macrocracks (0.1-0.8 mm wide at surface) on the chloride threshold level depends on the exposure conditions, the cover thickness, and the crack size (Bi, 2009; Pettersson, 1996). However, there has been a big controversy as to whether the size of crack and corrosion rate are correlated; therefore, an important question that needs to be answered is whether cracks with greater size would cause faster corrosion.

Several researchers found little correlation between corrosion rates and crack width (Arya & Ofori-Darko, 1996; Schiessl, 1988; Schiessl & Raupach, 1997), while others have reported that there is a relationship between corrosion rate and crack width (Okada & Miyagawa, 1980).

Alekseev et al. (1993) reported that the main effect of macro cracks in submerged concrete is a reduction of the initiation time. Once active reinforcement corrosion was initiated, the corrosion rate changed over time; it started high, but rapidly decreased and approached the active corrosion rate typically found in uncracked concrete. According to his research, it was also found that the critical crack width for a given depth of pitting corrosion depends on the exposure conditions, the cover thickness, and the water/binder ratio.

For submerged high performance concrete, Pettersson (1996) found the chloride threshold value was reduced to almost zero for crack widths up to 0.8 mm and a concrete cover of 30 mm;

however, the active corrosion rate will become so small that it may be considered as practically harmless for partly submerged high performance concrete, as illustrated in Figure 2.3.

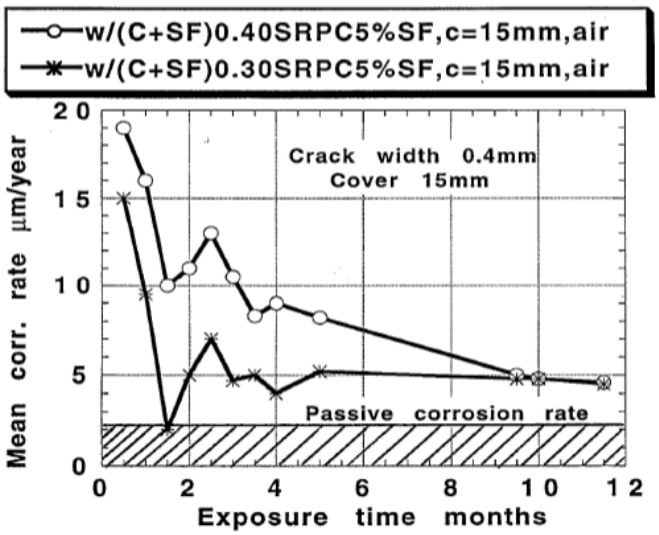

Figure 2.3 Corrosion rates measured by polarization resistance on field exposed concrete, splash zone, crack width 0.4 mm, 15 mm cover, w/(C+SF) = 0.30 and 0.40 (Pettersson, 1996).

Extensive field and laboratory studies on cracked concrete (water to binder ratio 0.50-0.70) have indicated that cracks up to 0.3 mm wide in concrete exposed to air had little negative effect on the long term corrosion depth (Moskvin, 1983; Schiessl, 1988; Schiessl & Raupach, 1997).

It has also been observed that the corrosion activity in cracked concrete depends on the exposure conditions and type of crack (Frederiksen, 1993; Jaffer & Hansson, 2009). They found only a low corrosion activity can be observed in cracks with widths up to 0.4 mm, for cross sectional cracks in the splash zone. Cracks in the concrete lead to an earlier initiation of corrosion, but not to a higher corrosion rate, in the long term.

According to Wilkins & Lawrence (1980), the cross sectional static cracks even up to 1 mm crack width would not lead to corrosion at a significant level in the case of submerged concrete. However, although corrosion can occur in thinner longitudinal cracks, it is not expected to be significant, if the crack widths are less than 0.6 mm (Jaffer & Hansson, 2009; Wilkins & Stillwell, 1986). For dynamic cracks where the crack width changes with loading, it has been

reported that the corrosion has prematurely taken place in cracks with crack widths as low as 0.1 mm (Hodgkiess et al., 1983).

In conclusion, the statement whether corrosion rate changes with crack width remains controversial. However, the concept of a "critical crack width" does not conflict with the idea that the corrosion rate is not dependent on the crack width within a certain crack width range. There is the possibility that the corrosion rate does not change with crack widths when the range of crack width does not cross (either smaller or greater than) the "critical width" and at the same time, if the crack width range crosses the "critical width", a different corrosion rate can be observed: a sample with a crack width larger than the "critical width" may have higher corrosion rate than a sample with the crack width smaller than the "critical width". The value of "critical crack width" varies from 0.1 mm to 1.0 mm (for static cracks, it is from 0.3 mm to 1.0 mm), depending on the concrete properties and the environmental conditions. With crack width below the "critical value", the corrosion rate remains so small that it would be considered non-harmful. However, when crack width exceeds the "critical value", corrosion becomes much faster and can lead to potential structural damage.

2.2 Water flow and chloride ions transport in porous media

2.2.1 Water flow

2.2.1.1 The pressure gradient formulation for water flow

Under saturated conditions, water flow, as an incompressible fluid in a saturated rigid porous medium, is driven by a pressure gradient according to Darcy's law. The net flux across a face of porous surface is

$$\boldsymbol{u} = -\left[\frac{k}{\eta}(\nabla \mathrm{p}_l + \rho_l g \nabla D)\right] \tag{2.8}$$

where $\boldsymbol{u}$ is Darcy velocity or specific discharge vector (m/s), k is the intrinsic permeability of the porous medium (m^2); η is the fluid's dynamic viscosity (Pa·s); p_l is the fluid's pressure (Pa) and ρ_l is its density (kg/m^3); g is the gravitational acceleration (m/s^2); and ∇D is a unit vector in the

vertical direction. The intrinsic permeability, k represents the resistance to flow over a representative volume of porous medium and depends only on the properties of the porous medium, while a similar concept called the coefficient of permeability or hydraulic conductivity, K, depends on both fluid and solid properties. K and k can be related as

$$\frac{k}{\eta} = \frac{K}{\rho_l g} \tag{2.9}$$

Darcy's Law can also be expressed in terms of pressure head with the relation of pressure p to the total hydraulic head H or the pressure head H_p:

$$\frac{p + \rho_l g D}{\rho_l g} = H = H_p + D \tag{2.10}$$

D is the elevation head and it has the direction over which g acts. When defined as vertical elevation, the horizontal gradients in D equal zero and vertical gradients in D equal one.

In many practical conditions, a porous medium like concrete is not fully saturated. The degree of saturation depends on the surrounding environmental moisture conditions and the saturation level in concrete. When concrete is not fully saturated, a negative capillary pressure develops and facilitates the absorption of water. Under such conditions the permeability becomes dependent on the water content. Darcy's law has been extended to describe water flow for this kind of problem in unsaturated porous media. One of the earliest and most widely used models for unsaturated porous media was developed by Richards and Lorenzo Adolph (1931) and is known as Richard's equation:

$$\boldsymbol{u} = -\left[\frac{k_s \cdot k_r}{\eta}(\nabla P_l + \rho_l g \nabla D)\right] \tag{2.11}$$

where k_s is the intrinsic permeability at full saturation and k_r is the relative permeability of liquid, defined as the ratio between the permeability at saturation θ, K ($\theta \leq \theta_s$) to K($\theta = \theta_s$), where θ_s is the saturation water content or the porosity.

The mass balance equation for an unsaturated porous medium is given by

$$\frac{\partial(\theta_s S_l)}{\partial t} = \nabla . \boldsymbol{u} \tag{2.12}$$

where S_l is the saturation of the liquid phase; t is the time.

Combining Equation 2.11 and Equation 2.12, Richard's equation becomes

$$\frac{\partial(\theta_s S_l)}{\partial t} = -\nabla\left[\frac{k_s \cdot k_r}{\mu_l}(\nabla P_l + \rho_l g \nabla D)\right] \tag{2.13}$$

Typically, Richard's equation has high nonlinearities due to the very sharp variations in the material and hydraulic properties at different saturation levels. To solve this equation, the constitutive relations between relative permeability k_r, saturation S_l, and the capillary pressure P_l are needed. A constitutive relationship or model that has been shown to work with concrete is given is van Genuchten- Mualem mode (Kumar, 2010 and Ramadani, 2013), given by Equation 2.14 to 2.16 (Mualem, 1976; Van Genuchten, 1980) :

$$k_r = \sqrt{S_e}\left[1 - \left(1 - \sqrt[m]{S_e}\right)^m\right]^2 \tag{2.14}$$

$$P_l = -\frac{1}{\alpha}\left[(S_e)^{-\frac{1}{m}} - 1\right]^{\frac{1}{n}} \tag{2.15}$$

$$S_e = \frac{S_l - S_{lr}}{1 - S_{lr}} \tag{2.16}$$

where, k_r is the relative permeability; S_e is the effective saturation of liquid, P_l is the capillary pressure of the porous medium, S_l is the degree of saturation in porous medium, and S_{lr} is the residual saturation of the porous medium; m, n and α are empirical parameters (m=1-1/n).

The pressure gradient formulation does provide a good way for the modelling of water flow in unsaturated porous media. However, the hydraulic conductivity data for concrete are not readily available because of the difficulties, such as time consuming water retention test, associated with the unsaturated hydraulic conductivity measurement, (Hall, 2009). Kumar (2010) and Ramadani (2013) adapted the centrifuge technique, which was originally used in soil science, to concrete

testing and it has been shown to be a relatively quick method for acquiring the saturated hydraulic conductivity.

The capillary pressure and saturation relationship is often called a retention curve. The retention curve can be experimentally determined by static saturation-capillary pressure data. A typical experiment of determining the saturation-capillary pressure relationship of soil or rock is shown in Figure 2.4. The soil sample will be allowed to reach equilibrium saturation under different capillary pressures, which are set by adjusting the water level in the tube. The sample is initially saturated with water, and subjected to a zero capillary pressure. Then the water level is decreased with increments to apply negative pressure to the sample causing water draining from the sample. During each water level step, when the equilibrium state is reached, saturation and capillary pressure is recorded. The experiment is terminated when porous plate reaches the air entry value. An imbibition (or wetting) capillary pressure curve is acquired by reversing the process (Bear et al., 2010).

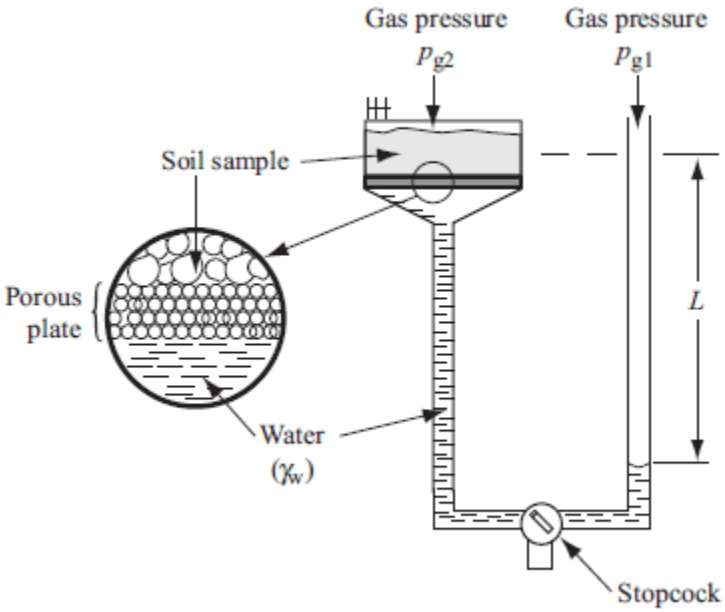

Figure 2.4 Laboratory determining the capillary pressure curve (Bear et al., 2010).

2.2.1.2 Hysteresis

Typically, the capillary pressure curve (or retention curve) obtained from draining (or drying) procedure differs from that obtained from imbibition (wetting) procedure (see Figure 2.5). This phenomenon where the capillary pressure curve depends on the history of drying and wetting of a sample is called hysteresis.

Hysteresis has been observed in the area of concrete research. Schneider (2011) estimated the Van Genuchten parameters of mortar and concrete by inverse modelling of the experimental data of absorbing and desorption pressure-water content curves. The results clearly show the divergence between the estimated Van Genuchten parameters for absorption and desorption (Figure 2.6).

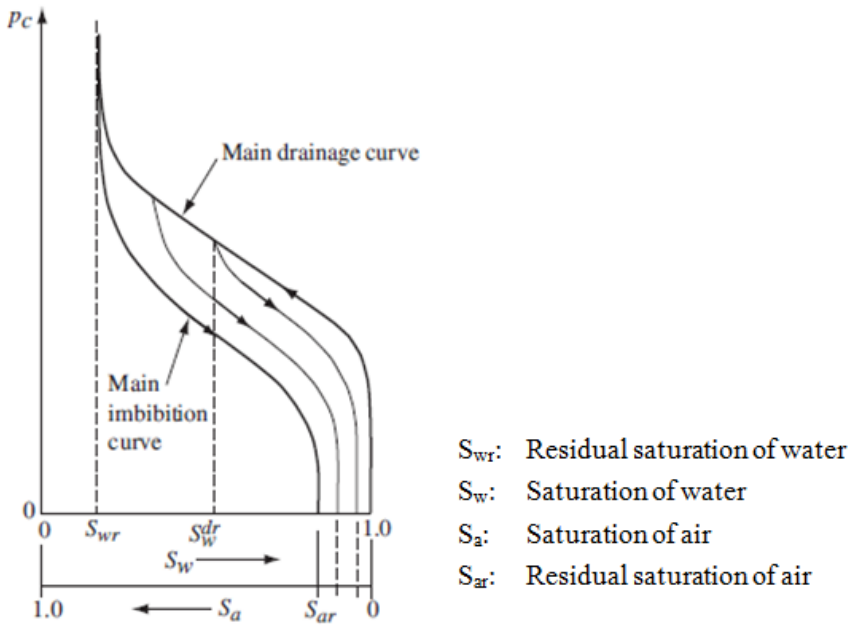

Figure 2.5 Hysteresis in capillary pressure curves (Bear et al., 2010).

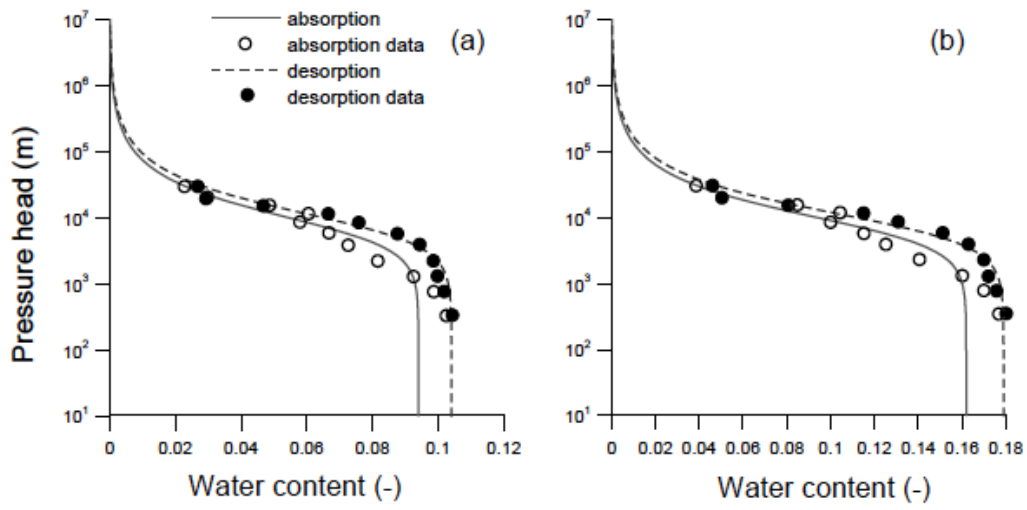

Figure 2.6 Water retention curves for concrete (a) and mortar (b) (Schneider, 2011).

This phenomenon is believed to be caused by four effects (Bear et al., 2010). Firstly, it is the inkbottle effect. This effect is caused by the shape of pore which has narrow and wide cross-sectional areas. During wetting and drying phases, at different saturation level, menisci in pores may have the same curvature, which give same capillary pressure at different water saturation level. Secondly, it is the raindrop effect. This effect is due to the fact that the contact angle at advancing trace is larger than that at resending trace and also the contact angle depends on the impurities, minerals on the surface, and whether the solid surface has been wetted by the fluid or not. Thirdly, the hysteresis may be caused by the entrapment of air in wetting after previous drying cycle. Finally the deformation of the material during wetting and drying may also contribute to hysteresis, especially in unconsolidated porous media.

2.2.2 **Chloride ion transport**

Chloride ions penetrate into concrete by advection and diffusion. In the case of saturated concrete with no flow, chloride ions penetrate concrete due to diffusion, which is driven by the concentration gradient. Diffusion is usually the dominant transport mechanism for chloride ion ingress in fully saturated concrete. Under unsaturated conditions, however, advection plays a

major role in chloride ion transport. The advection is driven by capillary suction and causes the liquid that may contain chloride ions to move into the unsaturated pore structure of concrete.

2.2.2.1 Chloride transport by diffusion

Chloride ions move in porous media due to a concentration gradient within the pore solution. Under steady state conditions, this mechanism is described by Fick's first law.

$$J = -D_{eff}\frac{\partial C}{\partial x} \tag{2.17}$$

where J is the flux of chloride due to diffusion in the x direction (kg/m^{2}s); D_{eff} is the effective chloride diffusion coefficient (m^2/s); C is the concentration of chloride (kg/m^3) at depth x.

Under unsteady conditions, the concentration of chloride ions in the pore solution changes with time (transient condition). The mechanism of ion transport is described by Fick's Second Law, which applies the law of mass conservation to the ion transport process.

$$\frac{\partial(\theta_s S_l C)}{\partial t} = -\frac{\partial J}{\partial x} \tag{2.18}$$

$$\frac{\partial(\theta_s S_l C)}{\partial t} = \frac{\partial}{\partial x}\left(D_{eff}\frac{\partial C}{\partial x}\right) \tag{2.19}$$

where θ_s is porosity; S_l is liquid saturation. The term on the left hand side represents the rate at which the chloride ion concentration is changing inside the concrete, and the term on the right hand side represents divergence of chloride flux in pure solution.

2.2.2.2 Chloride transport by advection

The chloride ion transported by advection is essentially the movement of chloride ions associated with the water flow. Therefore the flux of chloride ions can be mathematically expressed as

$$J'_{sat} = C \cdot u \tag{2.20}$$

$$J'_{unsat} = C \cdot u_l \tag{2.21}$$

where J'_{sat} is the advective flux of chloride ions (kg/m^{2}s) in saturated case, J'_{unsat} is the advective flux of chloride ions (kg/m^{2}s) in unsaturated case, u is the water flux given by Equation 2.8 and u_l is the water flux given by Equation 2.11.

2.3 Effect of cracks on water flow and the transport of chloride ions in concrete

Despite the accepted fact that cracks play a major role in the long term performance of reinforced concrete, only a limited amount of research has been reported on how cracks affect the permeability of concrete.

Although in some studies (Mangat & Gurusamy, 1987; Raharinaivo et al., 1986) the crack width and exposure conditions were clearly stated during loading, the samples were unloaded prior to salt exposure. It is possible that a crack may recover significantly after unloading and during the environmental exposure, the characteristics of cracks in these studies were no longer the same size as they were when freshly induced. Therefore, there was no evidence supporting the relationship between crack width and transport characteristics in exposure conditions.

Therefore, only studies that have clearly stated the characteristics of cracks and their effect on the transport of common species, such as water and chloride will be summarized below.

2.3.1 **Water flow**

Aldea et al. (1999) and Wang et al. (1997) designed a feedback controlled splitting test, as illustrated in Figure 2.7. This experimental approach allows loading and unloading of a compression force according to the transvere displacement that monitors the opening size of cracks. In those studies, the longitudinal cracks were successfully created with different crack widths ranging from 50-900 micrometers.

Wang et al. (1997) have found that water permeability of concrete increases with crack width. The degree of the permeability increase depends on the size of the crack opening. It has been also found that there are three ranges of crack widths, in which the crack width has a different influence pattern: when a crack opening displacement was less than 50 micrometers, the crack opening had little effect on concrete permeability; when the crack opening displacement

increased from 50 to 200 micrometers, concrete permeability dramatically increased nonlinearly; when the crack opening displacement was larger than 200 micrometers, the rate of water permeability increase became linear and slower.

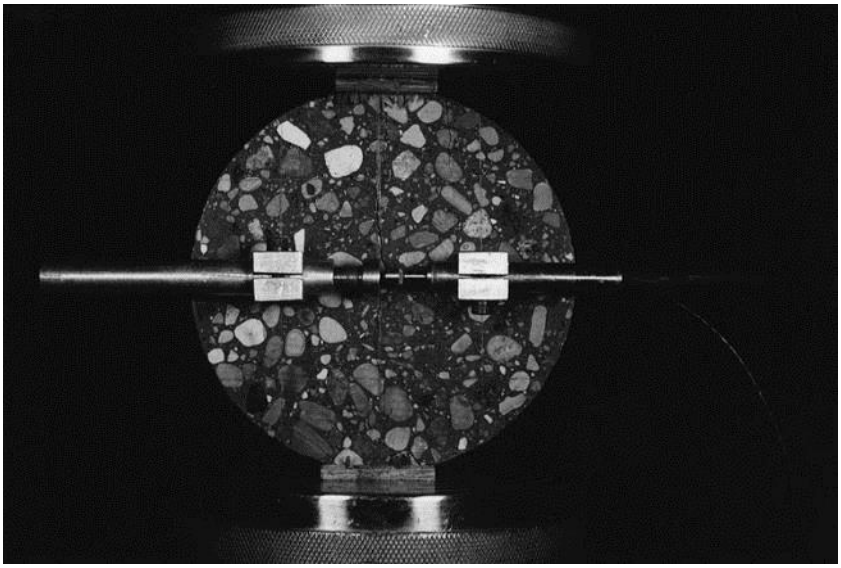

Figure 2.7 Feedback controlled splitting test (Aldea et al., 1999)

Aldea et al. (1999) generated similar cracks using a feed-back controlled splitting test and similar results were found: the water permeability of cracked normal strength concrete (NSC) and high strength concrete (HSC) significantly increased with increasing crack width. For cracks less than 200 micrometers, the permeability coefficient increased within an order of magnitude compared with that corresponding to uncracked state, while for crack widths greater than 200 micrometers, the water permeability increased rapidly. For the entire cracking range HSC showed lower permeability coefficients than NSC.

However, these two studies (Aldea et al., 1999; Wang et al., 1997) have some limitations. The setting of the water penetration test was not precisely comparable with the water-penetrating-through-cracks problem. Those cracks were created on a concrete disk, and permeability was tested on the disk surface, which is perpendicular to the crack lines. In the real concrete structure, it is more likely the case that water penetrates along the crack.

In addition, the crack pattern does not resemble the crack in the real case and it was also pointed out by Wang et al. (1997) that the cracks generated by the splitting tests may be identical in widths through the crack walls. However, in the actual structures, the curvature of flexural members, or the gradient of stress distribution will result in narrower crack widths at the level of the steel than at the surface. Furthermore, the water flow was not measured before the concrete reached full saturation.

2.3.2 **Chloride ions**

Aldea et al. (1999) applied the Rapid Chloride Permeability Test (RCPT) to cracked concrete where the crack was generated from a feedback controlled splitting test. The RCPT test results showed that both initial current and total charge increases with increasing the crack width suggesting that the permeability of chloride increases with crack width. However, for cracks up to 400 micrometers, the high strength concrete (69-79 MPa) can still be defined as very low chloride permeability concrete according to ASTM C 1202-94.

Rodriguez & Hooton (2003) examined chloride ingress influenced by artificially created, parallel-wall cracks with widths ranging from 0.06 to 0.74 mm and different crack wall surface roughness (brought by sawing and splitting). Chloride bulk diffusion test and Scanning Electron microscope/Energy Dispersive Using X-Ray (SEMEDX) analysis was employed to determine the concentration of chloride ions at the vicinity of cracks in concrete samples. It was concluded that the chloride diffusion in concrete was independent of either crack width or the crack wall roughness. The parallel-wall cracks were found to behave like a free concrete surface. A two dimensional diffusion profile of chloride ingress was observed.

Electron probe microanalysis (EMPA) and colourimetric tests (Win et al., 2004) were performed on cracked specimens with a single crack of 0.2 mm crack width, which were later exposed to NaCl solution at a temperature of 20 ℃ and a relative humidity of 60% for two months. It was found that for higher w/c mixes of 0.45 and 0.65, the penetration depth of chlorides from the surface of the cracks was equal to or slightly higher than that from the exposed free surface. The transportation of Cl^- ions was strongly influenced by the bulk movement of the solution through

the crack and within the concrete when the samples were not fully saturated and the capillary suction was taking place.

Ismail et al. (2004) applied an expansion core (Figure 2.8) to create the simulated cracks with crack openings ranging from 6 to 325 μm. The chloride content profiles along the depth from the crack surfaces were determined by grinding the sampling powders at different depths from the crack surface.

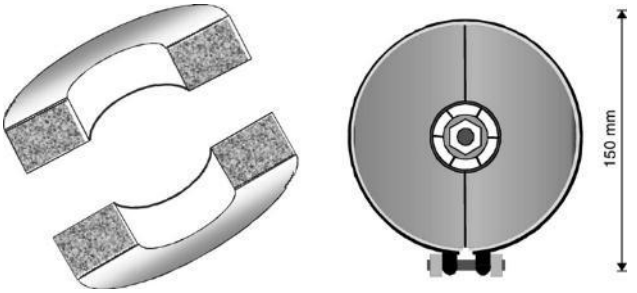

Figure 2.8 Crack generated by expansion core sample (Ismail et al., 2004).

Cracks smaller than 55 μm had little influence on the penetration of chlorides in the short period of the reported study (one month). The chloride concentration within 5 mm near the crack in mortar sample observed by Ismail et al. (2004) was much smaller than that observed by Win et al. (2004) around the same crack width even though a salt solution with much higher concentration (32.99g/L versus 3% by weight) was used.

Gowripalan et al. (2000) created flexural cracks with three-point loading and maintained them to open up to 0.3 mm. Beams were ponded in salt solution for 300 days. The experiment showed that the apparent chloride diffusion coefficient is greater in the tensile than in the compressive zone. However, no relationship between ingress of chloride ions and time was studied.

Summary

From the research reviewed above, it can be concluded that chloride penetration increases with increased water/cement ratio and crack width. However, quantification of this effect in the

literature depends on the exposure conditions, materials, and methods used. The critical crack width below which cracks have little influence on the Cl^- ingress in short periods (one month) is very small (less than 55 μm) and there is no dramatic difference regarding the effect of crack width on the chloride ingress even after long periods (more than one year). It has also been shown that by increasing the water/cement ratio [from 0.4 (Rodriguez, 2003) to 0.45 or 0.65 (Win et al., 2004)], crack surface starts to increase its effect of accelerating the chloride penetration.

Despite the existence of a number of studies on Cl^- ingress in cracked concrete, considering a variety of variables including crack width, crack type, material properties, exposure conditions, two questions still remain unanswered: (1) How much does the presence of a crack contribute to the unsaturated-stage chloride ingress in terms of bulk solution movement (advection)? (2) How deep does the influence of crack become insignificant (i.e. what is the zone of influence)?

2.4 Experimental techniques of water and chloride ions in concrete

In this section, the experimental techniques of testing water and chloride content are reviewed. The main discussion will focus on the theory of these techniques and the procedures will be briefly introduced. The application of time domain reflectometry (TDR) will be reviewed in the next section.

2.4.1 Tests for water content and flow properties

Water content changes in concrete due to evaporation and water penetration. In order to have a knowledge of how water moves and how fast water penetrates into concrete, a number of testing approaches have been developed to test the water content and permeability properties of a concrete sample for cracked or uncracked and saturated or unsaturated conditions.

There are a limited number of methods that have been used to measure the water content of concrete samples. Very limited literature can be found on the testing of water content profiles during water penetration. However, water permeability is extensively studied and the standard and widely used experimental approaches are very developed. In this section, experiments regarding water content and water permeability will be summarized.

2.4.1.1 Water content test

Water content can be measured by following ASTM D2216-10. A test specimen is oven- dried to a constant mass at a temperature of 110±5°C. The loss of mass is considered to be water. The water content is calculated as follows:

$$w = \left[\frac{M_{cms} - M_{cds}}{M_{cds} - M_c}\right] = M_w / M_s \tag{2.22}$$

w: water content, %,

M_{cms}: mass of container and moist specimen, g,

M_{cds}: mass of container and oven dry specimen, g,

M_c: mass of container, g,

M_w: mass of water($M_w = M_{cms} - M_{cds}$), g, and

M_s: mass of oven dry specimen, ($M_s = M_{cds} - M_c$), g.

2.4.1.2 Cracked concrete water permeability test

Water permeability tests are performed on the cracked specimens as mentioned in the studies by (Wang et al., 1997). This method aims for testing the permeability under saturated conditions.

The first step is sample preparation. The specimens are first vacuumed for 3 hours in a desiccator and then for another hour under water. After the saturated vacuum, the specimens were remained in the desiccator and soaked for at least 12 hours.

The test setup is illustrated in Figure 2.9. Water is filled in the pipette. The water permeates through the specimen due to the pressure head. The water level drop was measured at regular time intervals according to the water flow rate of the specimen, normally once a day. After each measurement, water in the pipette was restored to the original level.

The test results are plotted in the form of a curve of the cumulative water flow versus time. When the water flow becomes steady, the curve becomes linear and Darcy's law can be applied to the permeability calculation.

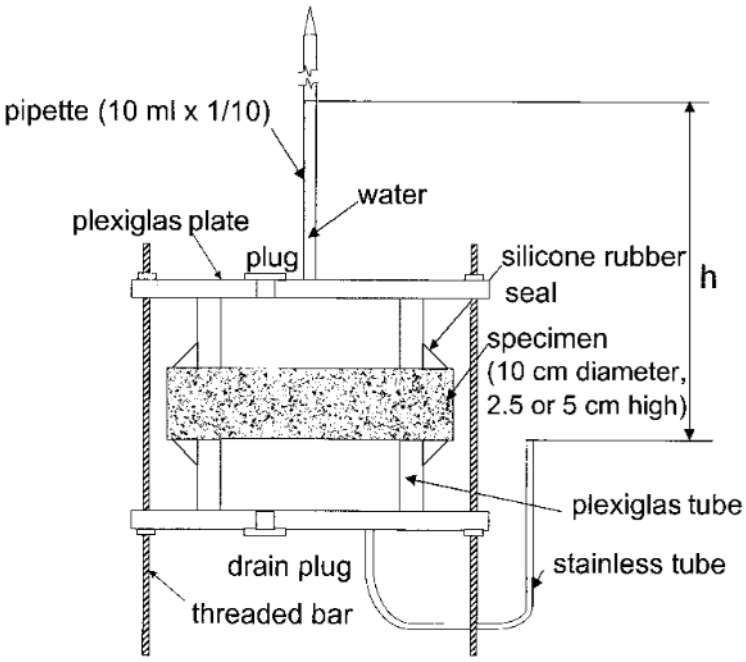

Figure 2.9 Water permeability tests (Wang et al., 1997).

The coefficient of permeability (k, in cm/sec) based on Darcy's law for a falling water head can be calculated according to Equation 2.25 (Cemica, 1995):

$$\frac{dQ}{dt} = -\frac{A'dh}{dt} = kA\frac{h}{L} \tag{2.23}$$

$$-\frac{dh}{h} = k\frac{Ah}{A'L}dt \tag{2.24}$$

Integrate h from h_0 to h_1, t from 0 to t.

$$k = \frac{A'L}{At} ln\frac{h_0}{h_1} \tag{2.25}$$

where,

A' is the cross sectional area of pipette, cm^2;
A is cross sectional area of specimen, cm^2;
h_0 and h_1 are initial and final water heads, cm;

k is permeability coefficient, cm/s;
L is the specimen thickness, cm;
Q is the volume of water flow, cm^3;
t is the time, s.

2.4.1.3 Centrifuge Technique

Darcy's Law determines the water flux density by the product of hydraulic conductivity and the fluid driving force. Under unsaturated conditions, the advective flow will be affected by the capillary suction from the unsaturated part of the sample and that is why it is required to wait until the steady flow can be achieved. Only the data from the steady-flow stage is considered in water permeability calculation when using this testing method.

The Steady-State Centrifugation is used for determining unsaturated and saturated hydraulic conductivity in porous media (ASTM D6527-00). Instead of using the gravitational force, fluid can be forced though a specimen with a constant flux or steady state flow during centrifugation of the specimen. In steady-state centrifugation (SSC) (Figure 2.10), the driving force can be determined by imposing a certain rotation speed on the specimen. The water flux density is determined by controlling the flow rate into the specimen by a constant-flow pump which evenly disperse the water flow front over the specimen. By these settings, when the specimen reaches the steady state, the hydraulic conductivity can be determined by the water flux density and driving force.

When the matric potential gradient is much lower than the acceleration, $d\Psi/dr \ll \rho\omega^2 r$, Darcy's Law becomes

$$K = q/[\rho\omega^2 r] \tag{2.26}$$

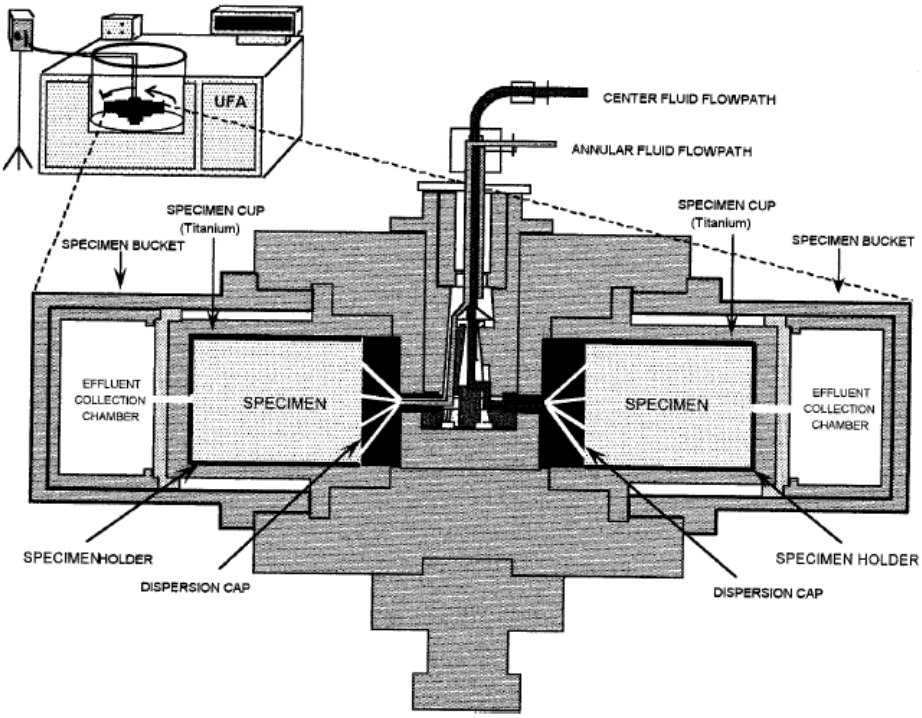

Figure 2.10 Centrifuge technique (ASTM D6527-00).

In this method Darcy's law can be arranged as follows:

$$q = -K\left[\frac{d\Psi}{dr} - \rho\omega^2 r\right] \tag{2.27}$$

where:

K: hydraulic conductivity, cm/s,

r: distance from axis of rotation, cm,

ρ: water density, gm/cm^3,

ω: rotation speed, radians/s,

Ψ: matric potential

$\frac{d\Psi}{dr}$: the matric potential gradient

$\rho\omega^2 r$: the centrifugal force per unit volume

2.4.1.4 Infiltration test

The saturated hydraulic conductivity can be determined when all the pores, including the large ones (such as cracks), are fully saturated. However, flow in macropores is difficult to quantify, because it is variable from place to place. One solution is to infiltrate water under a tension (negative pressure); this approach prevents the filling of the large pores, and gives a hydraulic conductivity measurement of the porous medium matrix (Decagon Devices, 2003).

Tension infiltrometers are widely employed in some areas, such as soil science to measure the unsaturated hydraulic properties of porous media. When a tension infiltrometer (Figure 2.11) is used, it measures the unsaturated hydraulic conductivity of the medium it is placed on at different applied tensions.

Typically, the infiltrometer maintains a small negative pressure on the water as it is infiltrating into the porous medium, which allows water to infiltrate at a slower rate than that when water is ponded on the surface. The infiltrometer has an adjustable suction (0.5 to 7 cm), which will be applied to the water in the "water reservoir" (Figure 2.11). By applying a small negative pressure (or tension) on the water as it is infiltrating, water will not enter the larger cracks or larger voids, but will infiltrate into the matrix according to pore size (Decagon Devices, 2003).

To make the hydraulic conductivity measurement, the infiltrometer is placed on the surface, making sure that it makes sound contact with the porous medium surface. Then volume at regular time intervals is recorded as the water infiltrates.

Hydraulic conductivity can be calculated as follows (Zhang, 1997):

$$I = C_1 t + C_2 \sqrt{t} \tag{2.28}$$

where I is the cumulative infiltration volume. C_1 (ms^{-1}) and C_2 ($ms^{-1/2}$) are parameters from the curve fitting of cumulative infiltration vs. the square root of time.

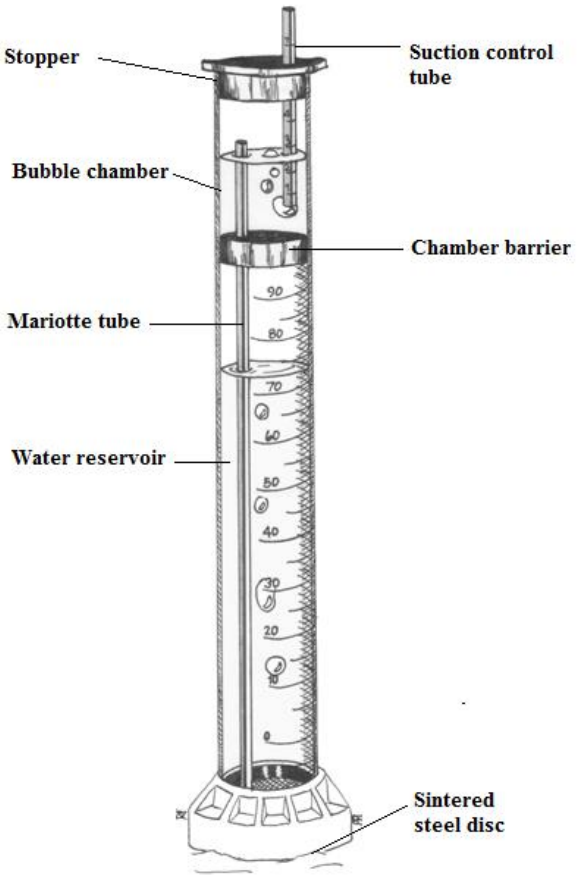

Figure 2.11 Infiltrometer diagram (Decagon Devices, 2003)

The hydraulic conductivity can therefore be calculated as follows.

$$K = \frac{C_1}{A} \tag{2.29}$$

$$A = \frac{11.65(n^{0.1} - 1)\exp[2.92\alpha h_0]}{\alpha {r_0}^{0.91}} \qquad n \geq 1.9 \tag{2.30}$$

$$A = \frac{11.65(n^{0.1} - 1)\exp[7.5(n - 1.9)\alpha h_0]}{\alpha {r_0}^{0.91}} \qquad n < 1.9 \tag{2.31}$$

where

K: hydraulic conductivity (cm/s)

n: and α are the Van Genuchten parameters for the material tested

$r_{0:}$ disk radius (cm)

$h_{0:}$ suction at the disk surface (cm)

Comparison of the three mentioned water permeability testing methods is summarized in the table below. The Tension infiltration is a fast approach to test the hydraulic conductivity for both saturated and unsaturated conditions and it does not require the preparation of samples as in water permeability test and steady-state centrifugation test.

Table 2.1 Comparison of water permeability tests

Comparison of Hydraulic conductivity test	Water permeability test	Steady-State Centrifugation	Tension infiltration
Hydraulic conductivity (saturated)	Yes	Yes	Yes
Hydraulic conductivity (unsaturated)	No	Yes	Yes
Sample preparation	Core sample	Core sample	In-situ
Test speed	Slow	Fast	Fast

2.4.2 **Chloride ion transport properties and content**

Chloride ions have a significant impact on the corrosion of steel rebar in concrete. Therefore, it is of great interest to understand the chloride content at a given location and its penetration into concrete. Several test approaches have been developed to measure chloride diffusion and concentration.

2.4.2.1 Rapid Chloride Permeability Test (RCPT)

The rapid chloride permeability test (ASTM C1202, 2010) provides a way to measure the electrical conductance of concrete, which serves as a rapid indication of its resistance to the penetration of chloride ions. The setup is shown in Figure 2.12.

The ammount of electrical current through 50-mm thick 100-mm in diameter slices of cores is monitored during a 6-hour period. Two solution reservoirs are connected by the core, of which one surface is immersed in a sodium chloride solution, and the other surface in a sodium hydroxide solution A potential difference of 60 V DC is imposed and maintained on the two ends of the specimen. The total charge passed through the core during the 6-hour period is related to the resistance of the sample to chloride ion penetration; see Table 2.2. (ASTM C1202-10)

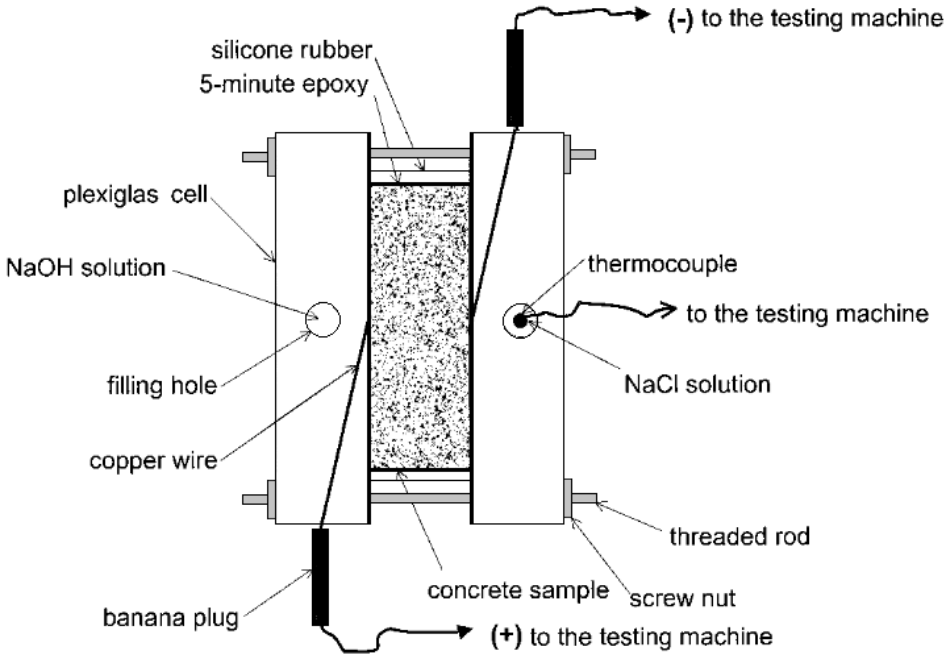

Figure 2.12 The rapid chloride permeability test (Aldea, 1999).

Table 2.2 Chloride Ion Penetrability Based on Charge Passed

Charge Passed (coulombs)	Chloride Ion Penetrability
>4000	High
2000-4000	Moderate
1000-2000	Low
100-1000	Very Low
<100	Negligible

This method gives an indication of concrete's resistance to the chloride ion penetration. However, the information provide by this test is limited: it is not able to assess the diffusion coefficient without knowing the parameters, such as chloride concentration, of the chloride penetration process.

2.4.2.2 Chloride bulk diffusion test (ASTM C1556)

In order to calculate the apparent chloride diffusion coefficient, the experimental approach should be able to give the information of chloride content at different locations over a certain interval assuming only diffusion governs the ingress of chloride ions.

The experimental procedure is as follows: (1) Obtain a sample of concrete specimens prior to exposure to chloride solution, determine the initial chloride ion content of the specimen and test the initial water-soluble chloride content according to ASTM C1218. (2) Seal all sides of the test specimen with a barrier coating, except the finished surface. Saturate the specimen in a calcium hydroxide solution to prevent further leaching off of calcium hydroxide, rinse with tap water and then immerse in a sodium chloride solution. (3) After a specified exposure time, the specimen is taken out from the sodium chloride ponding and thin parallel layers starting from the exposed surface of the specimen are ground off. A chloride concentration profile is obtained by collecting powder samples at different depths of the specimen. Record and plot the measured chloride content value vs. depth below the surface.

The apparent chloride diffusion coefficient can be calculated by non-linear regression analysis based on Fick's second law for unsteady-state diffusion:

$$\frac{\partial C}{\partial t} = \mathrm{D_a}\frac{\partial^2 \mathrm{C}}{\partial \mathrm{x}^2} \tag{2.32}$$

The solution to this partial differential equation is:

$$\frac{\mathrm{C_{(x,t)}}}{\mathrm{C_0}} = 1 - \mathrm{erf}\left(\frac{\mathrm{x}}{\sqrt{4\mathrm{D_a t}}}\right) \tag{2.33}$$

where

$C_{(x,t)}$: concentration of chlorides at distance x and time t, (% mass of concrete/cement),

C_0: concentration of chlorides at x =0, t>0, (% mass of concrete/cement),

erf: error function,

D_a: the apparent diffusion coefficient (m^2/s).

2.4.2.3 Chloride diffusion cell

When the chloride diffusion is in steady state, Fick's first law can be used to calculate the diffusion coefficient (Nilsson, 1993). Based on this theory, the chloride diffusion cell (Figure 2.13) has been developed.

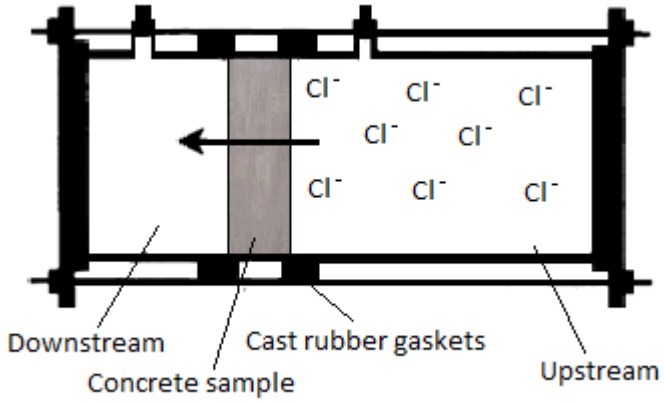

Figure 2.13 Chloride diffusion cell (Adapted from Rodriguez, 2003)

The thin concrete sample is set to separate two cell compartments, called upstream and downstream filled with a chloride salt solution, and a chloride free solution, respectively. Saturated calcium hydroxide or alkali hydroxide solutions are normally used as a downstream solution to avoid lime leaching from the concrete (Buenfeld, 1987). The chloride effective diffusion coefficient can be obtained by Equation 2.34 and 2.35:

$$J = -D_e \frac{\partial C}{\partial x} \tag{2.34}$$

$$D_e = \frac{Jx}{C_u - C_d} \tag{2.35}$$

where

J: flow of chloride ions, (mole/s·m^2)

D_e: chloride effective diffusion coefficient, (m^2/s)

x: thickness of the specimen,(m)

C_u, C_d: upstream and down stream chloride concentration, (mole/m^3)

2.4.2.4 Scanning Electron Microscopy Combined with Energy Dispersive X-Ray Analysis

This method utilizes the pairing between the chemical elements and characteristic energy spectra to identify the atom type; based on the fact that the intensity of the emitted radiation is proportional to the concentration of the element. With proper calibration, the profile of element concentration can be obtained (Buenfeld, 1987).

Rodriguez & Hooton (2003) and Win et al. (2004) studied the profile of chloride ions using this technique. The distribution of chloride atoms was presented using x-ray mapping.

Despite of the informative result of chloride mapping, SEM-EDX analysis does have its drawbacks: (1) It only measures the total chlorine content in the sample. (2) It is not sensitive to small concentrations because of the non- characteristic x-rays background. (3) The procedure of preparing the SEM sample may disturb the chloride distribution.

2.4.3 Time domain reflectometry (TDR) test

Time domain reflectometry (TDR) is a technology originally used to diagnose communication cables by locating the breaks or shorts. An electromagnetic signal is sent out to the coaxial cable and reflected by discontinuities in the cable. Collecting the travel time of the signal and converting the time to distance with knowledge of the propagating velocity, the distance to the breaks or shorts can then be determined. With the fact that the propagation velocity of an

electromagnetic wave is affected by the moisture content in the surrounding soil, researchers (Topp et al., 1980) in soil science adopted TDR reversely, with wave-guides of known length to find the moisture content of soil.

2.4.3.1 TDR dielectric constant measurement

Concrete is one type of porous medium containing at least two of the three phases – solid, gas, and liquid. Each phase can be characterized by a different dielectric constant value and the dielectric constant of the mixture reflects the fraction of each phase by volume. Usually the dielectric constant of water is roughly taken as 80, for air its value is 1, and for solid phase of porous material typically found in soil it is between 1 and 11 (Table 2.3). In concrete it is between 2.2 and 5.4 (Table 2.4). Among all compositions, water has the largest dielectric constant, which means that the water content of porous media is highly sensitive to the dielectric constant.

Table 2.3 Dielectric constants of materials forming porous media (Curtis & Defandorf, 1929)

Material	Dielectric constant
Air	1
Water	80 at 20℃
Ice	3 at -5℃
Basalt	12
Granite	7-9
Sandstone	9-11

Table 2.4 Comparison of measured to known and calculated dielectric constant (Korhonen et al., 1997)

Material	Dielectric constant	
	Measured	Known/calculated
Sand, od	2.9	3.02
Coarse aggregate, od	2.2	3.45
Unhydrated cement	2.7	2.83
Hydrated cement paste, ssd	31.2	33.64
Concrete, od	5.4	5.49
Mortar, od	3.9	4.99

od: oven dry
ssd: saturated surface dry

In the TDR technology, the dielectric constant of a porous medium is measured by a probe acting as a wave-guide (Figure 2.14).

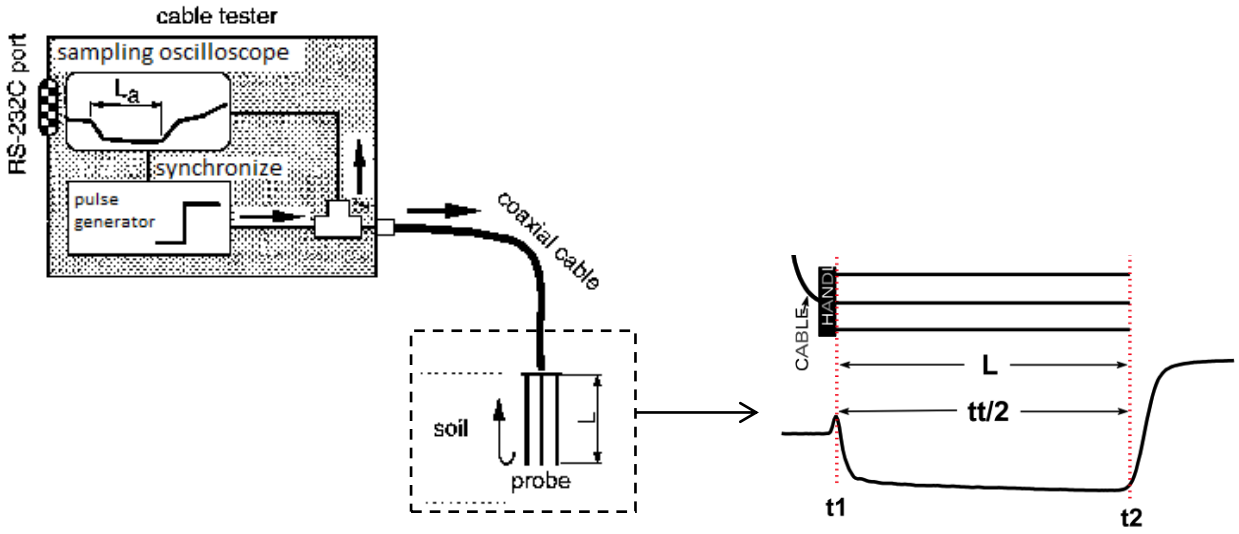

Figure 2.14 TDR set up (Noborio, 2001).

Since the velocity of the propagating wave is a known function of the dielectric coefficient of the medium (Equation 2.36), the round-trip time (i.e., the time needed for the wave to travel forth and back through the entire length of the probe) can therefore be used to calculate the dielectric coefficient of the surrounding material within the length of the probe. It is expressed as

$$v = \frac{c}{\kappa^{0.5}} \tag{2.36}$$

$$v = \frac{2L}{t} \tag{2.37}$$

where v is the signal velocity (m/s); L is the length of the probe (m); t is the round-trip transit time (s); c is speed of light in free space (3×10^8m/s), and κ is the dielectric constant of the material surrounding the probe.

Therefore, if the relationship between the dielectric constant and moisture content of the medium is known, the overall dielectric constant of the surrounding materials within the length of the probe can be determined from the round-trip time:

$$\kappa = \left(\frac{ct}{2L}\right)^2 \tag{2.38}$$

Usually the TDR testing apparatus (such as Tektronix 1502B/C Metallic TDR Cable Tester) displays apparent probe length L_a instead of giving t:

$$L_a = cV_p\frac{t}{2} \tag{2.39}$$

Thus, dielectric constant can be rewritten in terms of L_a:

$$\kappa = \left(\frac{L_a}{LV_p}\right)^2 \tag{2.40}$$

where, $V_p$is ratio of velocity of signal propagation.

2.4.3.2 TDR electrical conductivity measurement

With the same setup of TDR testing the water content, the electrical conductivity (Ec) can be determined, at the same time, by the attenuation of the signal strength during the round-trip. Figure 2.15 gives wave forms showing different attenuation amplitude in a salt solution and distilled water.

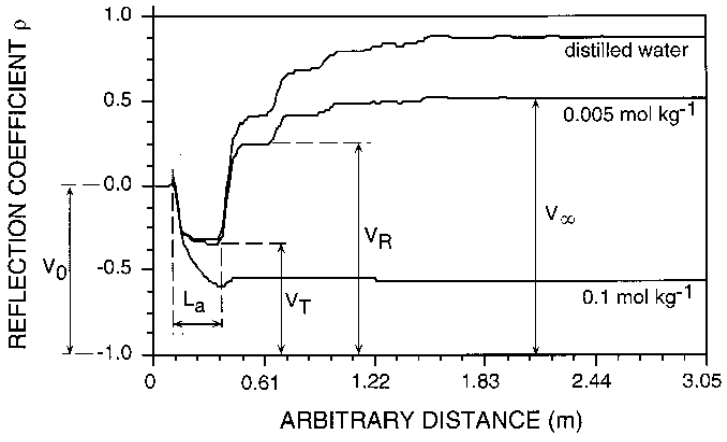

Figure 2.15 TDR waveforms in NaCl solution and distilled water (Dalton et al., 1984).

The relationship of signal amplitudes along a probe in a conducting medium in the example in Figure 2.15 can be described as (Dalton et al., 1984):

$$(V_R - V_T) = V_T exp(-2\alpha L) \tag{2.41}$$

$$\alpha = \frac{60\pi\sigma}{\kappa^{0.5}} \tag{2.42}$$

$$\sigma_D = \frac{\kappa^{0.5}}{(120\pi L)\ln[V_T/(V_R - V_T)]} \tag{2.43}$$

where $V_T$is the signal amplitude after partial reflection from the beginning of the probe; V_R is the signal amplitude after reflection from the end of the probe; α is the attenuation coefficient, and σ_D is the electrical conductivity.

Baker & Spaans (1993) and Heimovaara (1992) have proved that σ_D (Equation 2.43) is equivalent to that of Giese–Tiemann (G–T method,) (Equation 2.44) presented by (Topp et al., 1988)

$$\sigma_{G-T} = \left(\frac{K_p}{Z_u}\right)\left(\frac{1-\rho_\infty}{1+\rho_\infty}\right) \tag{2.44}$$

where K_p is the geometric constant of a probe; Z_u is the characteristic impedance of a cable tester (Ω), and ρ_∞ is the reflection coefficient at a distant point from the first reflection on the waveform, $\rho_\infty = (V_\infty - V_0)/V_0$, where $V_\infty$is the signal amplitude at the distant point and V_0 the signal amplitude from the TDR instrument. The 1502B/C TDR Cable Tester automatically calculates the total impedance, Z_L, by

$$Z_L = Z_u \frac{1+\rho_\infty}{1-\rho_\infty} \tag{2.45}$$

Therefore Equation 2.45 becomes

$$\sigma = \frac{K_p}{Z_L} \tag{2.46}$$

Probe constant K_p is determined experimentally by immersing the probe in solutions of known electrical conductivity at a certain temperature (Dalton, 1990).

$$\sigma_a = K_p f_T / Z_L \tag{2.47}$$

where $\sigma_a$is the electrical conductivity of solution, and f_T is a temperature correction coefficient.

Rhoades et al. (1976) found the relationship of electrical conductivity of bulk medium, pore solution and solid phase:

$$\sigma = \sigma_a \theta T(\theta) + \sigma_s \tag{2.48}$$

where σ_s is the solid phase electrical conductivity and T is a transmission coefficient which has a linear relationship with water content:

$$T(\theta) = a\theta + b \tag{2.49}$$

Equation 2.48 becomes

$$\sigma = a\sigma_a \cdot \theta^2 + b\sigma_a \cdot \theta + \sigma_s \tag{2.50}$$

where a and b are empirical constants. Therefore with given electrical conductivity pore solution, σ_a; the overall electrical conductivity σ is a second order polynomial function of water content, θ.

2.4.3.3 Previous applications of TDR to concrete

2.4.3.3.1 Water content

An empirical relationship between the dielectric coefficient and volumetric water content for a common soil material was established by Topp in 1980, (Equation 2.51) (Topp et al., 1980). That

equation was widely used with general type of soil and was slightly modified for improvement with specific type of soil later (Noborio, 2001; Skierucha et al., 2004).

$$\theta = -5.3 \times 10^{-2} + 2.92 \times 10^{-2}\kappa - 5.5 \times 10^{-4}\kappa^2 + 4.3 \times 10^{-6}\kappa^3 \quad (2.51)$$

where θ is the volumetric water content, κ is the dielectric constant.

However, the relationship between dielectric constant and water content has been shown to depart significantly from Topp's equation when TDR is applied on concrete. Korhonen et al. (1997) developed a second-order polynomial equation that relates dielectric constant to water content for both mortar and concrete. The results showed that the TDR readings were different between mortar and concrete and the aggregate size may also affect readings. It is suggested that a family of curves may need to be developed in order to describe the dielectric constant and water content relationship for concrete in general.

Malan and Ahmet (2002) calibrated a linear relationship for mortar and hardened cement paste, with $R^2 > 0.995$. Although it was pointed out that the best-fit trend line was a fourth order polynomial, the linear equation was shown to effectively described the water content-dielectric constant relationship.

Henryk and Zbigniew (2005) applied TDR to four types of aerated concrete to measure the volumetric water content up to 50%. Each type of concrete had a different bulk density (400 kg/m^3, 500 kg/m^3, 600 kg/m^3, 700 kg/m^3). Four second order polynomial equations were fitted.

In summary, the application of TDR in concrete water content measurement is not fully developed. Several polynomial regressions have been developed for their own kind of concrete. This technique needs a careful calibration for the concrete with a specific proportioning.

2.4.3.3.2 Salinity

As mentioned in the previous section, the TDR can be used to measure the electrical conductivity. Therefore, it is a potential means for measuring the chloride ions content in concrete. This

section summarizes previous work where TDR was used to measure the electrical conductivity in concrete. As far as the author is aware, application of the TDR technique to measure the chloride ions content in concrete will be attempted for the first time in this thesis.

There is very limited research on the measurement of salinity of concrete using TDR. Suchorab and Widomski (2011) tested the salinity change in aerated concrete. In this research, the salinity was defined as %mass. The calibration of the salinity test was done by fitting S against the reflected signal voltage (V_R as previously mentioned). The seemingly flawed part of the calibration is its lack of water content consideration, which affects the ions concentration within the material. The author also pointed out that if volumetric water content of aerated concrete is below 10%, the material salinity reading was close to zero. However, the level of water content, below which the salinity begins to be affected by water content change, was not studied.

In summary, the salinity test of concrete using TDR has only been found in the application of aerated concrete. When the water content is around 10% or lower, which is the case for most regular concrete, the water content and the ion strength brought by concrete itself may play a role in the electrical conductivity reading. It is not clear how much do these two factors affect the electrical conductivity reading in TDR. Therefore, they need to be also considered in the calibration procedure.

3 Experimental Methods

3.1 Overview

In order to investigate how the presence of cracks may affect the transport characteristics of the cracked concrete, four types of cracked concrete beams were cast. Two types of cracks were generated: natural flexural cracks, and artificial cracks (made by inserting shims at the time of casting). Two levels of crack openings, 0.3 mm and 1.0 mm, representative of ranges where the corrosion rate has been observed to be negligible and where it becomes very active respectively, were investigated. The apparent hydraulic conductivity of the cracked concrete samples was evaluated by the tension infiltration test. Time Domain Reflectometry (TDR) was adopted to measure the water content and chloride content under transient saturation conditions through probes grids for artificial and natural cracks, respectively.

3.2 Sample Preparation and Material properties

Ordinary Portland cement (CSA A5 Type GU) was used as the cementitious material for all samples in this project. Its physical and chemical properties are shown in Table 3.1. The details of fine aggregate, water, superplasticizer and rebar are summarized in Table 3.2. For this project concrete with a water/cement ratio of 0.45 was used to represent normal concrete. The 28 days compressive strength was 33.5 MPa. The mix proportioning design (Table 3.3) was based on the ACI 211.1 manual with a fixed sand ratio of 35%. Large gravels were not used in the concrete mixing because those gravels would interfere with probes, causing the stainless probes to bend; instead, coarse sand with a 0.5 cm maximum in diameter was chosen as coarse aggregate. A superplasticizer was added to increase the workability so that the mixture was cohesive and self-compacting. A good workability helps to build sound bond of concrete and probes.

Table 3.1 Chemical Analysis of the ordinary Portland cement (CSA A5 Type GU)

Chemical Analysis (% by mass)	
SiO_2	20.7
Al_2O_3	3.68
CaO	63
Fe_2O_3	2.95
MgO	4.21
Na_2O	0.14
K_2O	0.59
SO_3	2.62
Free CaO	1.02
Loss on ignition	2.7

Table 3.2 Table of raw materials

Material	Source	Standard
Portland Cement	Lafarge (Type GU)	CSA-A5
Fine Aggregate	Pit run (Coarse sand)	ASTM C-136 ASTM C-129
Water	Tap Water	N/A
Rebar	HarrisRebar	No.10 Plain carbon steel, ASTM A-615
Superplasticizer	Master Builder	ASTM C-260

Table 3.3 Mix design

Portland cement (kg/m^3)	448.9
Water* (kg/m^3)	202.0
Fine aggregate (kg/m^3)	542.2
Coarse aggregate (kg/m^3)	855.9
Superplasticizer (% by weight of cement)	0.5

*Includes water from aggregate and superplasticizer.

Two types of beams were cast: short beam and long beam with the configuration and size depicted in Figure 3.1. The samples were demolded after 24 hours and cured in the curing room with a temperature 23± 2℃ and RH>90% for 28 days.

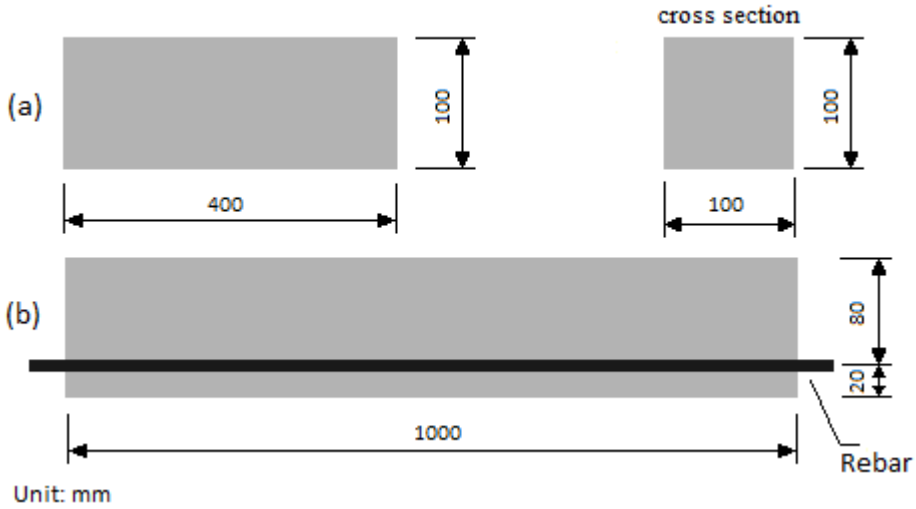

Figure 3.1 Beam sample configuration. (a) Short beam, (b) Long beam.

3.3 TDR setup

3.3.1 **Probe design**

a) Probe type

The probes of the TDR cable tester served as wave-guides. With the probes inserted, a cable tester could send the electromagnetic wave into the concrete and receive the wave back after the reflection. There are several configurations that have been proposed, with a single central conductor and one to six outer conducting rods (Figure 3.2). (Jones et al., 2002)

The simplest two-rod configuration (bottom right in Figure 3.2) was selected in order to ensure the least disturbance to moisture transport of the concrete and acquire the best resolution of the mapped grid (8×8) of data points (see the probe map in Figure 3.4) on the side surface. This probe grid covered an area of 48 cm^2 around the crack.

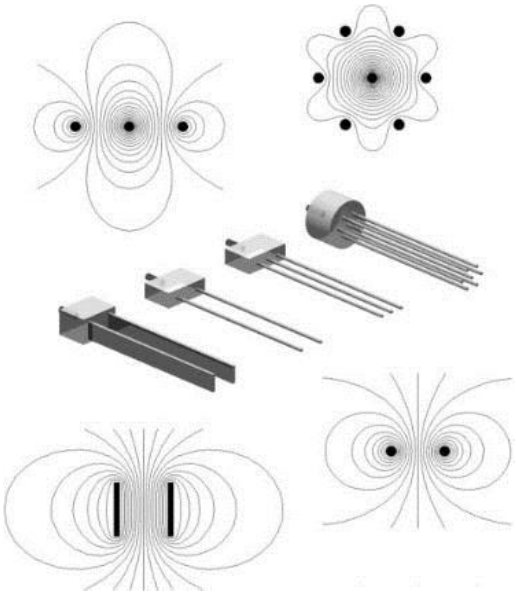

Figure 3.2 Various TDR probe designs. Electrical field lines generated by different probe configurations are also shown, where closer line spacing is associated with a more concentrated field (i.e. greater influence on permittivity) (Jones et al., 2002).

b) Probe length

Theoretically, the probe length does not affect the accuracy of water content measurement in non-conducting media. In practice, shorter probes create shorter apparent length L_a (see Equation 2.39) which leads to larger variation in the dielectric constant (Noborio, 2001). Topp et al. (1984) suggested using a probe with length L≥0.1 m to achieve an accuracy of standard deviation (S.D.) =0.02 m^3/m^{-3} in the field. For conducting media, a shorter probe will reduce the attenuation of TDR signals. Dalton and van Genuchten (1986) suggested that a practical lower limit for the probe length (for simultaneous measurement of water content and electrical conductivity) is about 0.1 m. Taken into account both the dielectric constant and the electrical conductivity measurement together with the mold size, a 90 mm probe was selected.

c) Probe diameter and spacing

Knight (1992) suggested a rule which has been widely accepted for the probe design of two- and three-wire type probes, such that rod diameter/spacing (d/s)>0.1, to reduce energy concentration around the wires. In the current study, the probe was designed with d=1.59mm, s=10mm, d/s=0.159 to satisfy the mapping of a 8×8 probe matrix within a 100 mm ×100 mm area. In summary, the two-rod probe has L=90 mm, d=1.59 mm, s=10 mm, d/s=0.159. A picture of the probe is shown in Figure 3.3.

Figure 3.3 Two-rod probe.

d) Cable design

The TDR cable consisted of a BNC connector, coaxial cable and alligator clippers; the BNC connector connected the coaxial cable to the Tektronix 1502B/C Cable Tester. The length of the cable was 2 m which was far from the upper limit (about 15 m) where recording of signal reflection may be affected (Heimovaara, 1993).

3.3.2 **Probe installation**

In order to obtain the profile of water and chloride content, the TDR probes were inserted from the lateral surface of the sample (or the top surface before demoulding; the samples were side-cast), which, before demolding, was the finishing surface of the sample (Figure 3.4). For the unreinforced short beam 9x8 probes were installed and for the reinforced long beam, probes on Row 7 were excluded to avoid the rebar at that position. In each column the neighboring probes acted as a two-rod probe when connected to the cable tester.

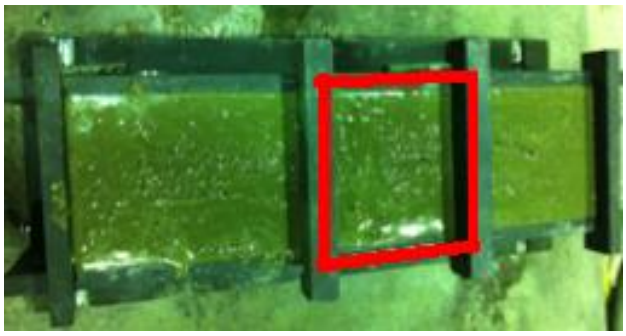

(a)

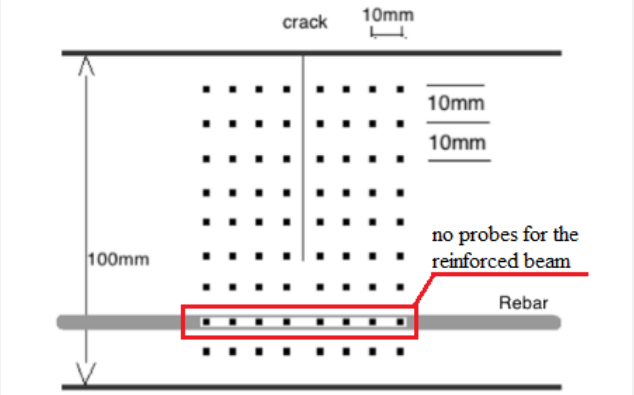

(b)

Figure 3.4 Probe map view from the finishing surface (a) a picture of the probe inserting aera, and (b) a schematic of the probe map; the black dots indicate the location where the probes are inserted.

A probe holder (Figure 3.5) was designed to keep the probes parallel to each other and perpendicular to the concrete surface. The edges of those holes were manufactured with chamfers which allowed the probes to easily pass through.

The timing for inserting probes was important; the proper setting condition should ensure enough friction between the mixture and the probe to prevent the probes from sinking through the specimen but not too much to cause the plastic deformation of unhardened concrete contacting probes. This deformation would create air gaps between the concrete and the probes. In order to determine the best setting condition, a cylinder sample, on which trials of inserting probes were performed, was cast from the same batch as the beam samples. The probes together with the holders were installed approximately 15 minutes after casting (Figure 3.6) and then the holders were removed 3 hours after casting.

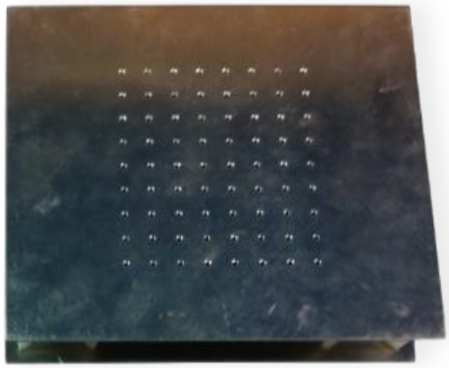

(a)

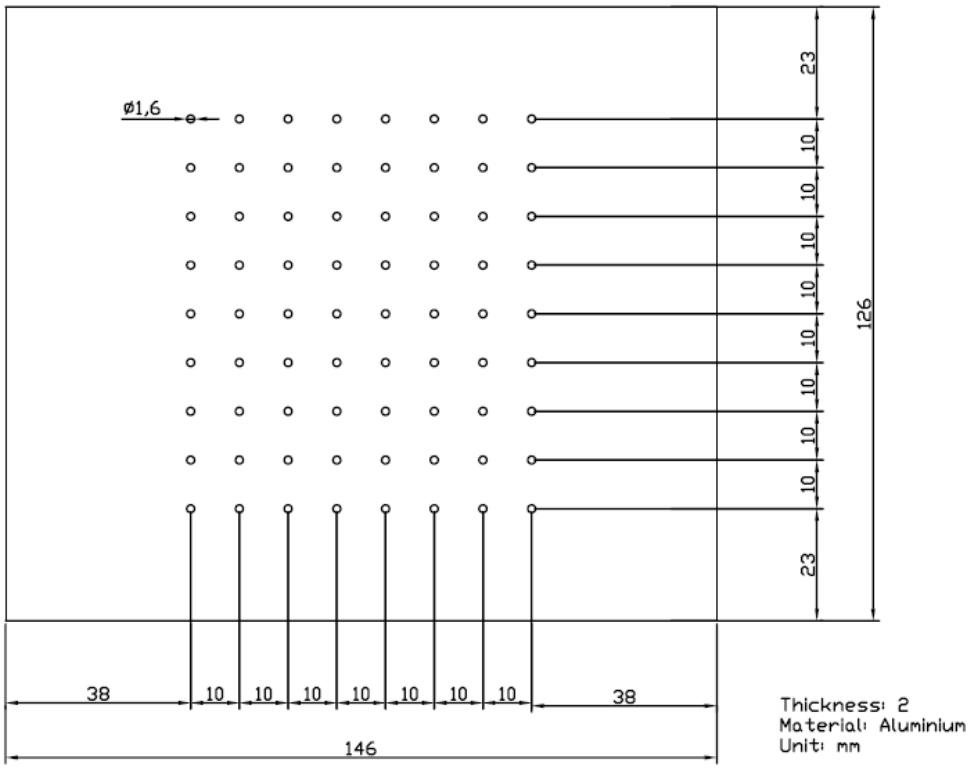

(b)

Figure 3.5 Double-layered probe holder. (a) Picture of an actural holder (b) Schematic representation with dimensions.

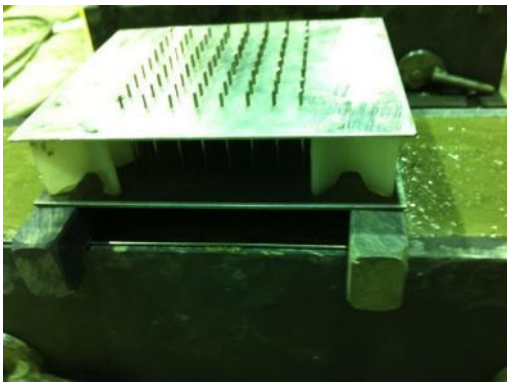

Figure 3.6 Installation of probes.

3.4 Creation of cracks

Two types of cracks were created: artificial cracks and natural flexural cracks; two levels of crack sizes were also used.

Artificial cracks were introduced by casting concrete beams with a shim implanted at the middle bottom of the mold, while the natural flexural cracks were created by applying three-point flexural loading. In conclusion, four types of cracked beams were used for this study. Sample features are summarized in Table 3.4

Table 3.4 Summary of crack samples

Sample ID	Sample number	Crack type	Crack width (mm)	Reinforcement
A03	3	Artificial	0.3	No
A10	3	Artificial	1.0	No
N03	3	Natural	0.3	Yes
N10	3	Natural	1.0	Yes

3.4.1 **Creation of artificial cracks**

Before casting the concrete mixture, shims were attached to the walls of the molds in order to create the artificial cracks. Shims with a 60×100 mm cross section and thicknesses of either 0.3 mm or 1.0 mm were attached to the side surface of the mold by epoxy (Figure 3.7). The epoxy was cured for 10 minutes to develop the bonding strength. During casting, the mixture was poured simultaneously from both sides of the shim to ensure an equal pressure was acting on both sides of the shim.

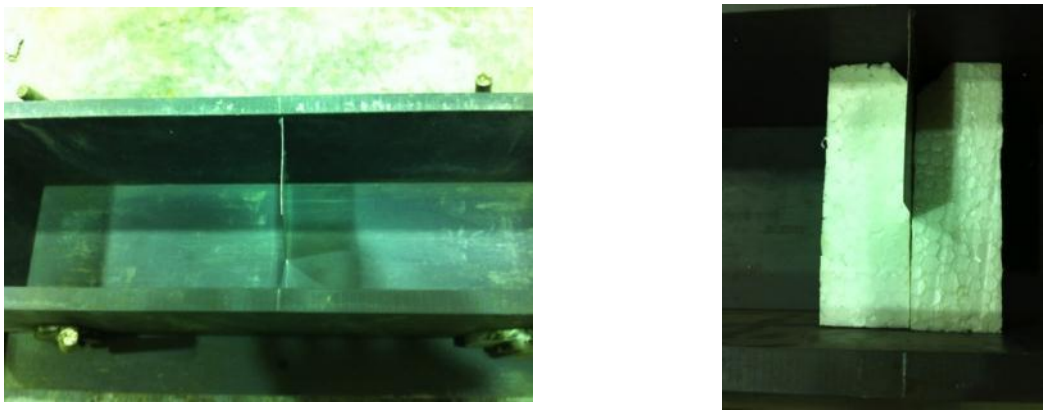

Figure 3.7 Mold for generating artificial cracks.

From the preliminary tests, it was observed that the removal of shims when demolding (24 hours curing) would cause the failure of the epoxy bonding or even the rupture of shims. Therefore, the shims were pulled out before demolding. This was achieved with the following steps: 3 hours after casting, C-clamps (as shown in Figure 3.8) were used to gently pull out 5 mm of the shim (without disturbing the probe holder) and then after 24 hours curing the shim was pulled out completely. Once the crack was shaped, samples were placed in the curing room (Figure 3.9).

Figure 3.8 Shim pull-out set up.

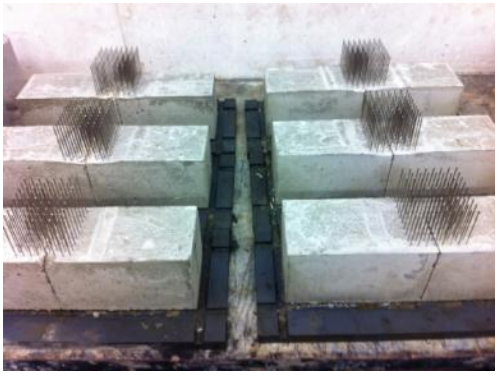

Figure 3.9 Samples cured with probes installed.

3.4.2 **Creation of flexural cracks**

The natural cracks were created by a three-point flexural loading. It was noticed from the preliminary tests that if the rebar was placed in the tension zone, the beam would readily fail due to shear, for this rebar reinforcement configuration without stirrups. If the stirrups were added, instead of one single crack, multiple cracks would be created along the beam and an anchor system would be needed to keep the flexural loading at a constant value. If the rebar was placed in the compression zone, it would be able to prevent the growth of the crack from extending through the entire beam depth. In addition, the single crack could be generated when the mid-

span concrete reached the fracture strength, and it was convenient to keep it open at desired width by inserting shims.

A notch was made at bottom of the beam mid-span to promote the creation of a crack at that location. Then, the samples were subjected to a three-point loading test with a 0.9 m span. The test configuration setup is shown in Figure 3.10. The loading was conducted at a rate of 0.3 kg/s and was programmed to stop when a sudden 10% percent drop of the crack took place. The loading vs. mid-span displacement diagrams are shown in Figure 3.11.

(a) (b)

Figure 3.10 Generation of natural cracks (a) three-point flexural loading test, (b) picture of a natural crack.

Cracks were generated at load values in the range of 1500-1800 N. Once a crack was created, it could be easily reopened later by adjusting the fine-position knob. After the coating treatment was done (see Section 3.4.3), Two shims were inserted near the top surface from both the front side and the back side of the crack. Shims with thicknesses of 0.3 mm and 1.0 mm were used to maintain the crack openings 0.3 mm and 1.0 mm wide throughout the crack.

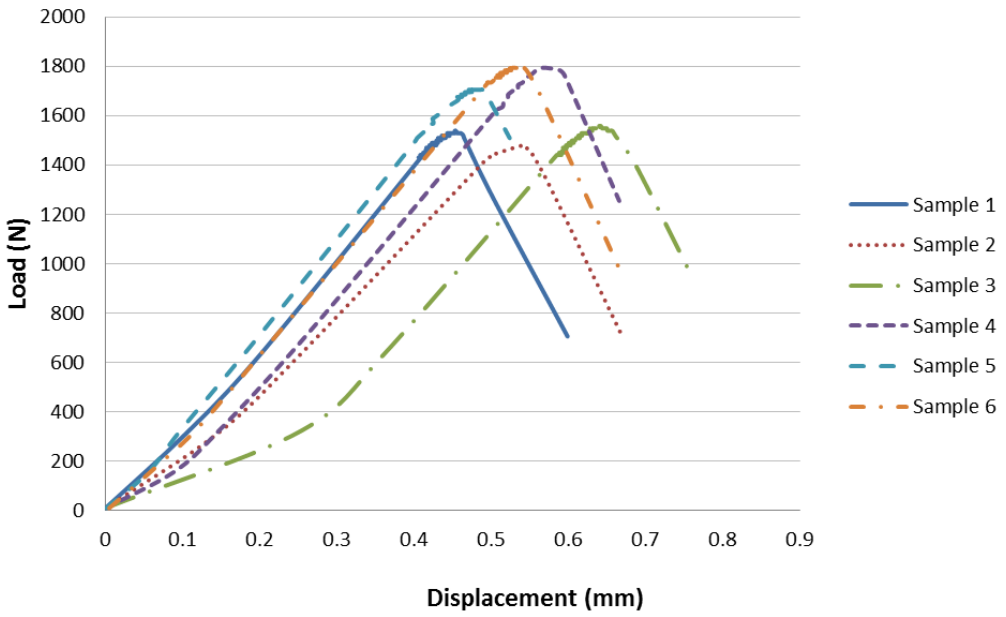

Figure 3.11 Loading and mid-span displacement.

3.4.3 **Coating and finishing**

All sides of the samples were coated with epoxy, except the finish surface, which allowed one dimensional transport of moisture and chloride ions and was more representative of many field structures, such as bridge decks.

The coating epoxy was made by mixing resin and cure with a mixing ratio of 1:1 by volume. Before application, all samples were cleaned by a compressed-air blower to remove any dust or debris. Three layers of coating were applied to the samples to ensure the fill of all open pores in the concrete surface. Care was taken to prevent the epoxy from filling the cracks. After each coating was applied, one-week curing time was allowed for the epoxy to become solid and develop strength.

The exposed probe part had a length of 6 cm. This may cause disturbance to the waveform by bringing additional peaks of the signal echo reflected both from the open end and the probe-concrete joint. As indicated by the red arrows, additional peaks appeared near the first reflection peak [Figure 3.12 (a), (c), (e)] when the probes were connected from the extended open end and appeared near the second reflection peak when the probes were connected from the probe-

concrete joint [Figure 3.12 (b), (d)]. Hence, all extended probes were cut short allowing only enough length, 5 mm, for the cable clips to connect. The epoxy that remained on the probe tips was carefully scratched off (Figure 3.13).

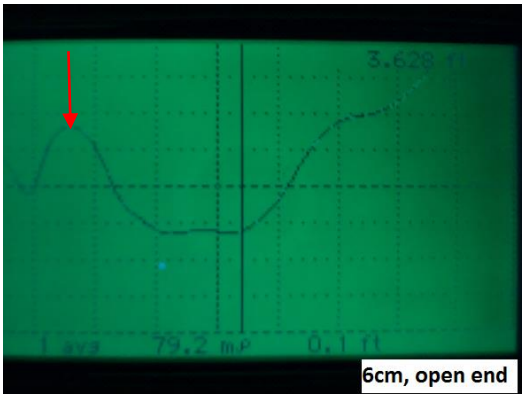

(a)

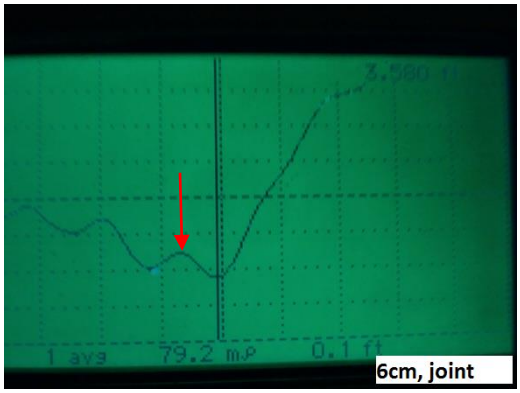

(b)

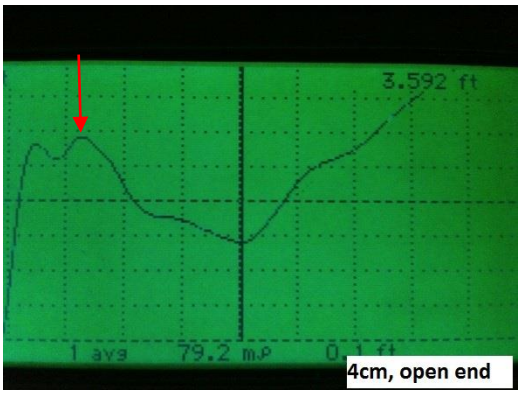

(c)

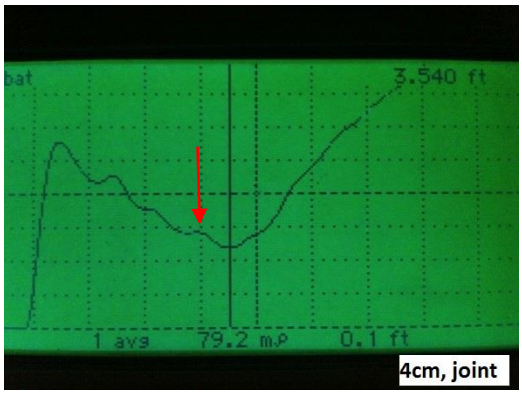

(d)

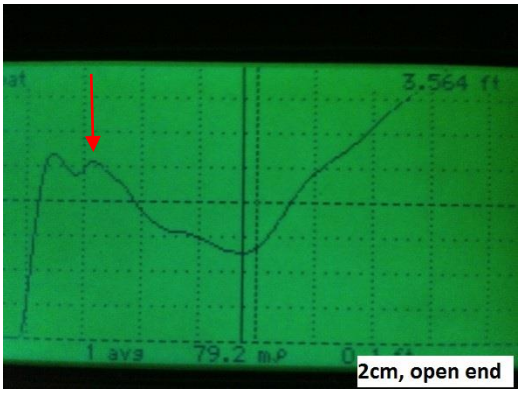

(e)

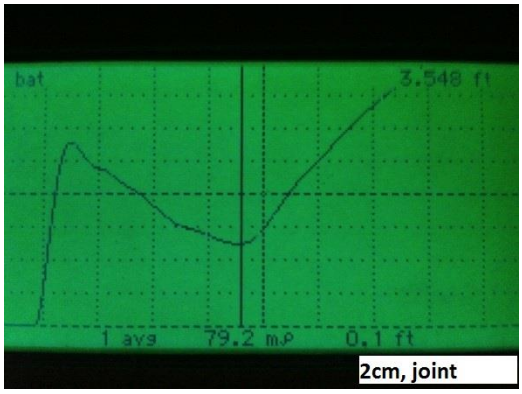

(f)

(g)

Figure 3.12 Wave forms from probes of different extend length (a) extended probe length is 6 cm, clips at the end of probe; (b) extended probe length is 6 cm, clips at the joint of probe and concrete surface; (c) extended probe length is 4 cm, clips at the end of probe; (d) extended probe length is 4 cm, clips at the joint of probe and concrete surface; (e) extended probe length is 2 cm, clips at the end of probe; (f) extended probe length is 2 cm, clips at the joint of probe and concrete surface;(g) extended probe length is 0.5cm.Note: horizontal axis is the reflection rate and the vertical axis is the distance.

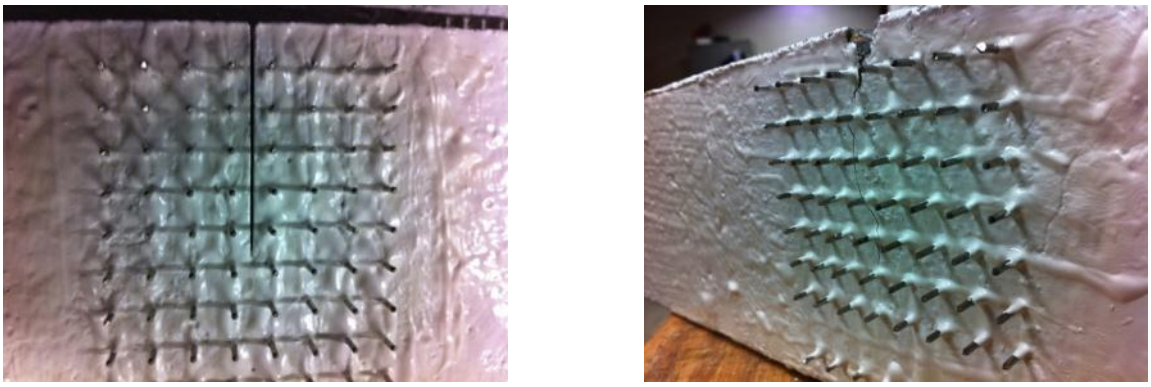

(a) (b)

Figure 3.13 Final-finished probes (a) sample with an artificial cracks and (b) sample with a natural crack.

3.5 Infiltration test

The Decagon mini disk tension infiltrometer was used to measure the hydraulic conductivity. As shown in Figure 3.14, the porous steel disk of the infiltrometer was placed on the cracked surface. Fine sands and a nylon membrane were used to ensure a good contact between the concrete

surface and the steel disk. Because the ponding treatment was conducted right after the infiltration test, the ponding solution (see Section 3.6.3) was used for the infiltration test to prevent from diluting the penetrated solution during ponding. According to Table 3.5, the suction was adjusted to 1 cm so that the water would infiltrate into the cracks with crack widths of 0.3 mm and 1.0 mm at a proper rate. The volume of the fluid was recorded at time 0 and every 30 seconds thereafter during the infiltration test until the water volume in the reservoir dropped to 1 ml. Curve-fit of the cumulative infiltration volume vs. square root of time was used in conjunction with Equations (2.28)-(2.31) to find the apparent hydraulic conductivity of the cracked area.

Figure 3.14 Infiltration test set up.

Table 3.5 Maximum pore diameter to specific suction head (Decagon Device 2003)

Suction setting	1 cm	2 cm	3 cm	4 cm	5 cm	6 cm	7 cm
Pore diameter	2.90 mm	1.45 mm	0.97 mm	0.73 mm	0.58 mm	0.48 mm	0.41 mm

3.6 Time Domain Reflectometry (TDR) test

3.6.1 Probe constant calibration

The probe constant, K_p, was experimentally determined by immersing the probe in the solutions of known electrical conductivity at a certain temperature and calibrating the total impedance measured by TDR with the electrical conductivity of the solution. (Dalton et al., 1990; Persson et al., 2000). A series of NaCl solutions (0%, 0.6%, 1.2%, 1.8%, 2.4%, and 3.0% by weight) were prepared for the calibration. All solutions were allowed to reach room temperature (22.4 ℃). The electrical conductivity was measured by the Ec-meter and the total impedance Z_L was read from the Tektronix 1502B at an "infinite distance" (60 m was used) with full length of probe submerged in the beaker.

3.6.2 TDR Calibration

The TDR calibration included two parts: (1) the calibration of dielectric constant and water content and (2) the calibration of electrical conductivity and chloride content.

Six calibration samples (10 cm $\times$10 cm $\times$ 3$\pm$0.5 cm) were sawed off from one short beam, which were made with the same concrete as that of the tested beams. Each sample had nine probes, which gave eight readings from each sample (Figure 3.15). After exposure to ambient air in RH=40$\pm$2% for 30 days, these six samples were submerged for three months respectively in a series of NaCl solutions with concentration 0.0%, 0.6%, 1.2%, 1.8%, 2.4%, and 3.0% by weight (Figure 3.16).

Eight tests were conducted to measure the dielectric constant and impedance at the probes of the concrete blocks with various levels of uniform moisture content. The different levels of uniform water content were obtained by stepped oven drying. The initial TDR readings were taken when the specimens were removed from the ponding solution and their surfaces were towel-dried to saturated surface-dry (SSD) conditions and weighed. Following that, eight times of drying were conducted. Each time, the specimens were placed into a 105℃ drying oven for 2-3 hours; the final drying was conducted for 24 hours. After each drying, the samples were removed from the oven, wrapped and sealed in plastic bags and kept for 3 days to allow the moisture to get evenly

distributed in the specimens. For each water content level, the water content of the sample was measured by weight; the dielectric constant and electrical conductivity were measured with the TDR system. The time allowed for the water to equalize is conservative; it was decided based on Korhonen (1997) where a much larger cylinder specimen was used. Also the calibration data were read from different locations of the specimen, they did not show an uneven water distribution in the specimen.

Figure 3.15 Calibration samples.

Figure 3.16 Ponding of calibration samples.

3.6.3 **Environmental treatment**

For the wetting phase, the specimens were submerged in a 3% NaCl solution with the uncoated surface facing up, about 5 cm under the water surface (Figure 3.17). In the curing room, the RH was maintained above 90% to minimize the evaporation of the solution. The electrical

conductivity of the ponding solution was monitored by an Ec-meter. The electrical conductivity was maintained at 118 ±5 dS/cm, which corresponds to 3% NaCl solution.

Figure 3.17 Ponding of coated cracked concrete beams

For the drying session, the beams were exposed to the ambient air in the laboratory environment, which is 40±2% RH, and 23 ℃.

3.6.4 **Dielectric constant and electrical conductivity test**

The TDR test setup consists of a cable tester (Tektronix 1502B), coaxial cable, and stainless probes embedded in concrete samples. The specimens were subjected to wetting and drying cycles. During the environmental treatment, the dielectric constant and electrical conductivity were measured from the probes grid. As illustrated in Figure 3.18, each two vertical neighboring probes formed a two-rod probe, or probe pair, which gave eight probe pair in each column (9 probes) for unreinforced samples and 6 probe pair in each column (7 probes) for reinforced samples. Both types of samples had eight columns of probe pair, which gave 8×8 data and 8×6 data for the artificial crack samples and the natural crack samples, respectively. During wetting cycle, the samples were taken out and measured by TDR system, at 0, 1, 3, 5, 8, 13, 22, 33, 56, 80, 128, 200, 296 hours. When the samples were taken out of the ponding solution, they were immediately wrapped with a plastic membrane to prevent evaporation from the surface. During the drying cycle, the dielectric constant and electrical conductivity were measured at 0, 4, 11, 23, 47, 95, 167, 263, 407, 695 hours.

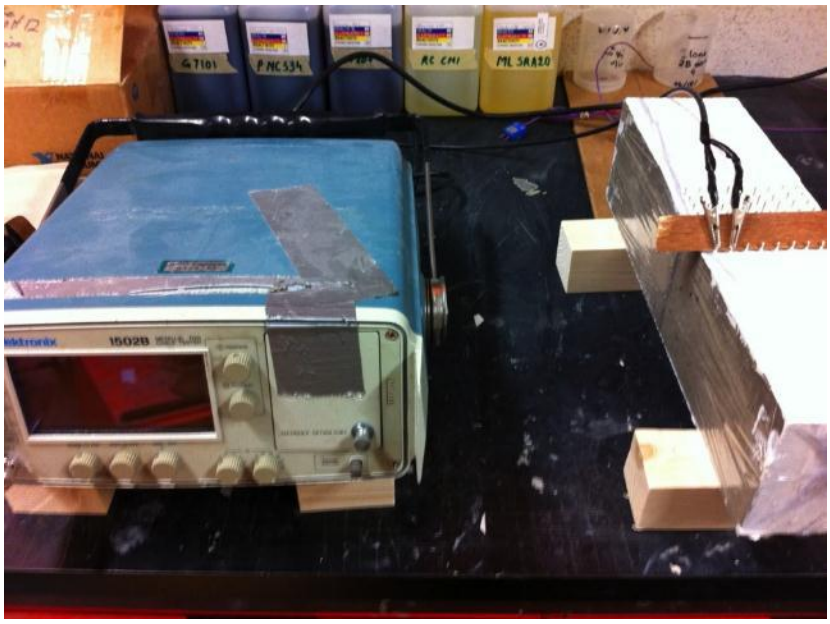

Figure 3.18 Schematic of a TDR test

A typical display of the TDR test is shown in Figure 3.19. The apparent length L_a (in foot) was read when the cursor was placed at the lowest point of the waveform. The length reading at the reflection (lowest on the wave form) ranged from 9.500-9.700 ft and the minimum grid of the cursor position was 0.004 ft that gave a 0.8% precision. The total impedance Z_L was read when the cursor was moved to a distance more than 200 ft (60 m). With the geometric probe constant K_p known from the calibration test, the dielectric constant and electrical conductivity could be calculated using Equation 2.40 and Equation 2.46, respectively.

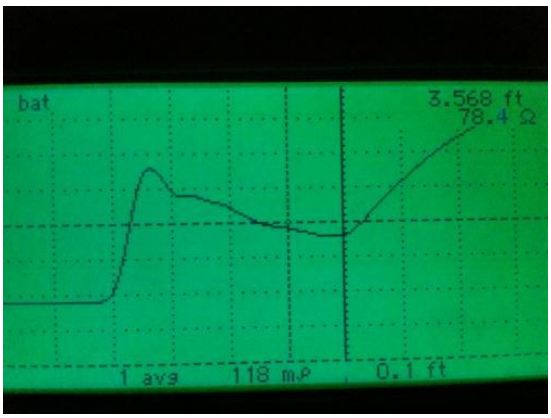

Figure 3.19 Typical TDR waveform.

4 Results and Discussion

4.1 Hydraulic conductivity of cracked concrete

Concrete samples with four types of cracks, including small artificial crack size, large artificial crack size, small natural crack and large natural crack size were tested. The hydraulic conductivity of the cracked area was tested by the tension infiltrometer following the experimental steps described in Section 3.5. A regression analysis for cumulative volume change vs. square root of time was conducted and the hydraulic conductivity, K, was calculated according to Equations 2.28-2.31. Van Genuchten parameters $\alpha=4.33\times10^{-4}$ and n=2.0 were selected from results from Section 5.4 to determine parameter "A" in Equation 2.31.

For each type of crack, three replicates were tested. The apparent hydraulic conductivity, K, is shown in Table 4.1 and plotted in Figure 4.1.

Table 4.1 Apparent hydraulic conductivity of cracked beams in the cracked area

Crack type	Artificial		Natural	
Crack width (mm)	0.3	1.0	0.3	1.0
Hydraulic conductivity,K (cm/s)	1.27×10^{-5}	3.43×10^{-5}	3.56×10^{-6}	1.56×10^{-5}
	1.75×10^{-5}	1.80×10^{-5}	5.43×10^{-6}	4.21×10^{-5}
	2.04×10^{-5}	3.60×10^{-5}	7.62×10^{-6}	3.31×10^{-5}
Average	1.68×10^{-5}	2.94×10^{-5}	5.54×10^{-6}	3.03×10^{-5}

The hydraulic conductivity, K, as measured by this method is an overall or effective value for the cracked concrete (concrete plus the crack under the infiltrometer's disc). The hydraulic conductivity of the crack by itself cannot be evaluated, using this approach, because the flow pattern in the crack was unknown. It can be seen from the Table 4.1 that the hydraulic conductivity of cracked concrete ranged from 3.56×10^{-6} to 4.21×10^{-5} cm/s. For a typical regular concrete with water-cement ratio of 0.4-0.5, the hydraulic conductivity is of the order of 10^{-10} cm/s to 10^{-11} cm/s (Mehta, 2006). The presence of cracks provided pathways for water flow, which dramatically increases the value of the hydraulic conductivity by up to five orders of magnitude.

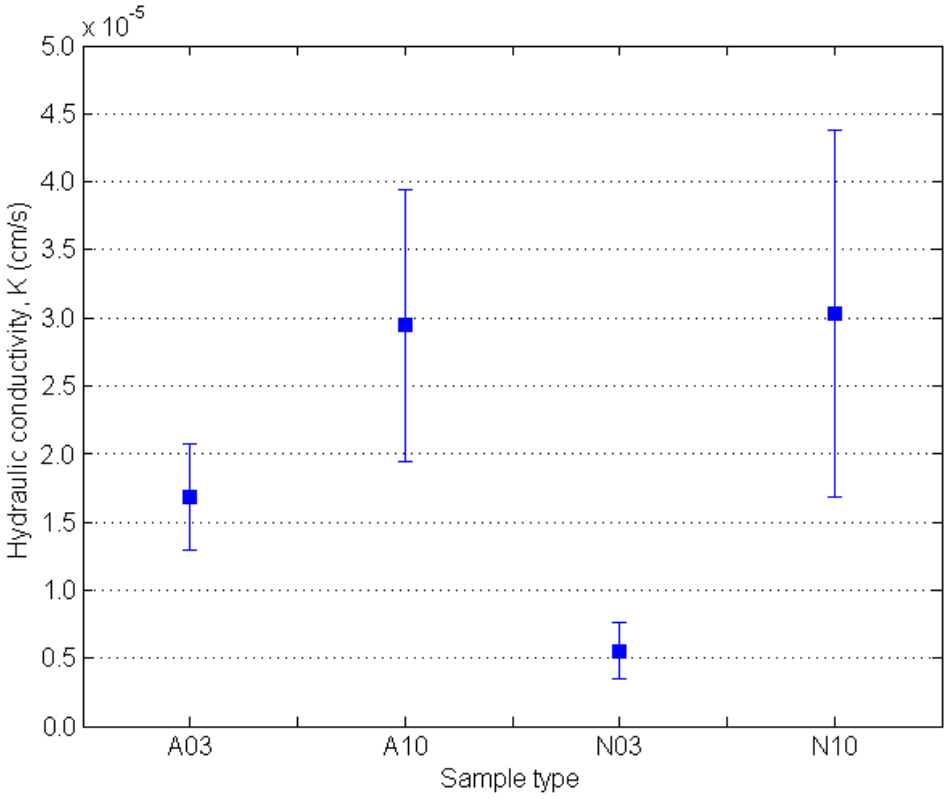

Figure 4.1 Apparent hydraulic conductivity of cracked beams in the cracked area; sample type: A03- 0.3 mm artificial crack, A10- 1.0 mm artificial crack, N03- 0.3 mm natural crack, N10- 1.0 mm natural crack. The error bars represent the highest and lowest value of observation.

It can also be observed that cracked samples, both artificial and natural, with larger crack widths had larger hydraulic conductivity, K. However, the increase of crack width had greater impact on the natural crack category: for artificial cracks, comparing to small cracks, large cracks increased K from 1.68×10^{-5} cm/s to 2.94×10^{-5} cm/s, or by 0.75 times while the natural cracks increased it from 5.54×10^{-6} cm/s to 3.03×10^{-5} cm/s, or by 4.46 times.

For the same crack size, the crack type had a different influence on the K value: for a 0.3mm surface crack opening, the natural crack had a significantly lower K than an artificial crack while for a 1.0 mm crack; both types of cracks gave a similar value of K.

To interpret the results, two factors that affect the water flow need to be considered: pathway size and texture. A crack serves as a pathway for the water to infiltrate, and according to fluid mechanics fundamentals a larger pathway gives less friction for the water flow (Munson et al., 1990). This is why concrete with larger cracks has a higher hydraulic conductivity. For the natural cracks with larger size of crack opening, the hydraulic conductivity is dramatically increased. The artificial crack is a two-parallel-wall crack with a smooth texture while the natural crack has a rough texture and torturous geometry. Depending on the crack size, roughness of the crack surface may or may not affect K. When the crack opening is small enough, the crack surface roughness plays a role in defining the flow channels within the crack. When the crack opening is large, the crack surface roughness has less impact on the crack opening, at any given point. That is why for large cracks, K is basically equal for both artificial and natural cracks while for small cracks, the natural cracks give a smaller K.

It conclusion, both larger crack sizes and smoother texture would increase the hydraulic conductivity of concrete. The effect of crack roughness is significant on concrete with small size cracks. However for concrete with large cracks, this effect does not have a significant impact on the hydraulic conductivity.

4.2 Calibration results

4.2.1 Probe constant

The geometric constant of the probe configuration used in the TDR test was determined according to the procedure described in Section 3.6.1. The results are tabulated in Table 4.2. The electrical conductivity, Ec, versus the multiplicative inverse of impedance, Z_L, is illustrated in Figure 4.2.

Table 4.2 TDR impedance and electrical conductivity of salt solutions with different concentration

NaCl%wt	TDR impedance(Ohm)	Ec meter(mS/cm)
0.0	greater than 1000	1.88×10^{-2}
0.6	11.0	25.0
1.2	5.6	42.2
1.8	4.1	74.4
2.4	3.5	97.1
3.0	3.0	118.1

Temperature: 22.4 ℃

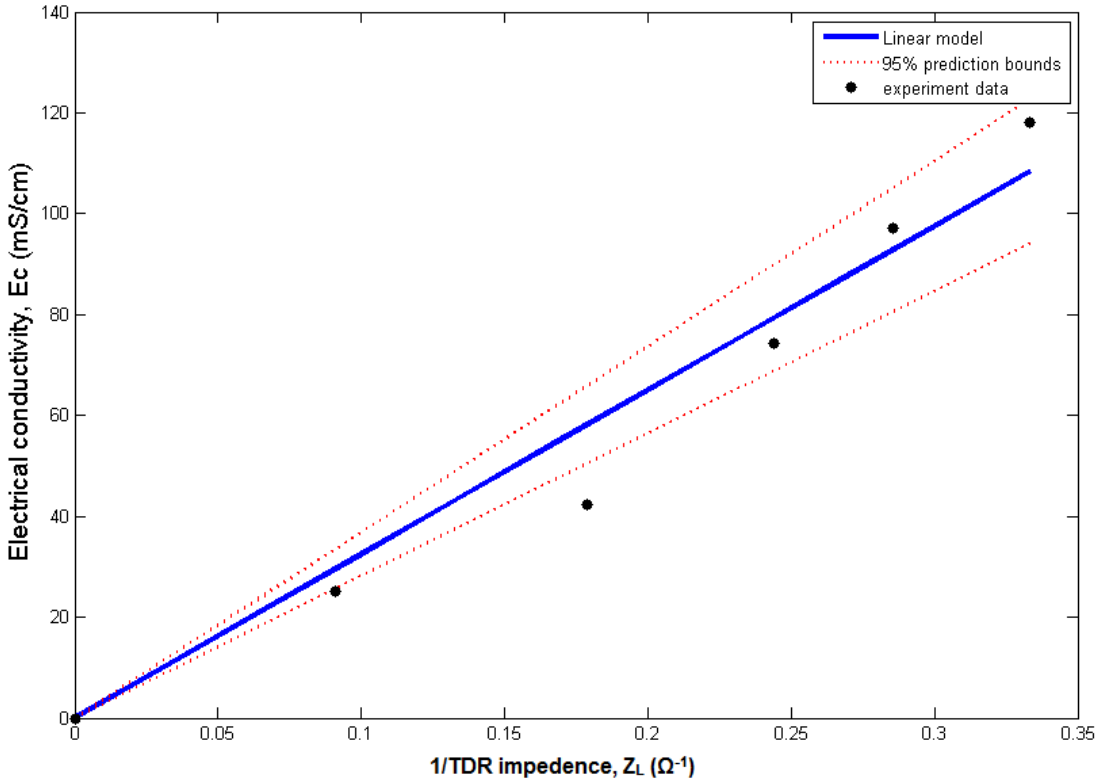

Figure 4.2 Regression of probe constant.

The linear regression model, $Ec(Z_L) = K_p * Z_L$, gave a coefficient estimate (with 95% confidence bounds): K_p =325.1 m/cm (282.2, 368.1). It relates the electrical conductivity to the TDR impedance reading according to $\sigma = K_p/Z_L$ which is same as Equation 2.47 without the temperature factor. When the configuration of probes changes, such as changing the rod spacing, rod length, or rod diameter, K_p needs to be recalibrated.

4.2.2 **Water content and dielectric constant relation**

Water content of six samples was recorded during the oven drying (Figure 4.3), and accordingly the apparent length, L_a was also collected and converted to dielectric constant κ using Equation 2.40. For each sample, seven readings were made from seven pairs of probes formed by eight probes in each sample. Considering the evaporation of water from the sample during the test, two readings near the specimen edge were not taken into account. The averaged dielectric constant versus water content for all six samples is plotted in Figure 4.4.

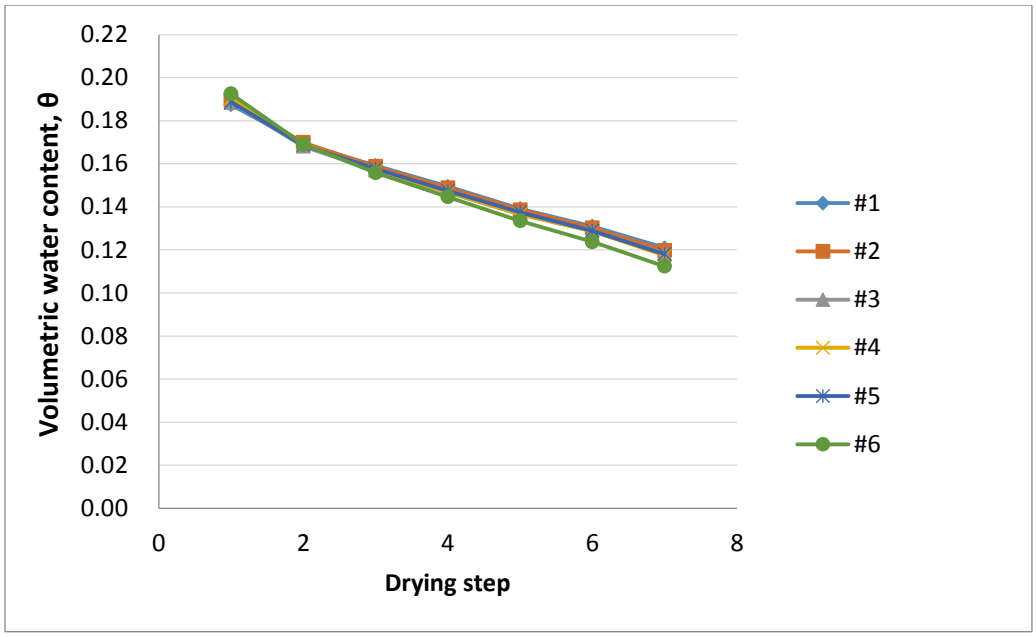

Figure 4.3 Oven dry water content change of calibration samples.

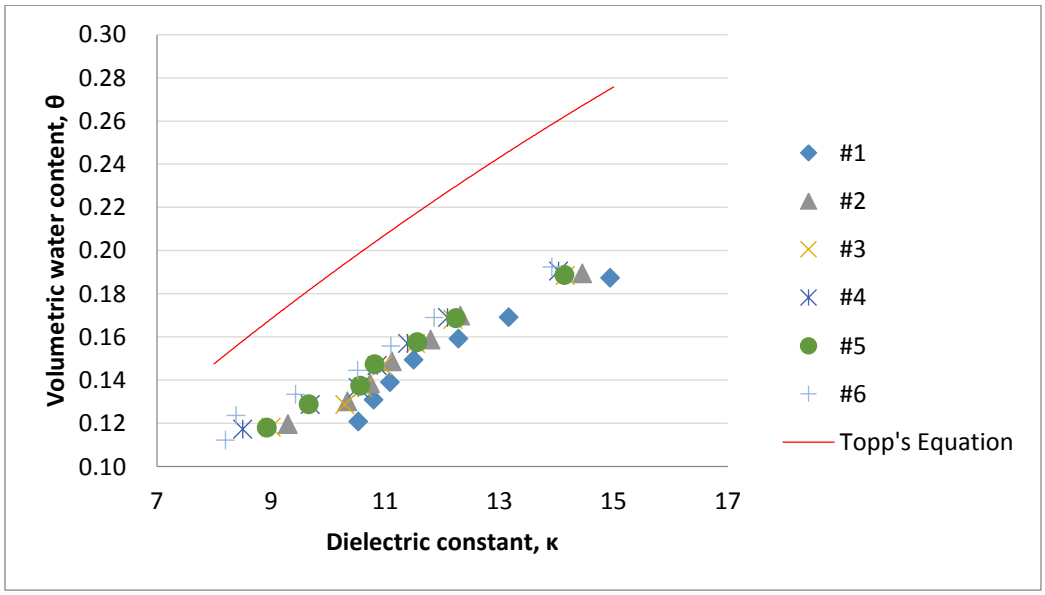

Figure 4.4 Relationship between water content and dielectric constant (sample #1, 2, 3, 4, 5, 6 were soaked in NaCl solution with 0.0%, 0.6%, 1.2%, 1.8%, 2.4%, and 3.0% NaCl by weight, respectively).

The relationship between water content and dielectric constant is similar to the well-known Topp's Equation (2.51) for soils. However, an overall drop of the water content is observed for the concrete, for dielectric constant in the tested range. This means that for a similar dielectric constant, concrete has a lower water content than soil by approximately 0.06 (see Figure 4.4). Korhonen et al., (1997) also observed a similar trend in the TDR calibration test with a drop of roughly 0.05 and 0.10 for concrete and mortar, respectively. Hardened cement paste has a specific surface area that is several orders of magnitude greater than that of unhydrated cement, sand, coarse aggregate and soil. Since bonded water has a lower dielectric constant than bulk water (Jacobsen and Schjønning, 1993a,b), a material with higher surface area and thus larger portion of bonded water would be expected to have a lower dielectric constant for the same water content. The bonded water phenomenon explains the deviation of water content- dielectric constant relationship from Topp's equation.

A linear model and a quadratic model have been used for the curve fitting of the relationship between volumetric water content and dielectric constant in concrete (Section 2.4.3.3), while a three-degree polynomial equation was used in soil.

Four possible equations, including polynomials from 1 to 4 degrees, have been studied; see fit 1 to fit 4 in Figure 4.5.

The 3-degree and 4-degree polynomial might be best fit for the given data to have a maximum R^2 statistically. However, these two high degree polynomials are over fitted, because the two curves become flat at both lower and higher end of κ, which does not agree with the trend of data that greater water content gives greater dielectric constant; for example at the lower end of the fit3 and fit4, the water content decreases with the increase of dielectric constant. Therefore, only 1-degree (linear) and 2-degree (quadratic) polynomials fitting models are considered and discussed below.

2-degree (quadratic) polynomial model:

$$\theta(\kappa) = a + b\kappa + c\kappa^2$$

where κ is the dielectric constant and θ is the volumetric water constant.

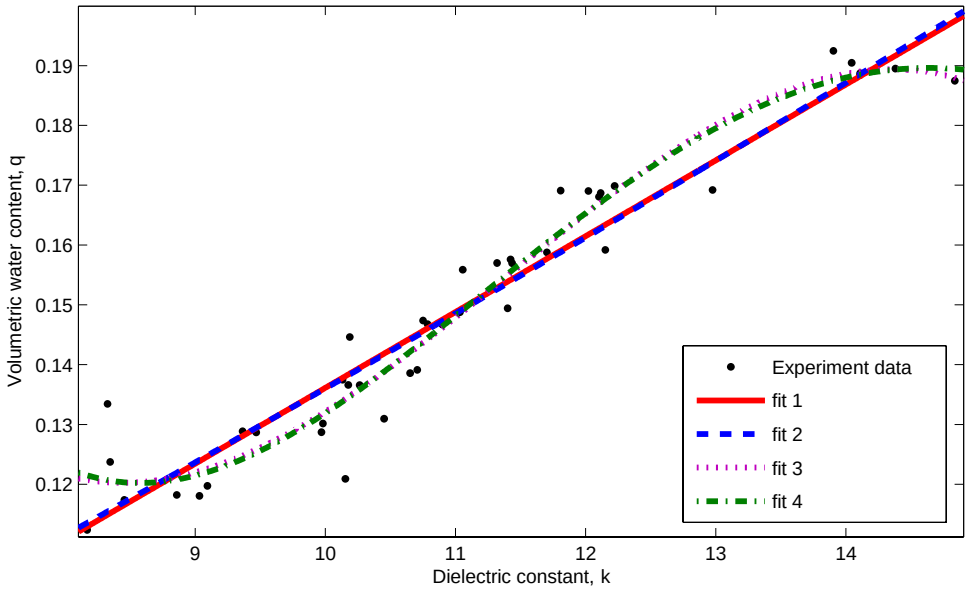

fit 1: $\theta(\kappa) = a + b\kappa$
fit 2: $\theta(\kappa) = a + b\kappa + c\kappa^2$
fit 3: $\theta(\kappa) = a + b\kappa + c\kappa^2 + d\kappa^3$
fit 4: $\theta(\kappa) = a + b\kappa + c\kappa^2 + d\kappa^3 + e\kappa^4$

Figure 4.5 Water content- dielectric constant curve fitting options.

Table 4.3 Statistics of 2-degree polynomial regression (fit 2)

Estimated Coefficients	Estimate	SE	tStat	pValue
Intercept	0.020154	0.036663	0.5497	0.58566
b	1.6482	0.010734	0.0065126	0.10735
c	8.531e-05	0.00028446	0.29991	0.76584

SE: standard error
tStat: t-statistic
Significance at pValue<0.05
Number of observations: 42, Error degrees of freedom: 39
Root Mean Squared Error: 0.0065
R-squared: 0.925, Adjusted R-Squared 0.922
F-statistic vs. constant model: 242, p-value = 1.06e-22

The p-value of the κ^2 coefficient is 0.7658. This is much greater than 0.05, which suggests that the estimated coefficient of κ^2 is not significant. Therefore, there is no need for a quadratic model and the linear model can be expressed as follows.

$$\theta(\kappa) = a + b\kappa$$

The statistics of the linear regression analysis are shown in Table 4.4, where one can easily see that the p-value is 3.944×10^{-24}. This suggests that the κ item is significant. The linear model was therefore adopted. The data points and linear model regression with 95% confidence bounds for the regression function are shown in Figure 4.6. The 95% prediction bounds suggests that there is a 95% chance that water content-dielectric constant relationship function will fall in the envelope formed by red-dotted lines, which gives a water content error no greater than $\pm$0.005 or 0.5% by volume for a given dielectric constant.

Table 4.4 Statistics of linear regression (fit 1)

Estimated Coefficients:	Estimate	SE	tStat	pValue
Intercept	0.00933	0.0063814	1.4621	0.15153
b	0.012679	0.00057017	22.238	3.944e-24

SE: standard error
tStat: t-statistic
Significance at pValue<0.05
Number of observations: 42, Error degrees of freedom: 40
Root Mean Squared Error: 0.00642
R-squared: 0.925, Adjusted R-Squared 0.923
F-statistic vs. constant model: 495, p-value = 3.94e-24

Hence, the dependence of water content on dielectric constant is given by Equation 4.1.

$$\theta = 0.012679\kappa + 0.00933 \quad (4.1)$$

It can be seen from Figure 4.6 that the linear model developed in this study has a similar trend with the model developed by Korhonen et al. (1997). However, for a given dielectric constant, the linear model in this study gives a higher volumetric water content (about 0.6) comparing to

the model presented by Korhonen et al. (1997) . As discussed earlier, bonded water has lower dielectric constant than bulk water. Compared to Korhonen's experiment, the concrete used in this project has finer aggregates, more like mortar, which gives the material larger specific area and thus more bonded water and therefore an overall higher water content in the measured dielectric constant range.

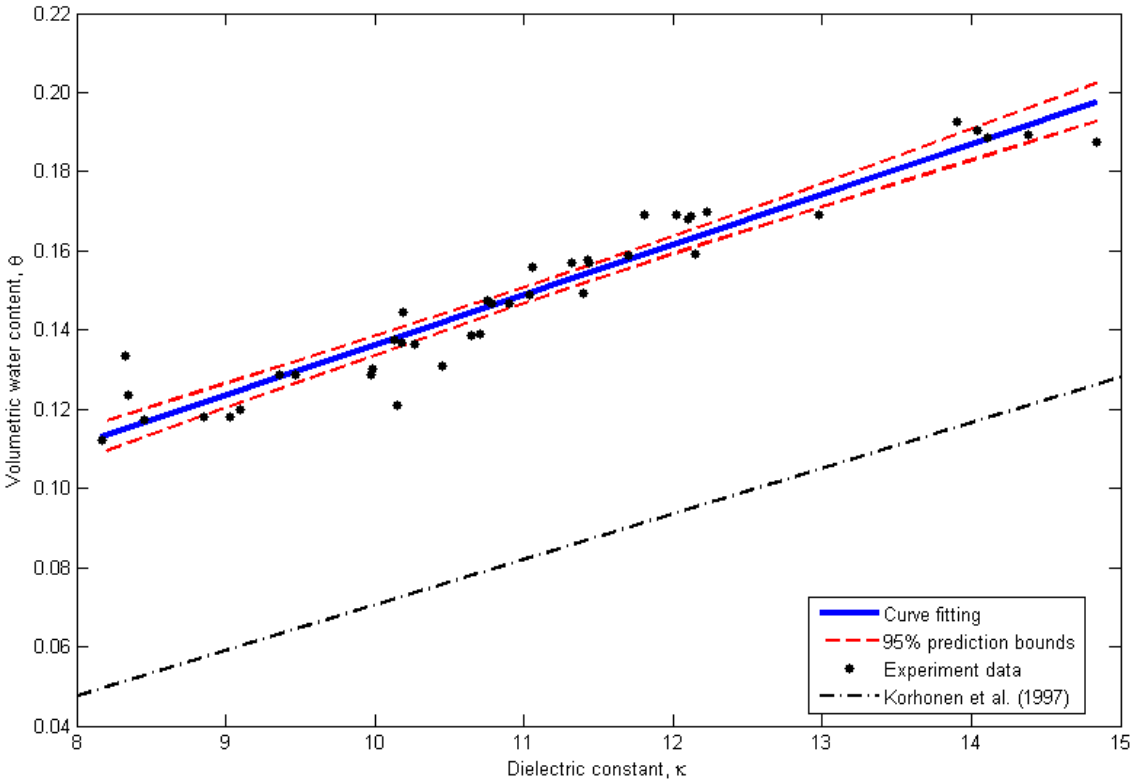

Figure 4.6 Water content-dielectric constant (Linear model).

4.2.3 **Chloride content and electrical conductivity relation**

Water content of six samples was recorded at seven time steps during oven drying, and the corresponding impendence measured and converted to electrical conductivity with probe constant K_p using Equation 2.46. For each sample, seven readings were made from seven pairs of probes formed by eight probes in each sample. Then five readings, excluding the two readings at

the boundaries, were used for averaging. Electrical conductivity versus water content for all six samples is shown in Figure 4.7.

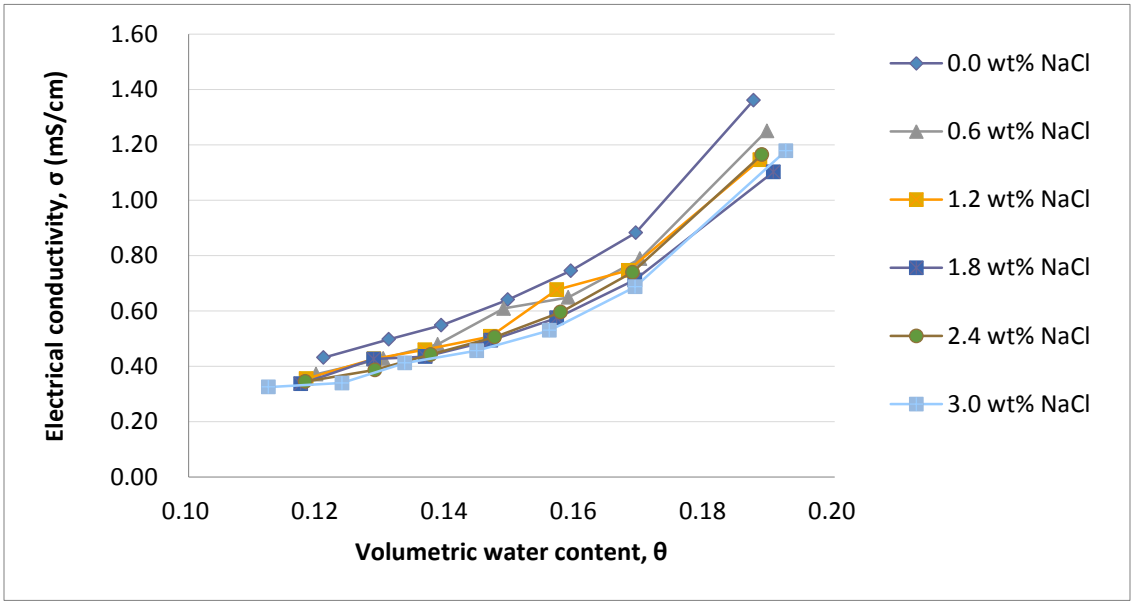

Figure 4.7 Relationship between water content and electrical conductivity

As described by Equation 2.48, the overall electrical conductivity (Ec) is a combination of the Ec of the pore solution and the Ec of the solid phase. The Ec of the solid phase is neglected because of the high impedance of dry concrete, which is over 1000 ohm, and beyond the range of impedance read by TDR system. Therefore, the overall electrical conductivity, σ, is determined only by the Ec of the pore solution, σ_a. Equation 2.50 becomes

$$\sigma = a\sigma_a \cdot \theta^2 + b\sigma_a \cdot \theta \tag{4.2}$$

where a and b are empirical constants; σ_a is the electrical conductivity of solution; the overall electrical conductivity σ is a second order polynomial function of water content, θ.

As seen from Figure 4.7, at given water content, a sample soaked in fresh water has an even higher electrical conductivity than a sample soaked in salty water. For samples soaked in salt solutions of different concentrations, the σ-θ curves weave together. This fact suggests that the Ec results measured by TDR are not very sensitive to chloride concentration in the pore solution.

This problem may be caused by the high ionic strength of the concrete pore solution due to the presence of various ionic species, such as Ca^{2+}, K^{+}, OH^{-}, in relatively high concentration, which reduces the sensitivity to the Ec change brought by chloride ions. Therefore in this project, the Ec measurement is only used as a supplementary data to the measurement of the water content change.

4.3 Water saturation change around the crack

The volumetric water content was tested with TDR following the steps described in Section 3.6.4. As shown in the Figure 4.8, the round solid marks indicate the location where probes were inserted. Every two vertical neighboring probes were employed as a two-rod probe pair to send and receive signals by a Tektronix 1502B/C Cable Tester. The surrounding lines show the signal distribution and the x marks represent the location, for which the water content was recorded. It was assumed that the water content at locations marked as x location was equal to the averaged water content for the signal covered area. For the unreinforced beams, 8 (row number) $\times$8 (column number) datasets were collected and for the reinforced beams, 6$\times$8 datasets were collected omitting the probe row at the rebar location and ignoring the last row of probes. The row of probes above and below the rebar could have been used by connecting horizontal rods in the same row. However, the signal distribution from those horizontal probes was too close to the rebar, and hence was affected by the presence of rebar causing a distortion of the waveform. Although using the non-conductive FRP-based rebar might have reduced the distortion, it brings effects on the TDR test as well for it has a very different permittivity than that of the surrounding concrete material. The significance of the effect on distortion of the waveform by other materials was not investigated in this study.

The matrix of dielectric data were collected and then converted to volumetric water content through the calibration, Equation 2.36 for both wetting cycle and drying cycle. The distribution of water content in the probed area was presented by colour-scaled images. Between the 8$\times$8 or 6$\times$8 data sets, a linear interpolation was employed to improve the data visualization.

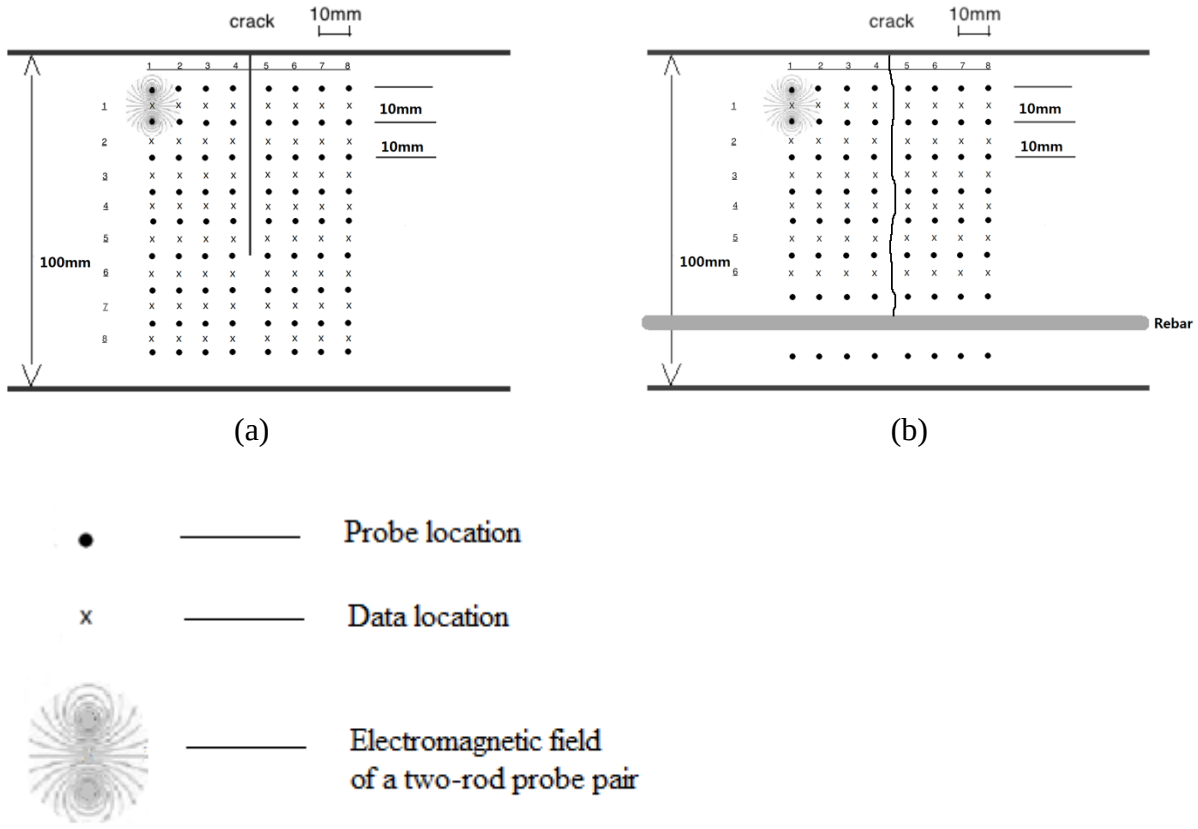

Figure 4.8 The location of data collection. (a) a schematic diagram of data grid on an artificial crack sample (b) a schematic diagram of data grid in on a natural crack sample.

4.3.1 **Wetting cycle**

Typical colour-scale plots are shown in Figure 4.9, for the saturation conditions at 5 hours of water ponding. The full records of plots for saturation from time 0 to 296 hours are attached in Appendix A. The artificial cracks are shown as a straight line at the middle position and the natural cracks are shown with two lines digitized from the real crack shape, a solid line for the front face, a dotted line for the back face, and a dash-dotted line representing the averaged crack shape of front and back cracks.

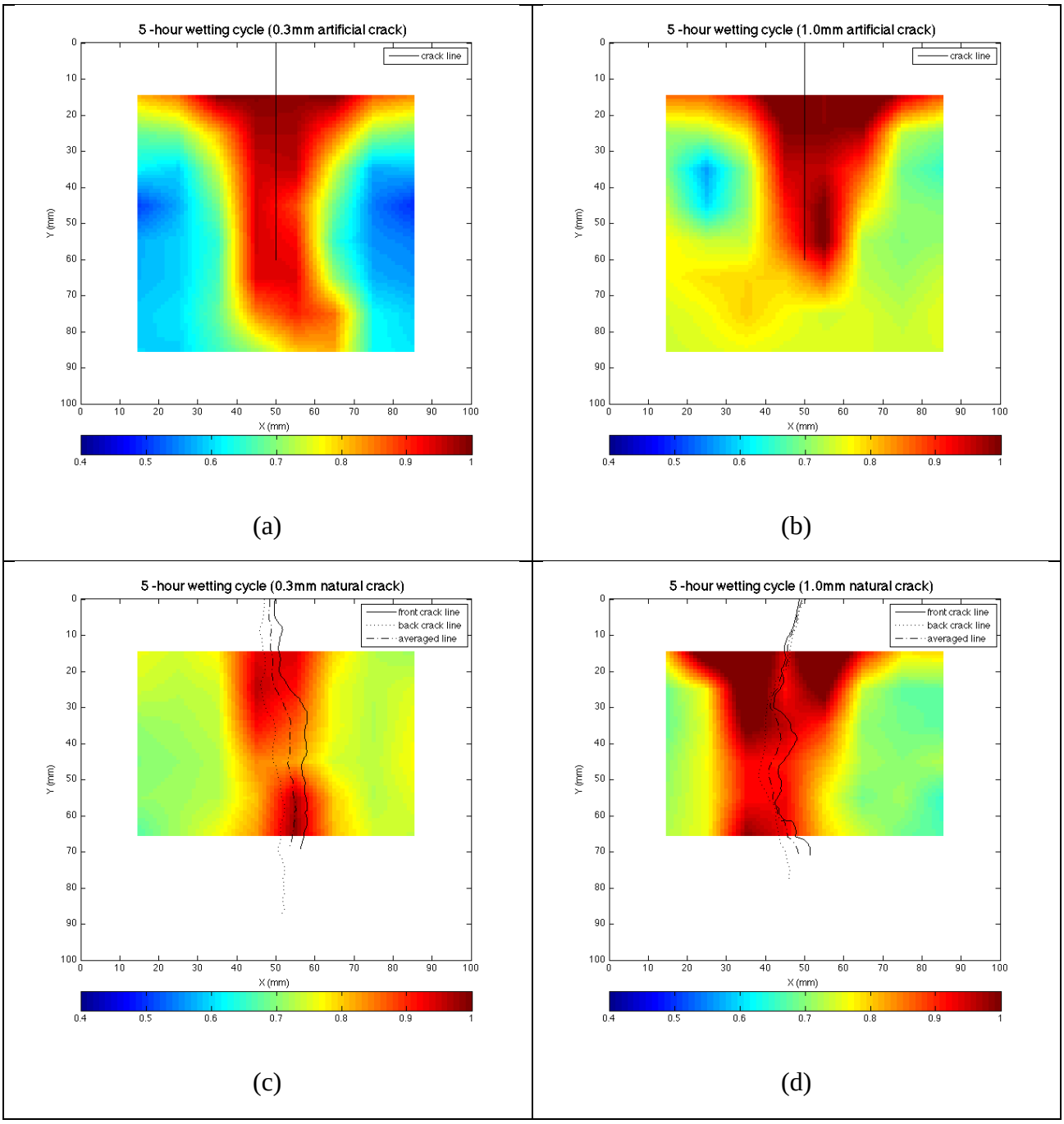

Figure 4.9 Typical colour-scaled images of the saturation conditions for concrete with 4 types of crack after 5-hour's wetting. (a) 0.3 mm artificial crack; (b) 1.0 mm artificial crack; (c) 0.3 mm natural crack; (d) 1.0 mm natural crack.

The initial saturation condition for the air-dried samples, at ambient conditions in the lab, ranged from 0.4 to 0.7. Drier areas were found near the crack. The water penetration proceeded at a fairly high rate: From air-dried state, 4 samples with different types of cracks reached full saturation at 296 hours (about 12 days). In the first hour, water saturation started quickly at the cracks' surface except for the natural crack with 0.3 mm opening, which may be caused by trapped air in the narrow crack. It can also be observed that, in a finer scale water penetrates through a "preferred path". For example, higher levels of saturation are seen at the locations [x,y]=[70,70],[35,70] in Figure 4.9 (a), (b), which is different than the ideally distributed water contour plots shown by simulations (Section 5.5). This is probably due to the localized micro cracks generated during the shim pull-out when the artificial cracks were generated or due to a non-uniform compaction around the shim insertion. For samples with artificial cracks, the water penetration front agrees well with the crack geometry and sample symmetry as the water front profile is close to a 2D diffusion problem from both the top open surface and the crack surface. For samples with natural cracks, because of the 3D geometric crack and possible damage in the matrix near the crack, it is acting more like a "cracked zone" with a higher permeability, on average.

4.3.2 **Drying cycle**

The typical colour-scaled plots for the saturation conditions at 695 hours of exposure to ambient air at in a RH=40±2% room condition, are shown in Figure 4.10. The full records of the plots of saturation from time 0 to 2855 hours (about 119 days) are attached in Appendix B. The artificial cracks are shown as a straight line at the middle position and the natural cracks are shown with two lines digitized from the real crack shape, a solid line for the front face, a dotted line for the back face, and a dash-dotted line representing the averaged crack shape of front and back cracks.

The drying phase started from a fully saturated condition. In the drying phase, water was lost from the sample at a much lower rate than the infiltration of water in the wetting phase. It took 2855 hours (about four months) for the sample to reach a saturation state similar to the air-dried initial value in the wetting phase, while it only took less than two weeks for those air dried samples to reach full saturation according to the wetting history (Appendix A). For both artificial crack samples and natural crack samples, water loss took place at a faster rate around the larger

cracks. For the artificial ones, the "faster-dried region" did not have the same length as the length of the crack (60 mm) because of the water content values gained from TDR are averaged with the value of non-cracked part (60 mm deeper from the open surface); for natural ones, the driest regions were more closely confined around the cracking paths as the crack goes through the whole data mapping area.

4.3.3 **Effects of cracks on saturation profile**

In order to compare the effect of cracks on the water flow, the profiles of saturation are presented as saturation vs. distance from the crack for wetting and drying phases (wetting: Figure 4.11, Figure 4.12; Drying: Figure 4.13, Figure 4.14). Three depth levels of 15 mm, 35 mm and 65 mm were chosen, to get insights into concrete near the surface, inside the sample, and at the depth where the crack ends. Results are compared among the artificial cracks and natural cracks.

In the first hour, water quickly occupied the near-crack area, as seen in Figure 4.11 and Figure 4.12. In the horizontal direction, the drastic water content change stopped at around 15 mm from the crack and about the same distance from the open exposed surface in the vertical direction (the depth) for both artificial crack samples and natural crack samples. An exception to this response was observed for A10 sample at a depth of 65 mm and N03 sample at a depth of 65 mm, where it manifested a gradual saturation increase instead of that steep water content gradient, which suggests a faster water distribution near the crack tip. This may be caused by the localized damage at the crack tip. In the vertical direction, at depth 15 mm no overall sudden increase of saturation is observed, which indicates that the waterfront has not reached yet, or has just reached the depth of 15 mm. At 8 hours, an overall saturation increase can be observed at depths of 15 mm and 35 mm, while no significant saturation change can be seen at a 65 mm depth at distance of 55 mm and 65 mm from the crack. This suggests that the water front is between 35 mm and 55 mm deep in both directions. In summary, both crack types and crack widths have similar effects on the water saturation profile.

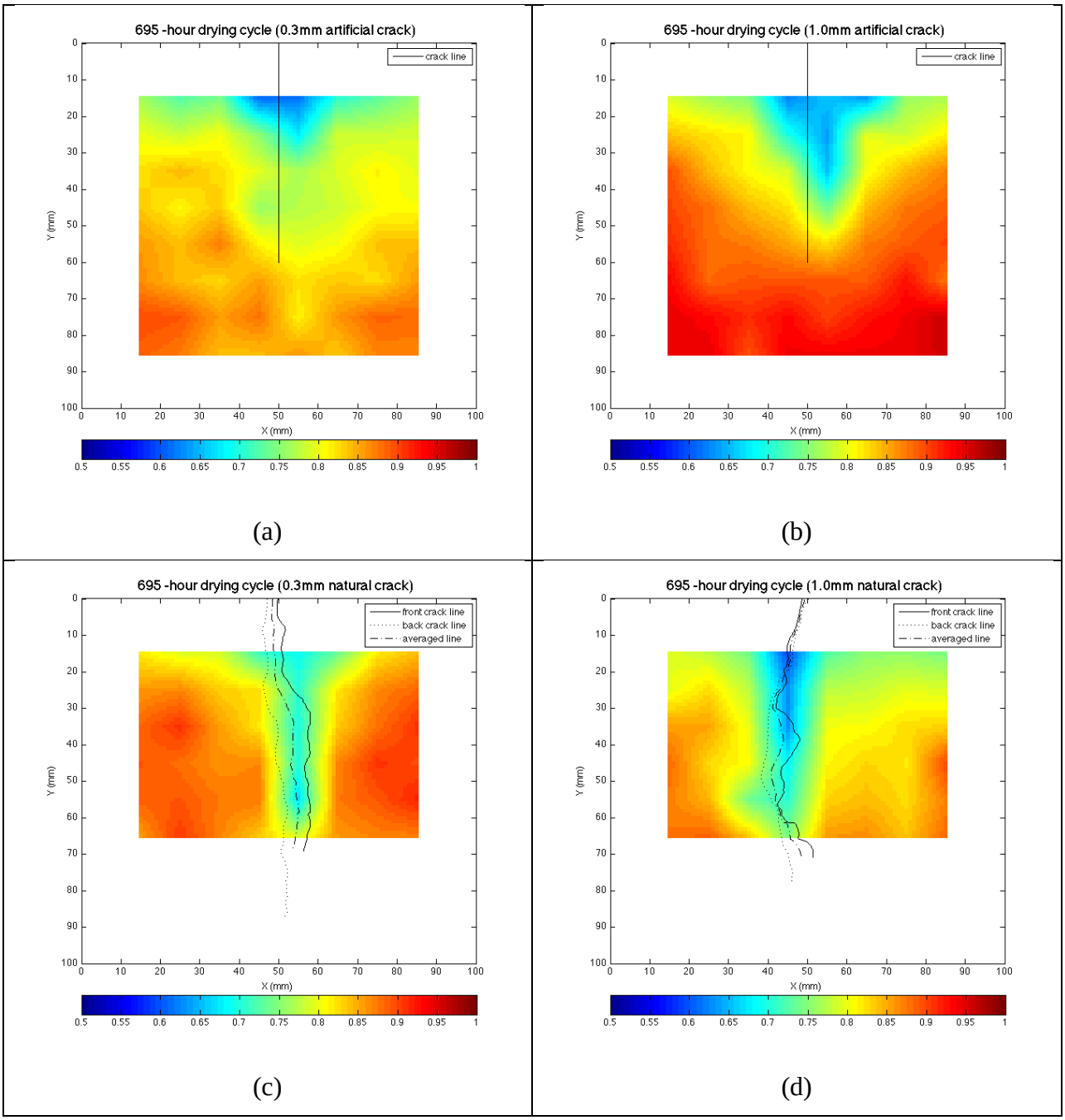

Figure 4.10 Typical colour-scaled images of the saturation conditions for concrete with 4 types of crack after 695-hour's drying. (a) 0.3 mm artificial crack; (b) 1.0 mm artificial crack; (c) 0.3 mm natural crack; (d) 1.0 mm natural crack.

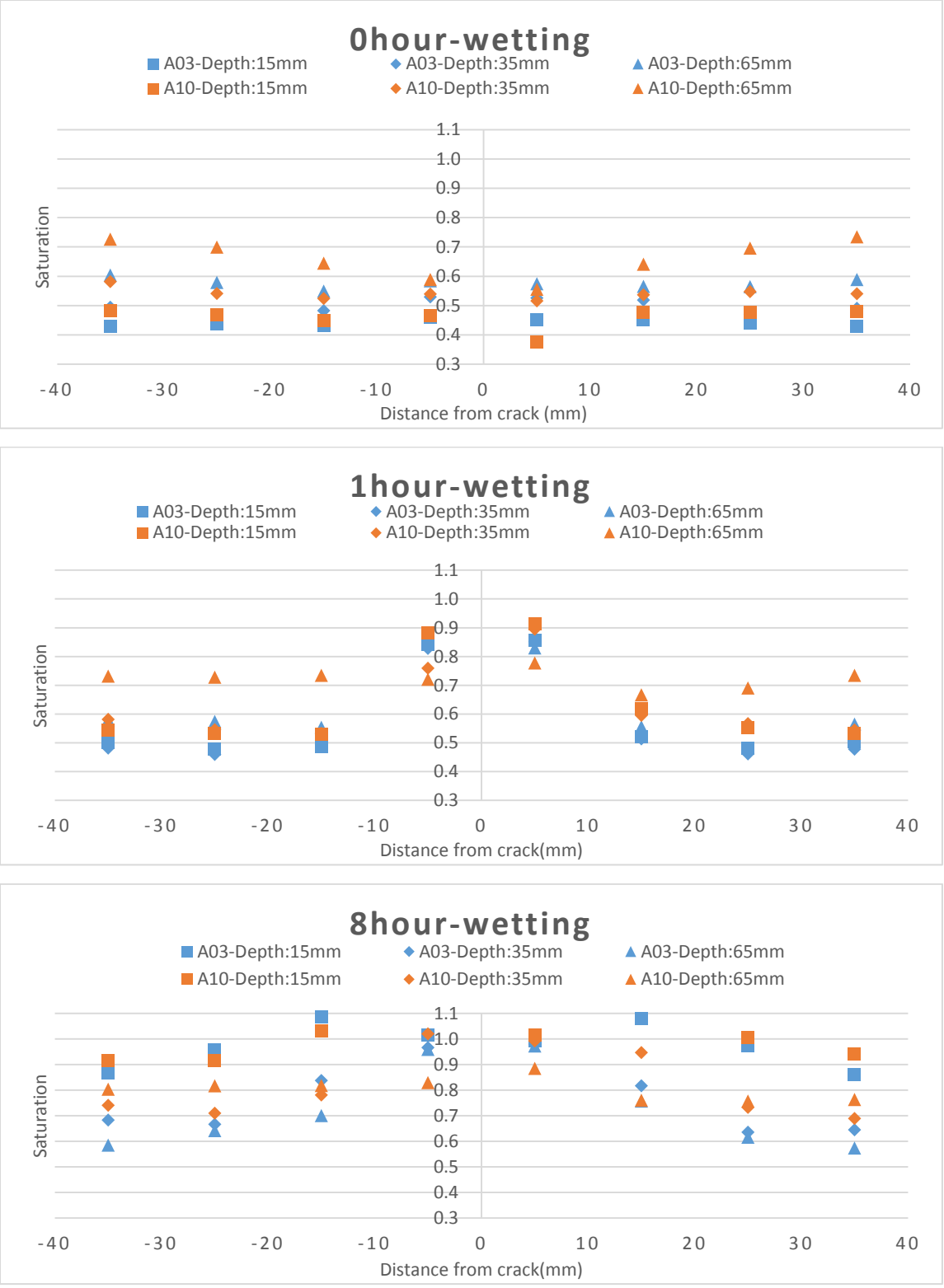

Figure 4.11 Saturation profile of artificial crack samples at 0, 1, 8 hours in the wetting phase (A03: 0.3 mm artificial crack, A10: 1.0 mm artificial crack, N03: 0.3 mm natural crack; N10: 1.0 mm natural crack).

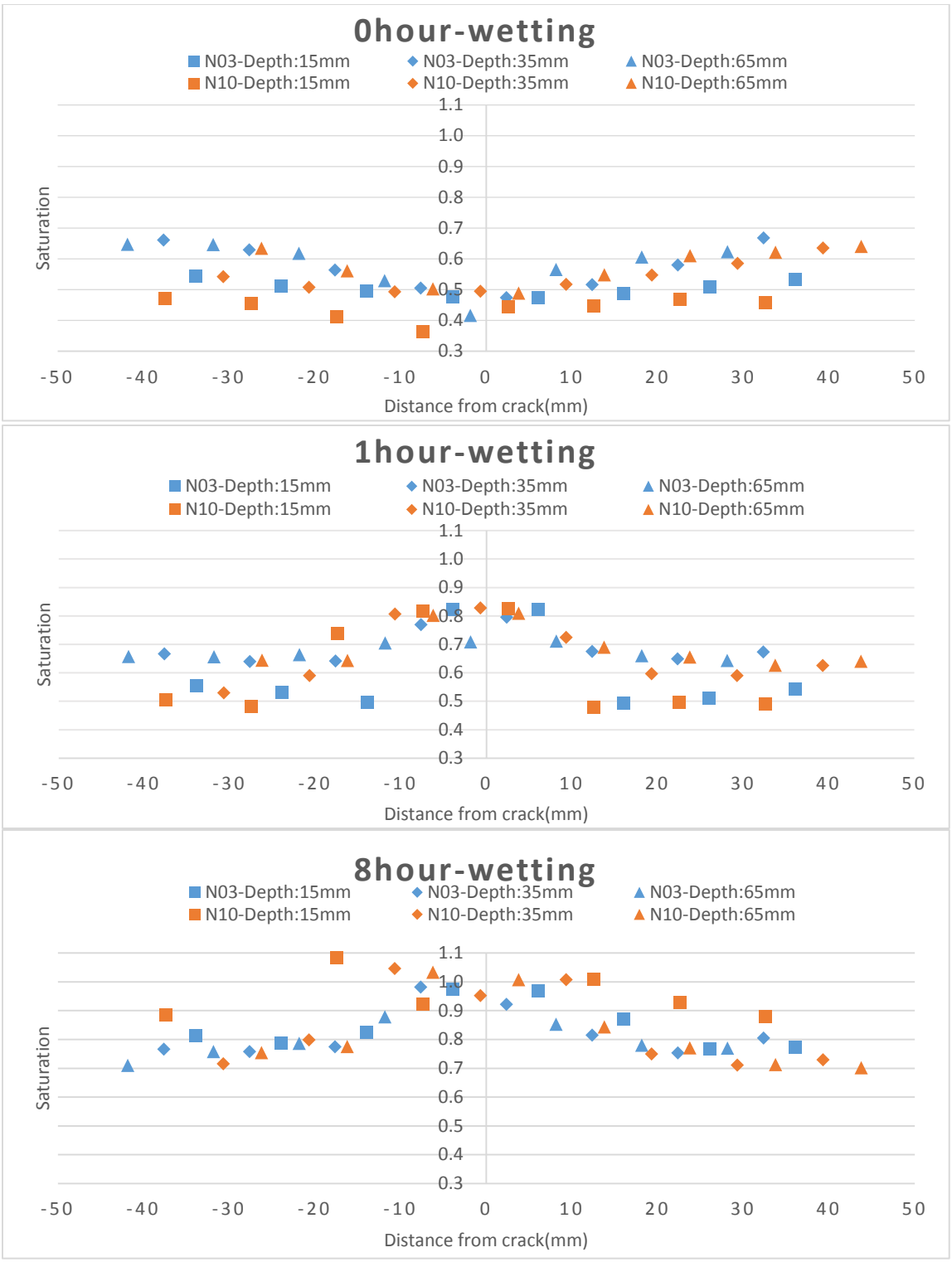

Figure 4.12 Saturation profile of natural crack samples at 0, 1, 8 hours in the wetting phase (A03: 0.3 mm artificial crack, A10: 1.0 mm artificial crack, N03: 0.3 mm natural crack; N10: 1.0 mm natural crack).

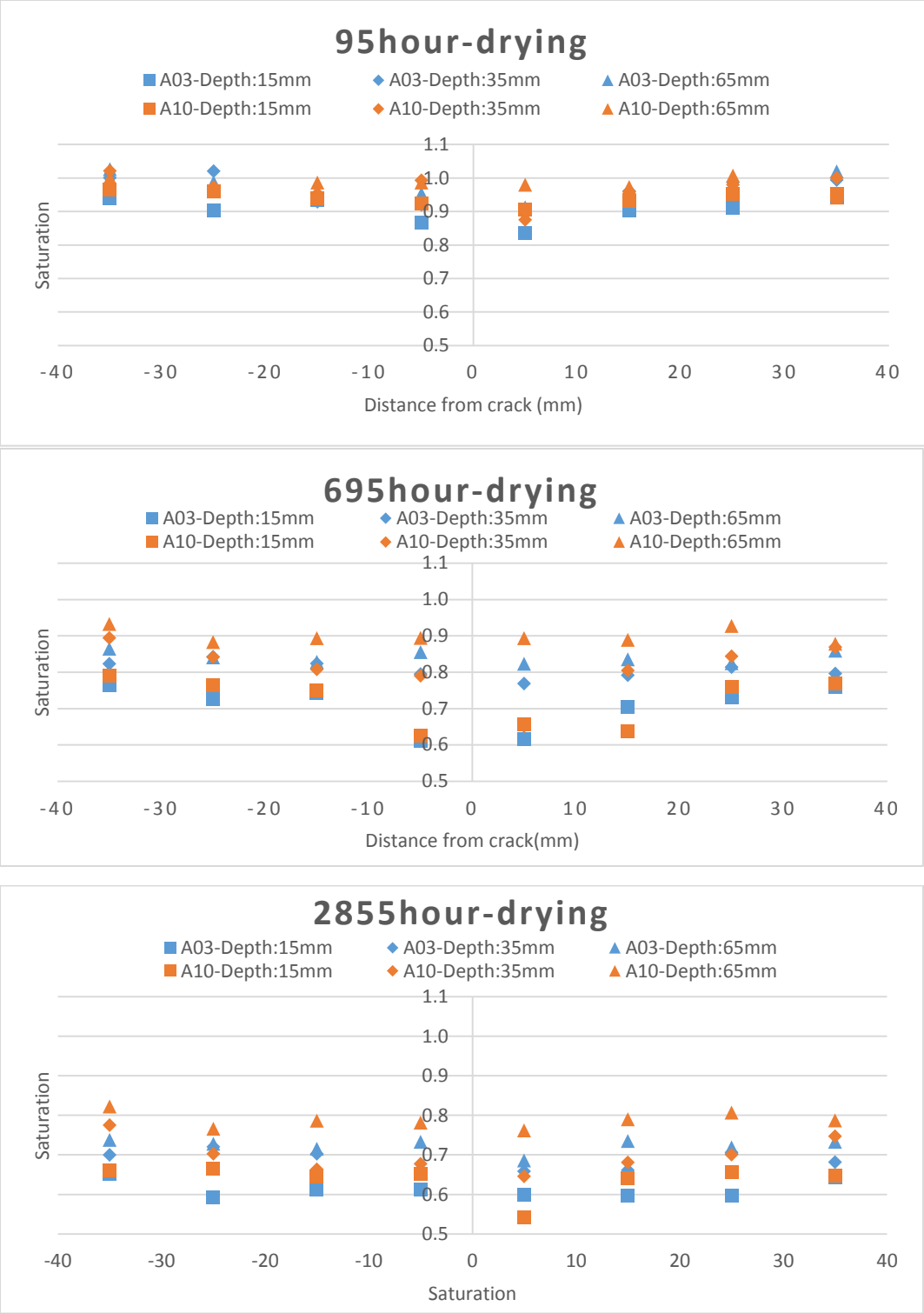

Figure 4.13 Saturation profile of artificial crack samples at 95, 695, 2855 hours in the wetting phase (A03: 0.3 mm artificial crack, A10: 1.0 mm artificial crack, N03: 0.3 mm natural crack; N10: 1.0 mm natural crack).

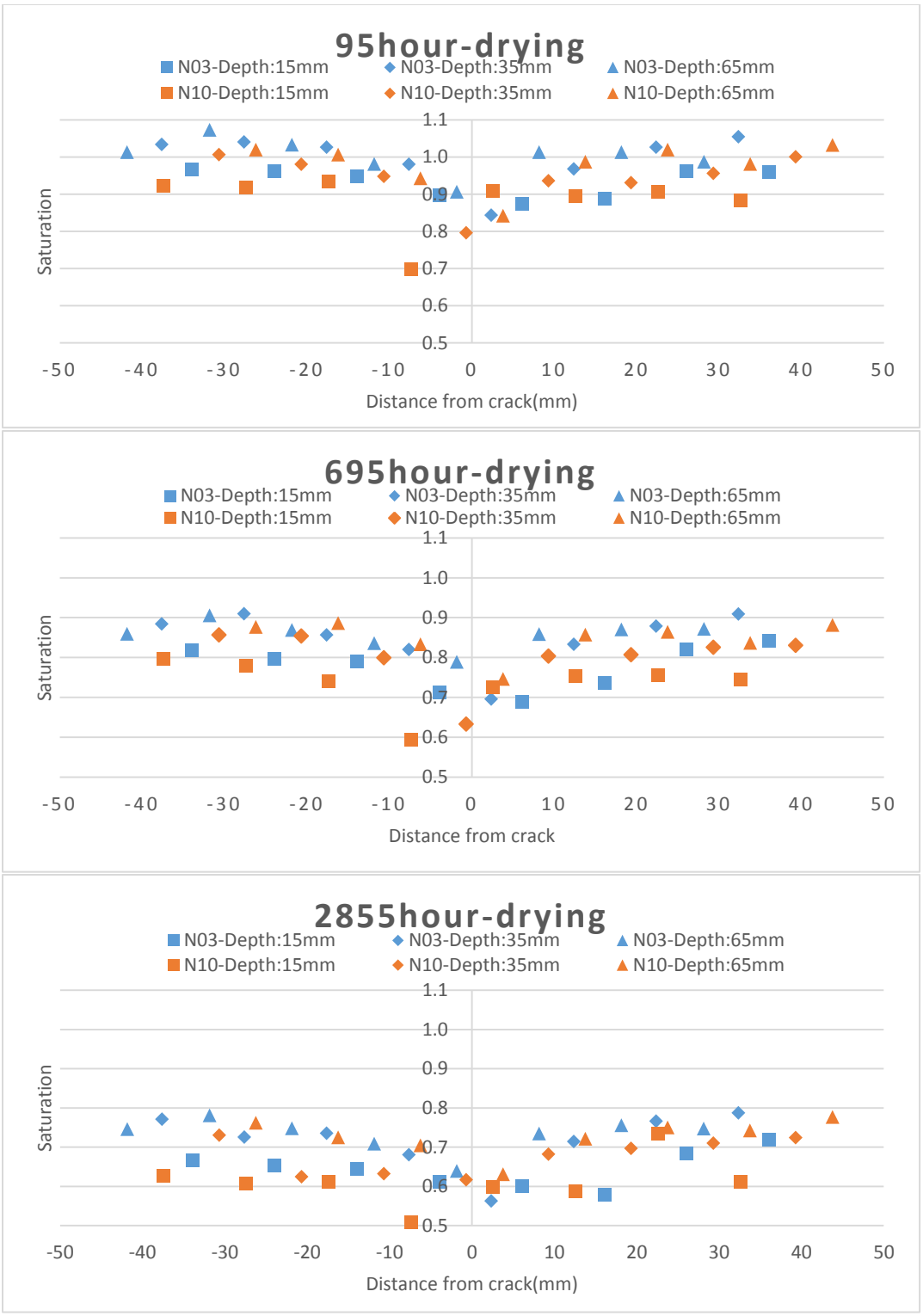

Figure 4.14 Saturation profile of natural crack samples at 95, 695, 2855 hours in the drying phase (A03: 0.3 mm artificial crack, A10: 1.0 mm artificial crack, N03: 0.3 mm natural crack; N10: 1.0 mm natural crack).

As seen in Figure 4.14, a sudden drop of saturation can be observed in natural crack samples at all depths within about 10 mm from the crack at 95, 695, and 2855 hours. For the artificial crack (Figure 4.13) a similar sudden drop is also observed at depth of 15 mm and 35 mm. However, it is not as sharp as the one observed in natural crack samples. This does not mean the water loss was lower in the artificial crack samples. This observed difference is caused by the TDR signal resolution. For the artificial crack samples, the near-crack probe is evenly distributed in a column, 5 mm from the crack surface and the drastic change of water content within that 5 mm may not be captured from the sampling volume. Because of this phenomenon and slow rate of drying, it is not possible to compare the "drying front" at the beginning of the drying phase. For natural crack samples, the larger crack size gives faster overall drying rate around the crack and the difference change in a reduced manner as time goes to 2855 hours (4 months). This is probably due to the fact that the tip of the natural crack has a very small crack width and water stored there slows the evaporation from the concrete matrix. For artificial crack samples this crack size effect does not appear.

4.4 Does the crack act as a free surface?

In order to find out if the crack surface behaves like the upper open surface, the saturation change versus time is plotted in Figure 4.15 (wetting) and Figure 4.16 (drying) at near-surface, noted as "exp-s"[15mm, 35mm], and near-crack, noted as "exp-c"[35mm, 15mm]([vertical depth, horizontal depth]). The "exp-s" point is the location where water content change was mainly due to surface transport, and exp-c point is the location where water content change was mainly due to crack transport. The saturation values are averaged from the left and right sides of the crack.

The results show that larger variations are found for the cracks with 1 mm surface openings in the first 40 hours. The saturation changes look very similar for both the near-surface point and the near-crack point, which suggests that water transport through open surface and through the crack surface have a similar behaviour.

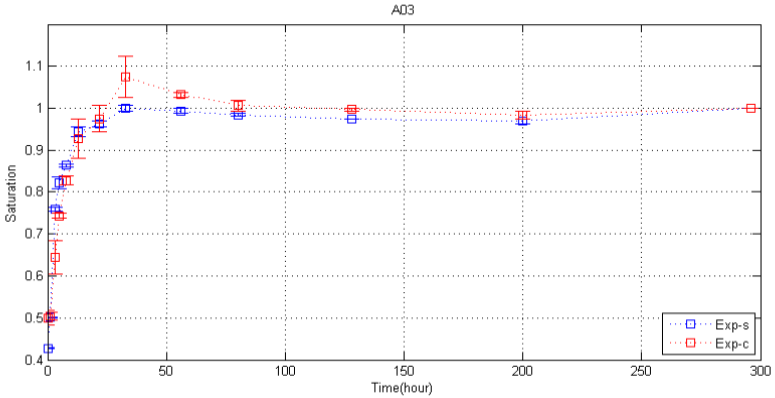

(a)

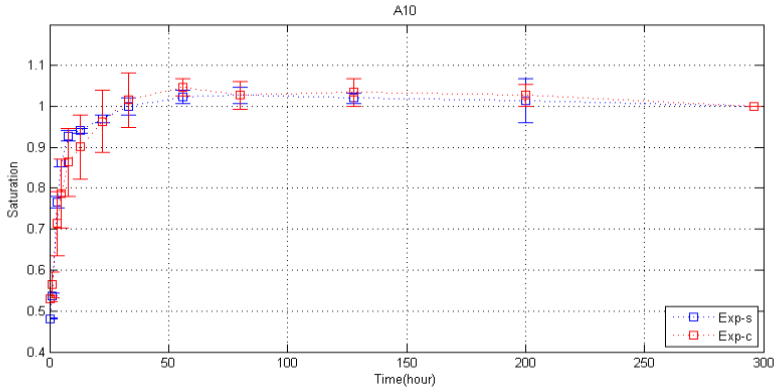

(b)

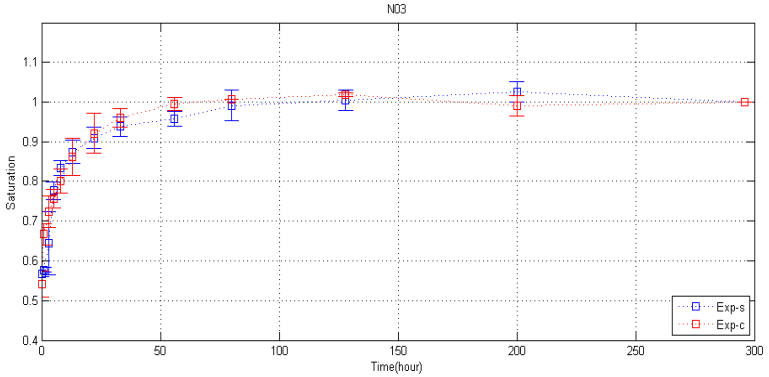

(c)

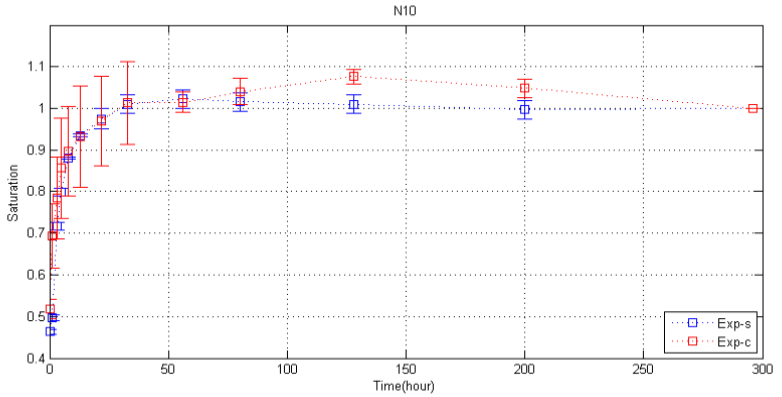

(d)

Figure 4.15 Saturation change vs. time for near-surface point (exp-s) and near-crack point (exp-c) in the wetting phase. (a) A03: Artificial crack with surface crack opening of 0.3 mm; (b) A10: Artificial crack with surface crack opening of 1.0 mm; (c) N03: Natural crack with surface crack opening of 0.3 mm; (d) N10: Natural crack with surface crack opening of 1.0 mm).

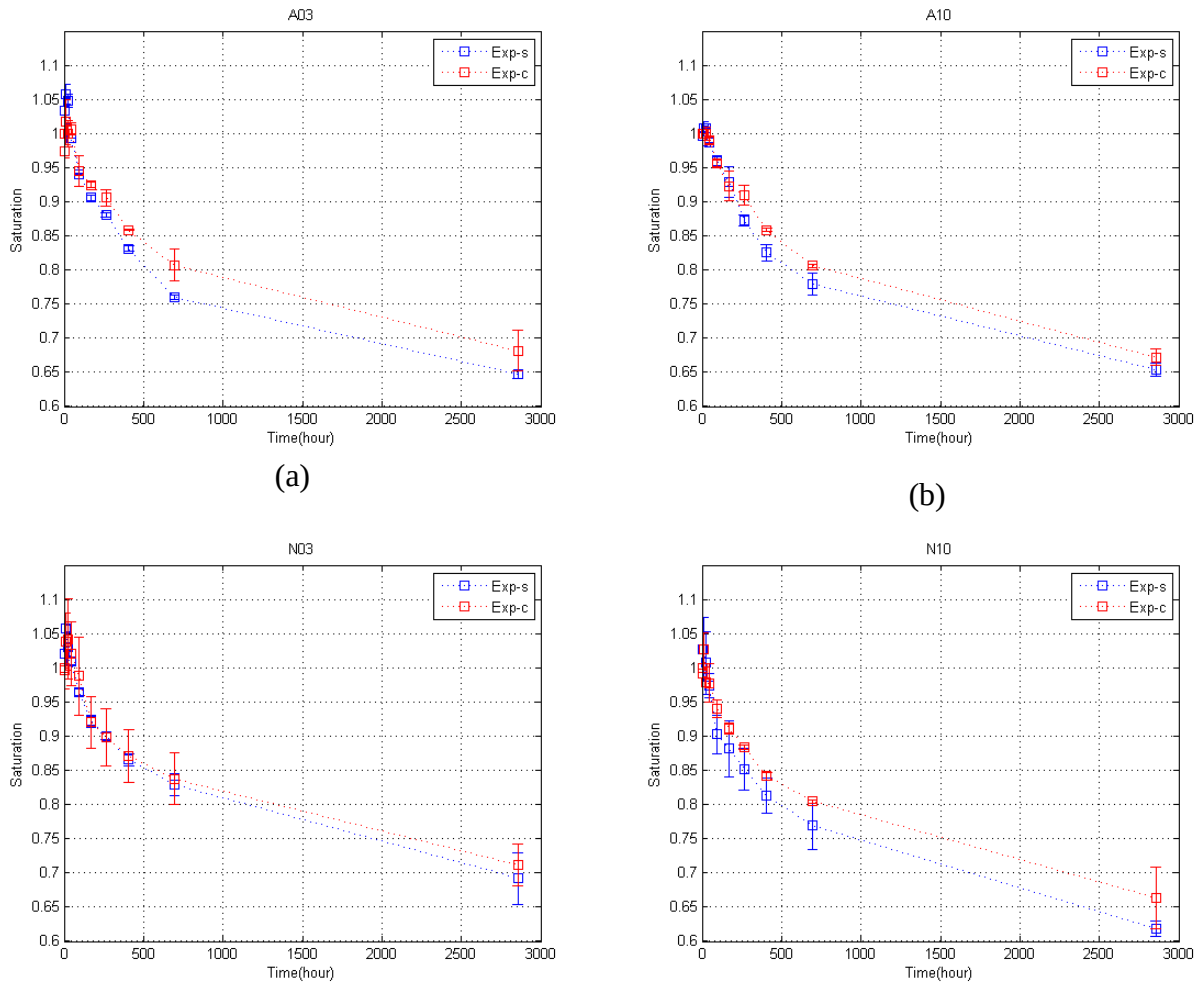

Figure 4.16 saturation change vs. time for near surface point (exp-s) and near crack point (exp-c) in the drying phase. (a) A03: Artificial crack with surface crack opening of 0.3 mm; (b) A10: Artificial crack with surface crack opening of 1.0 mm; (c) N03: Natural crack with surface crack opening of 0.3 mm; (d) N10: Natural crack with surface crack opening of 1.0 mm).

Also, for the drying phase, it can be seen from Figure 4.16 for all types of cracks. Drying rate at the near-surface point is slightly larger than that at the near-crack point. The maximum difference is 0.05 in saturation level. This shows that it would be reasonable to assume the crack behaves like an open free surface without a very large error in water saturation levels.

4.5 Summary

The hydraulic conductivities of the crack concrete samples were tested by the tension infiltration technique. It was found that the presence of cracks (0.3 mm and 1.0 mm) dramatically increased the value of the hydraulic conductivity of concrete (by up to 5 orders of magnitude). The effect of crack roughness was found to be more significant for small crack openings. However, for larger cracks, this effect did not affect the hydraulic conductivity significantly.

A Time Domain Reflectometry (TDR) test was developed for monitoring the evolution of water saturation around the crack over time. A proper calibration was conducted to find the relationship between dielectric constant and volumetric constant. However, the electrical conductivity measured by TDR was insensitive to the chloride concentration in the pore solution. This may have been caused by the high ionic strength in the concrete pore solution, which may act as background noise that over shadows the Ec change brought about by the chloride ions, making the change of Ec comparable to the experimental error.

The evolution of water saturation of the cracked concrete under wetting and drying conditions was analyzed as colour-scaled images and the water saturation contours were compared for different crack openings. For the artificial crack samples, a deviation from the expected "perfectly symmetric" flow regime around a straight crack was observed. This was probably caused by the micro cracks induced during the shim pull-out process or a non-uniform compaction around the shim insertion. For the natural cracks, in the drying phase, smaller cracks seemed to have better water storage. Hence, the water saturation decreased at a slightly slower rate.

The water saturation profiles were compared among samples with different crack types and sizes. It is found that both crack types and crack widths have similar effects on the water saturation profile. Also it is comfirmed by the comparison between the saturation change over time in the near-surface location and near-crack location. The results show that the saturation changes in a similar way for both the near-surface point and the near-crack point, which suggests that it would be reasonable to assume the crack behaves like an open free surface without a very large error in water saturation levels.

5 Numerical Modelling

5.1 Introduction

Macrocracks in concrete generally serve as fast pathways for the ingress of chlorides and lead to premature corrosion. Many findings (Alekseev et al., 1993; Frederiksen, 1993; Jaffer & Hansson, 2009; Pettersson, 1996) support the fact that cracking leads to a reduction of initiation period of corrosion. The limited amount of previous research on corrosion in cracked concrete has been restricted to measuring either potentials (for assessing the likelihood of corrosion) or corrosion rates in either field structures or preconditioned samples (often subjected to wetting/drying cycles) in the lab, without monitoring the distribution of the water saturation and chlorides around the crack. Therefore, the water flow in the cracked concrete needs to be investigated to have a better understanding of the cracked reinforced concrete corrosion.

The permeability of cracked normal strength concrete and high strength concrete significantly increases with increasing crack widths. There have been various theories proposed to model the flow and transport in fractured porous media and could be grouped in two categories: smeared approaches and discrete approaches. The smeared approaches treat the cracked concrete as a monolithic continuum whose transport properties are some average of the transport properties of the matrix and those of the crack. The discrete approach represents the crack separately from the concrete matrix as a free space or an equivalent porous medium with different transport properties. In this study, the discrete approach was used to investigate the effect of cracks on the unsaturated flow properties of concrete.

The objectives of this chapter are as follows:

1) To investigate if the fractured concrete displays a hysteretic behaviour for saturation, permeability, or both in the exposure environment involving wetting/drying scenarios;

2) To determine the constitutive relations, such as saturation vs. pressure head (known as the water retention curve) and the relative permeability vs. pressure head relationship for wetting/ drying flow regimes;

3) To determine whether a 1D representation of the crack in a 2D model of the cracked beam is sufficient to capture the essential features of the system's behavior; and

4) To compare the results of prediction where the crack is treated as "an equivalent porous medium" with the case where the crack is approximated as a free surface.

5.2 Governing equations

The water saturation and desaturation phenomena in cracked concrete are simulated as a 2D problem of water flow in a porous medium. The Richard's Equation application module, which analyzes flow in variably saturated porous media, was employed. With variable saturation, the hydraulic properties change as fluids move through the medium. Various models have been proposed in the literature to define the relationship between water content θ, effective saturation Se, and relative permeability Kr. The Van Genuchten (1980) model, together with the Brooks and Corey (1966) model are among the most widely used ones. The Van Genuchten model as summarized in Section 2.2.1.1 has been used before in the field of concrete research and has proven to be effective in describing the unsaturated hydraulic properties of concrete. Therefore, it was chosen in the simulation model. Richard's equation (Equation 5.1) and the Van Genuchten models for relative permeability (Equation 5.2) and capillary pressure (Equation 5.3) are listed below for the convenience of the reader.

$$\frac{\partial(\theta_s S_l)}{\partial t} = -\nabla\left[\frac{k \cdot k_r}{\mu_l}(\nabla P_l + \rho_l g \nabla D)\right] \tag{5.1}$$

$$k_r = \sqrt{S_e}\left[1 - \left(1 - \sqrt[m]{S_e}\right)^m\right]^2 \tag{5.2}$$

$$P_l = -\frac{1}{\alpha}\left[(S_e)^{-\frac{1}{m}} - 1\right]^{\frac{1}{n}} \tag{5.3}$$

$$S_e = \frac{S_l - S_{lr}}{1 - S_{lr}} \tag{5.4}$$

where, $\theta_s$is the water content at full saturation; k_r is the relative permeability; S_e is the effective saturation of the liquid; P_l is the capillary pressure of the porous medium; S_l is the degree of

saturation in the porous medium, and S_{lr} is the residual saturation of the porous medium; D represents the vertical coordinate; m, n and α are empirical parameters (m=1-1/n).

The crack was geometrically modelled as a single line (or curve). When modelling a surface crack as an open channel domain, Navier-Stokes equations could be used to represent water flow in the crack and Darcy's Law or Richard's equation for the matrix. This approach is very computationally intensive, and hence, rarely used with large specimens, especially under unsaturated conditions where a multiphase model would be needed. However, as shown in the previous chapter, the hydraulic behaviour of a discrete crack was very similar to that of the free surface that was exposed to the wetting or drying environment. Hence, in this study the crack line was directly subject to the boundary conditions like the free surface.

The crack can also be modelled as an equivalent porous medium whose hydraulic and transport properties are such that they can simulate the effect of a crack. Computationally, this approach is less intensive than the one using the Navier-Stokes equations but should be more intensive than the approach where a surface crack is treated as an external boundary. The equivalent porous medium approach was also used in this study. The crack line was assigned with a hydraulic conductivity measured in the infiltration test (Table 4.1) and the relative permeability k_r, was developed according to Boulfiza et al. (2003) as follows.

For a parallel-wall crack model, the hydraulic conductivity is proportional to the cubic power of the crack width:

$$K^{cr} = \frac{\rho g}{12\eta} w^3 \tag{5.5}$$

where K^{cr} is the hydraulic conductivity of a crack; ρ is the density of liquid; η is the viscosity of liquid; w is the crack width and g is the gravitational acceleration. It can be further developed to a crack width that varies continuously along the crack

$$K^{cr} = \frac{\rho g}{12\eta} L \int_0^{\infty} w^3 f(w) dw \tag{5.6}$$

where, $f(w)$ is the frequency distribution and L is the crack length

Under unsaturated conditions, there is a threshold width, w_s, such that portions of the crack with openings larger than w_s is drained, under a certain pressure head, H_p:

$$w_s = \sqrt{\frac{2\gamma\, cos\theta}{\rho g|Hp|}} \tag{5.7}$$

Therefore, Equation 5.6 can be extended to the unsaturated conditions as

$$K^{cr}(Hp) = \frac{\rho g}{12\eta} L \int_0^{w_s} w^3 f(w) dw \tag{5.8}$$

The relative permeability can therefore be expressed as the ratio of hydraulic conductivity in unsaturated condition to that in the saturated condition.

$$K_r^{cr}(Hp) = \frac{\int_0^{w_s} w^3 f(w) dw}{\int_0^{\infty} w^3 f(w) dw} = \frac{1}{2} Erfc\left(\frac{log\frac{w_0}{w_s} + \sigma^2 ln1000}{\sqrt{2\sigma^2}}\right) \tag{5.9}$$

where, $Erfc$ is the complementary error function $Erfc(x) = 1 - Erf(x)$, and Erf is the error function, w_0 is the most probable value of crack width, and σ is the standard deviation of the logarithm crack width distribution.

5.3 Model setup

5.3.1 Geometry and mesh

All models were built in "COMSOL Multiphasics 3.5a". The geometry of the model was set according to the cracked beam samples used in the experimental test. It was a 0.1 m×0.4 m rectangular domain representing the concrete beam with a crack at the midspan [Figure 5.1(a)] where the straight line represents the artificial crack. The red-boxed area can be replaced by the natural crack line meshes. As shown in Figure 5.2 (a), the curved lines represent the natural crack for all front, back and numerically averaged crack line in the natural crack model. The

natural crack line was digitized from the photos of cracked beams, as shown in Figure 5.2 (b). The geometry was meshed with a set of "Free Mesh Parameters": a maximum element size of 5×10^{-3} m and a growing rate 1.2; the maximum element size limits the possible size of the largest element and the growing rate limits the size different between two adjacent elements. Mesh refinement was applied to the area near the surface and crack, where the wetting and drying boundary conditions were applied. The mesh statistics are presented in Table 5.1. All the models were meshed in to 13675-18239 triangular elements; the number of boundary elements was between 330 and 421.

Table 5.1 Mesh statistics of the FEM models

Model type	A03/A10	N03 (Front)	N03 (Back)	N03 (Average)	N10 (Front)	N10 (Back)	N10 (Average)
Number of degrees of freedom	13675	18923	19547	16804	19769	16280	18239
Number of mesh points	3494	4805	4964	4275	5016	4146	4634
Number of elements	6688	9314	9620	8255	9738	7989	8972
Triangular	6688	9314	9620	8255	9738	7989	8972
Number of boundary elements	330	405	416	367	421	385	394

A03/A10: artificial crack model
N03 (Front): natural crack model with the front crack line of the 0.3 mm natural crack specimen
N03 (Back): natural crack model with the back crack line of the 0.3 mm natural crack specimen
N03 (Average): natural crack model with the averaged crack line of the 0.3 mm natural crack specimen
N10 (Front): natural crack model with the front crack line of the 1.0 mm natural crack specimen
N10 (Back): natural crack model with the back crack line of the 1.0 mm natural crack specimen
N10 (Average): natural crack model with the averaged crack line of the 1.0 mm natural crack specimen

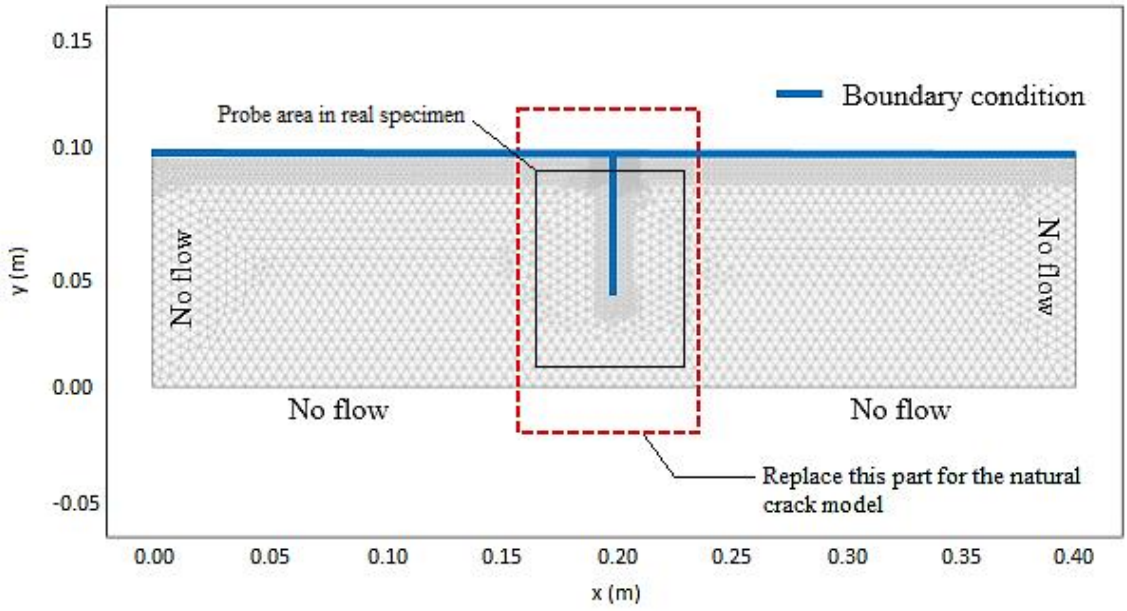

(a)

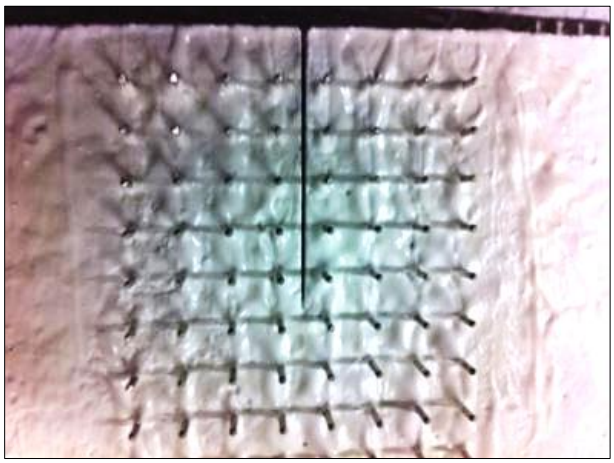

(b)

Figure 5.1 Artificial crack model (A03 and A10). (a) Schematic model representation; (b) A picture of the real specimen with TDR probes.

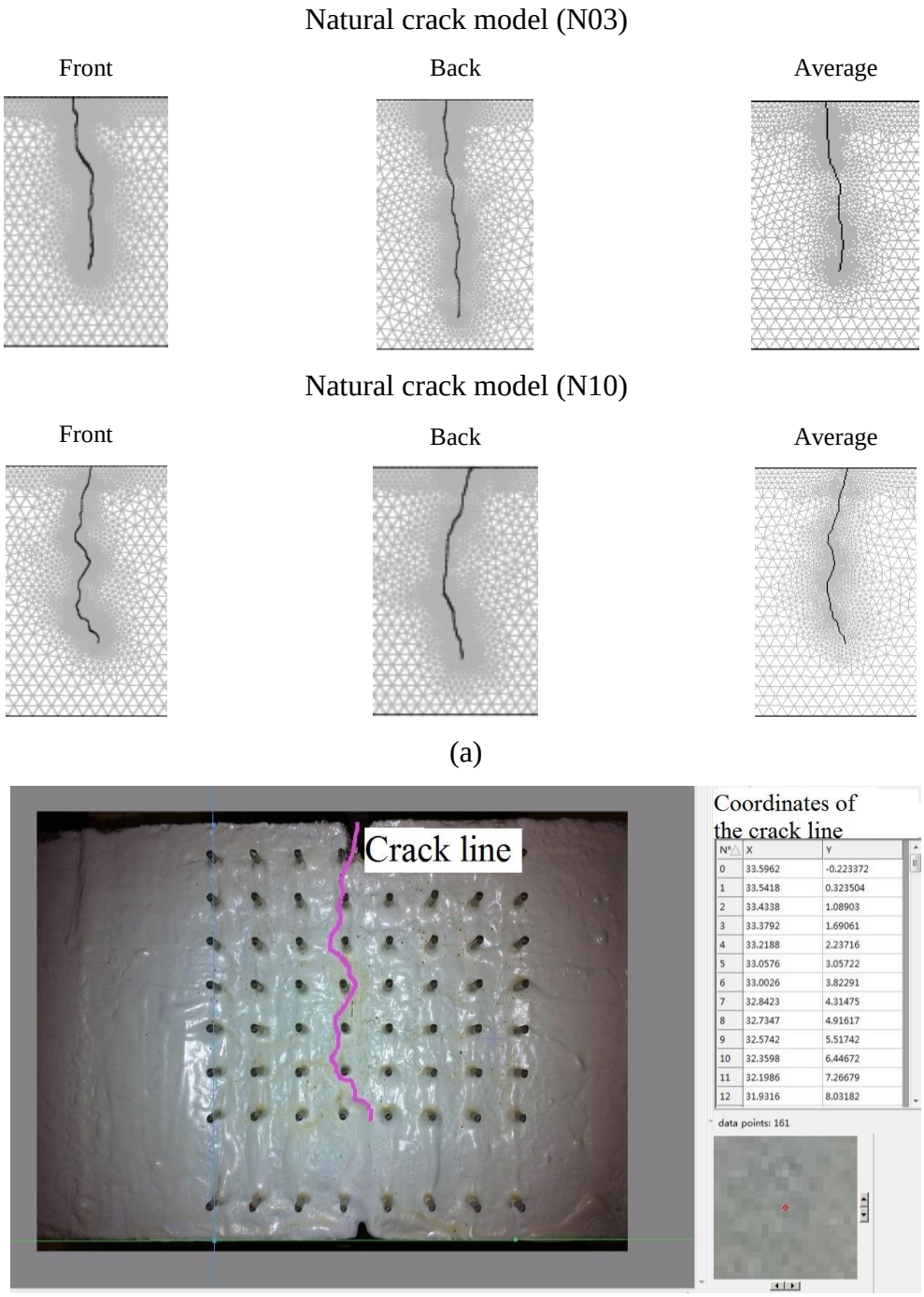

Figure 5.2 Natural crack model near the crack (N03 and N10). (a) Schematic model representation (b) A picture showing digitization of the real crack.

5.3.2 **Boundary conditions**

In the model, the top line and crack line were exposed to wetting and drying boundary conditions. The other boundaries had a no flow condition imposed to represent an impermeable coating on the real samples (Figure 5.2). The boundary conditions for wetting and drying are listed in Table 5.2. Pressure head, Hp=0.05 m simulates 5 cm ponding under water, and Hp=-12776 m simulates a dry condition of RH=40% according to Kelvin equation (5.10) and Equation (2.10)

$$p = -\frac{RT}{M}\ln\left(\frac{p_v}{p_s}\right) \tag{5.10}$$

where, p is the total pressure; temperature, T =23+273.15 K; ideal gas constant, R=8.3144621×10^{-3} kg·MPa/mol/K; molecular weight of water, M =0.01802 kg/mol; p_v is the partial pressure of water vapour in an air-water mixture, and p_s is the saturated vapor pressure of water at a prescribed temperature, the ratio is RH=0.4.

The whole history of the boundary condition change is plotted in Figure 5.3 (a). The transition between the wetting and drying condition, from 0.05 m to -12776 m, was modelled using continuous first derivative smoothing over a time period of about 36 hours, as shown in Figure 5.3 (b).

Table 5.2 Wetting and drying condition settings

Boundary conditions	Type	Surface boundary	Crack boundary
Wetting	Pressure head (Hp)	0.05 m (0<t<1296000s)	0.1+0.05-y* (m)
Drying	Pressure head (Hp)	-12776 m (t≥1296000s)	0.1-12776-y (m)

*y is the coordinate of the vertical axis as seen in Figure 5.1(a)

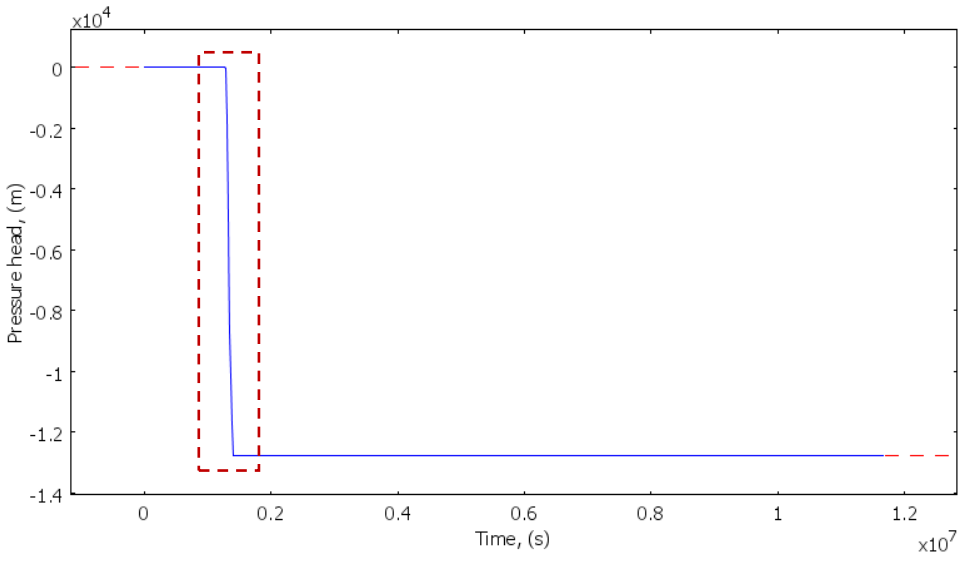

(a)

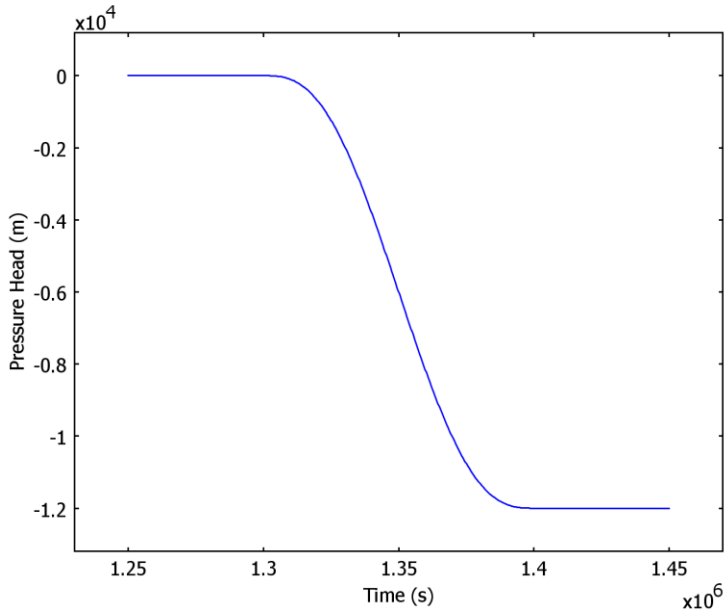

(b)

Figure 5.3 Boundary conditions for wetting and drying phases: (a) a complete wetting and drying history; (b) a zoom-in view of the smooth transition from wetting condition to drying condition.

5.3.3 **Material parameters**

Material properties used for the model are listed in Table 5.3. Porosity is the defined as the volumetric water content at full saturation state, and was taken to be equal to 0.19, according to the results of the oven dry test reported in Section 4.2.2. The residual water content was considered to be zero; thus the effective saturation, Se, in the model, which is defined as the ratio of difference of saturated water content and residual water content to the saturated water content, had the same value of the saturation reported in the oven dry test. The Van Genuchten parameters, $\alpha=4.33\times10^{-4}$ and n=1.52, were initially assumed to be the same for both drying and wetting phases according to Kumar (2010)'s water retention data through the drying experiments. An inverse modelling analysis was carried out later (see Section 5.4) to determine the best parameters for both wetting and drying phases.

Table 5.3 Material parameters for the concrete matrix

Name	Value	Unit	Description
ρ_w	1000	kg/m^3	Density of water
θ_s	0.19	-	Porosity of the matrix
θ_r	0	m^3/m^3	Residual water content of the matrix
K_s	5×10^{-10}	m/s	Hydraulic conductivity of the matrix
α	4.33×10^{-4}	-	Van Genuchten α parameter
n	1.32/2.0	-	Van Genuchten n parameter
η_w	0.001	Pa·s	Viscosity of water

5.3.4 **Initial value condition and time stepping**

The initial saturation was assigned be the value equal to the measured saturation at time 0 from the TDR test. The 8×8 or 6×8 data matrices reported in the water saturation test by the TDR test (Section 4.3) were linearly interpolated automatically to the node resolution of the model.

Saturation values outside of the data matrix were extrapolated to be a constant value as the boundary of the data matrix.

The time dependent solver was used to solve the model with the backward differences scheme (BDF) method. The time stepping was determined by the solver with a relative tolerance of 1×10^{-3}, and an absolute tolerance of 1×10^{-4}, so that the solver would increase the time stepping to maintain the convergence when it was overcoming the nonlinearity of calculation. For the wetting phase, the time range was from 0 s to 1296000 s (15 days), and the solutions were output in 5000 intervals over the wetting period. For the drying phase, the time range was from 1296000 s to 11664000 s (4 months) and the solutions were output in 1000 intervals over the drying period.

5.4 Hysteresis phenomenon

An inverse modelling analysis was carried out by adjusting K_s, α and n to match the experimental data for water saturation change 3.5 cm away from the midspan at different depths, where the evolution of water saturation were least affected by the variation of the crack line. It was found that there is no single set of Van Genuchten parameters could be identified to satisfactorily simulate the saturation change in both wetting and drying phases. Therefore usage of different hydraulic properties was necessary in order to match the experimentally measured water saturation value distribution in space and time using an inverse modelling analysis. The trial and error was conducted for "α" between 2×10^{-4} and 7×10^{-4}, for "n" between 1.3 and 1.4 for drying, and between 1.8 and 2.5 for wetting. The best values were $\alpha=4.33\times10^{-4}$, n=1.32 for the drying phase and $\alpha=4.33\times10^{-4}$, n=2.0 for the wetting phase.

With $K_s=5\times10^{-10}$ m/s, $\alpha=4.33\times10^{-4}$, n=1.32 for the drying phase and n=2.0 for the wetting phase, experimental data compare nicely with model predictions (Figure 5.4, Figure 5.5). The drying phase figures show that after four months of exposure, water saturation decreased from 1 to 0.7 at a depth of 1.5 cm and from 1 to 0.8 at a depth of 6.5 cm. Within the first month (695 hours), water saturation decreased fast nonlinearly: the water saturation decreased by approximately 1/3 of the total water saturation change in the fourth months at a depth of 1.5 cm, and approximately

1/2 at a depth of 6.5 cm. After the first one month of drying, desaturation became steady and slow.

The wetting phase figures indicate a fast saturation process. It only took about 50 hours for the near-surface part (depth=1.5 cm) to reach full saturation and in another 200 hours, the full saturation state reaches a depth of 6.5 cm. During the fast-paced water movement, a significant difference between model predictions and experimental results can be observed at early age (0-25 hours), where the model gives a flat part with unchanged saturation while the experimental data shows rapid change within 3 hours. This can be explained by the mechanism of the TDR test. As stated in Section 4.3, the TDR gives an averaged water content value in its sampled volume. Therefore the water content at a given point (coordinates) as reported by TDR may be affected, even before the water penetration front in the sampled volume has reached that particular point.

With the Van Genuchten parameters determined as $K_s=5\times10^{-10}$ m/s, $\alpha=4.33\times10^{-4}$, n=1.32 for the drying phase and n=2.0 for the wetting phase, the retention curve and the relative permeability curve for wetting and drying can be plotted according to the constitutive relationship of hydraulic properties (Equation 5.2-5.4). Figure 5.6 shows the water retention curve. Figure 5.7 and Figure 5.8 show the relationship relative permeability vs. pressure head and saturation. These curves are completely different: the water retention curve shows a difference of 0.4 in saturation between wetting and drying when pressure head increases to -12000 m. The relative permeability curves also indicate the difference of hydraulic conductivity of sample deviate up to 0.5 in the process of wetting and drying, knowing the hydraulic conductivity at a certain saturation level is a product of the relative permeability times the hydraulic conductivity at full saturation. These strong differences are clear indications that both curves are controlled by a hysteretic behaviour when concrete is subjected to wetting/drying cycles.

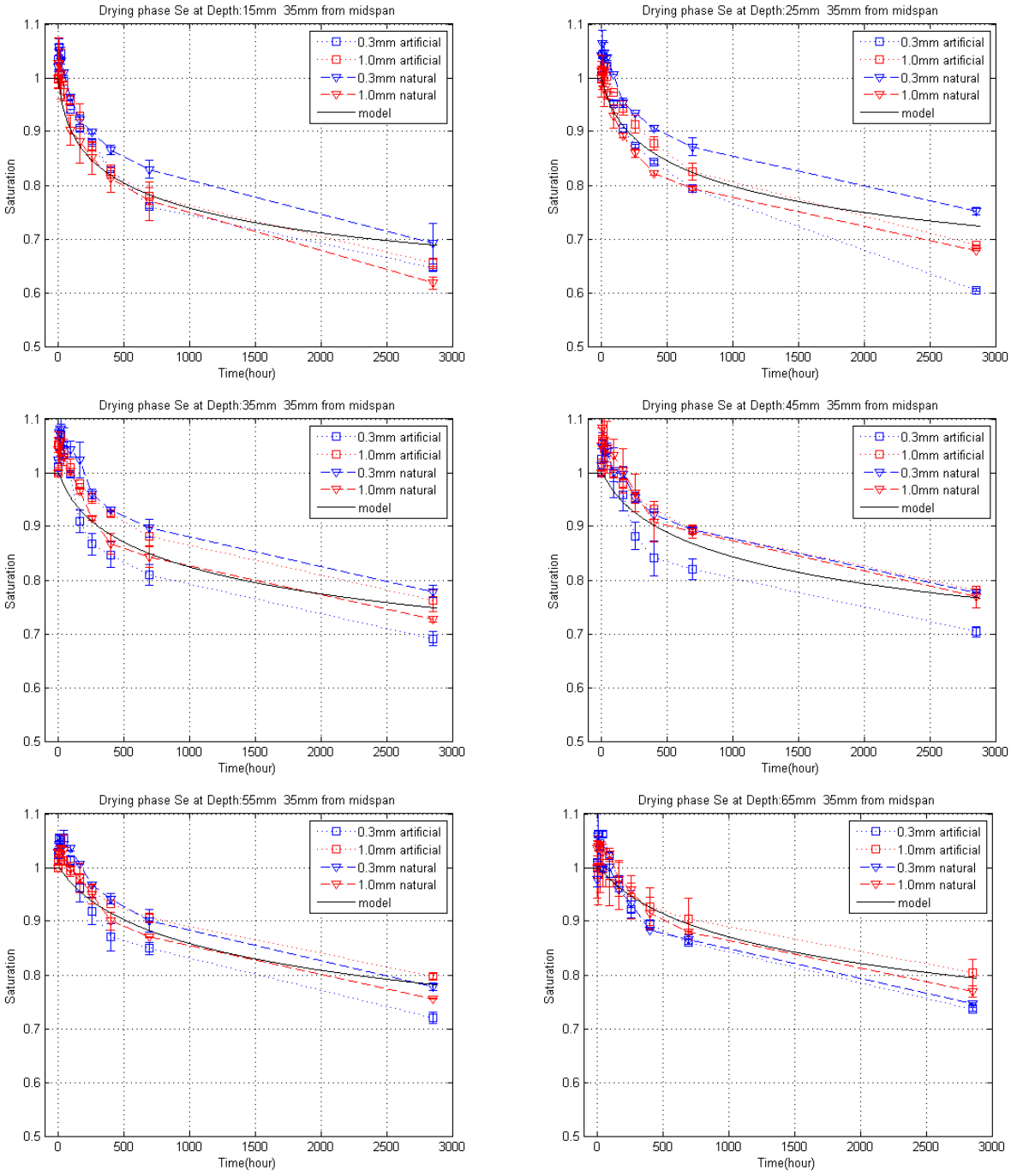

Figure 5.4 Evolution of water saturation at different depths during drying phase: experimental data and model predictions.

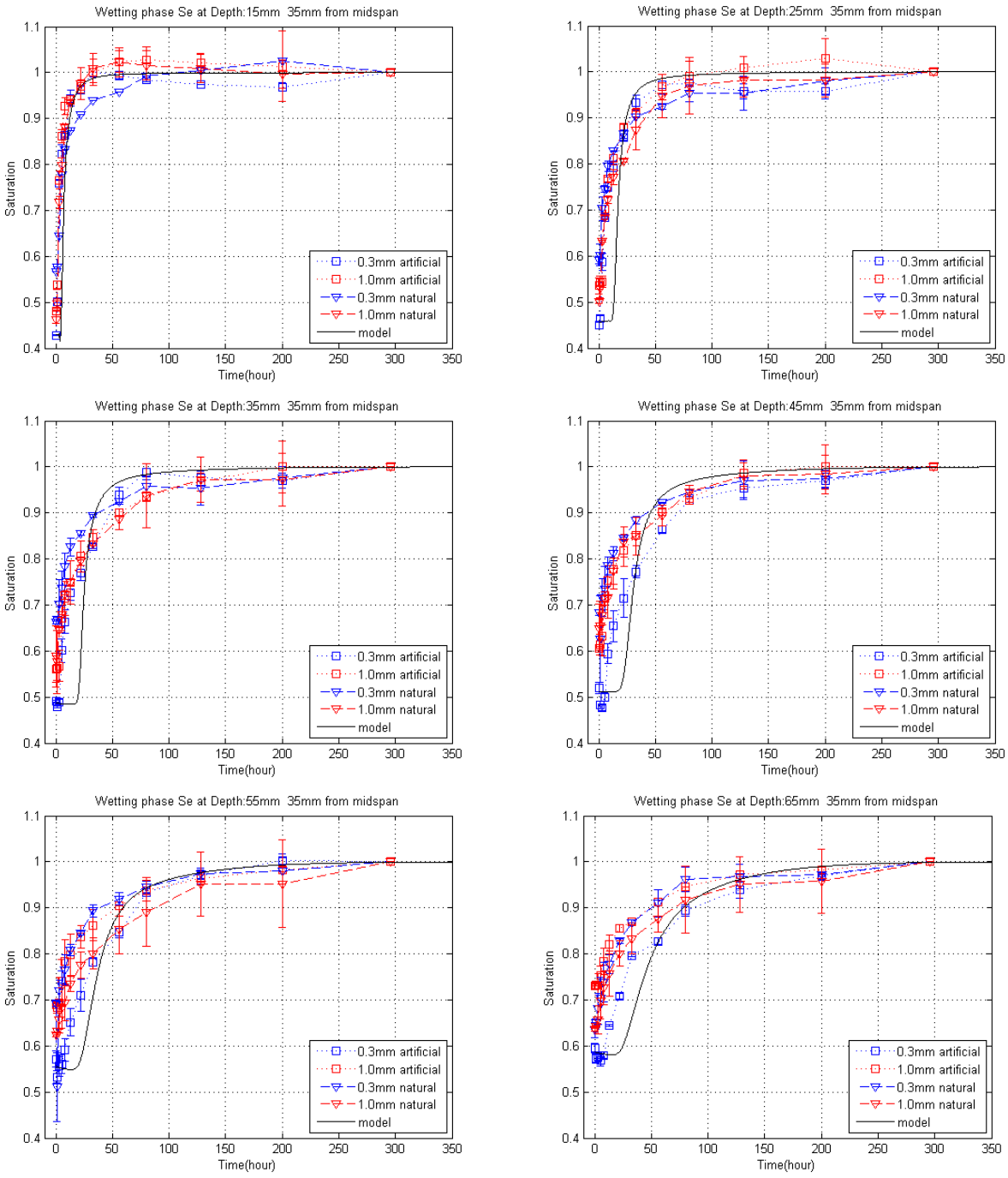

Figure 5.5 Evolution of water saturation at different depths during the wetting phase: experimental data and model predictions.

This hysteresis could be explained from a microstructural standpoint according to Hall (2009): besides of overall saturation state, the unsaturated hydraulic conductivity is also determined by the distribution of water in pore structure. In drying phase, water tends to be retained in narrow-necked large pores while in wetting phase, the retained water would be re-distributed through finer pore network which renders a larger overall conductivity. Therefore as seen in Figure 5.8, at any saturation degree, the wetting relative permeability (or hydraulic conductivity, hydraulic conductivity= relative permeability×saturation hydraulic conductivity) is higher than the drying one.

It is worth mentioning that the current implementation of hysteresis is limited in the sense that it uses a single curve for drying and another single curve for wetting. This worked effectively for the simple wetting/drying scenario considered in this study. However, a more general wetting/ drying boundary condition would require a more general hysteresis model to account for the fact that various points at different locations in the concrete sample would experience a different drying or wetting history and hence would need different curves. Nonetheless, despite the relative simplicity, the current model is still able to capture the existence of hysteresis for wetting/ drying boundary conditions.

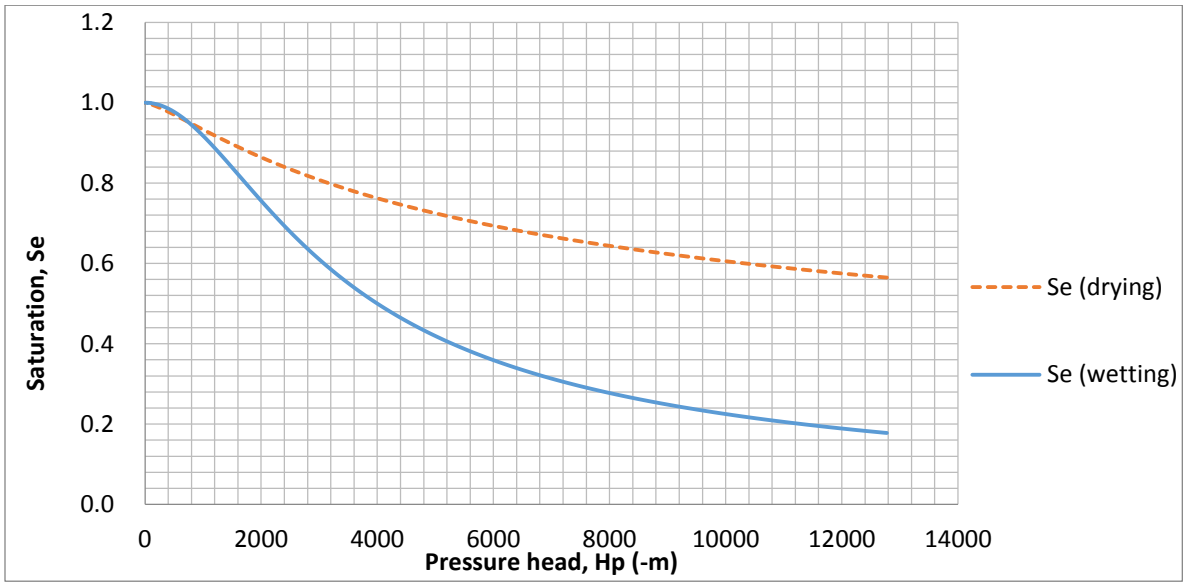

Figure 5.6 Water retention curve.

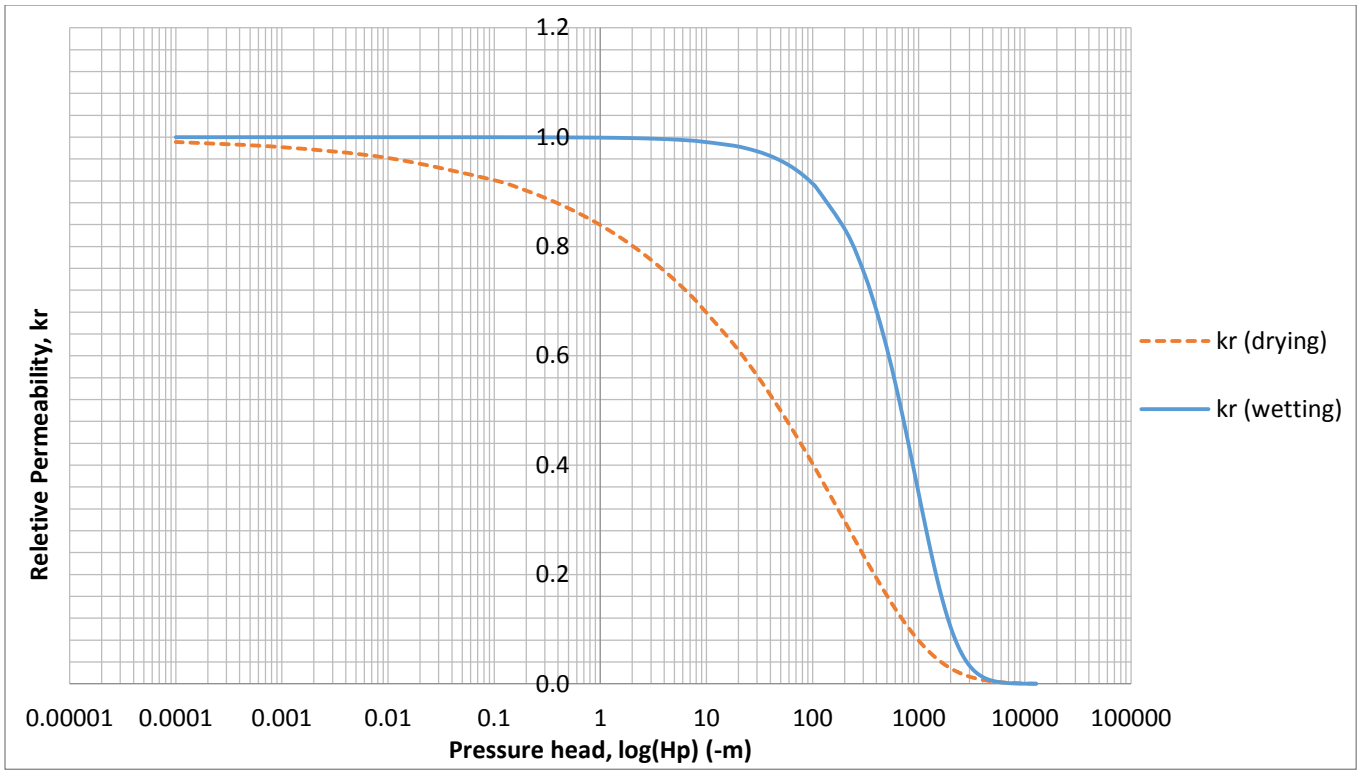

Figure 5.7 Reletive permeability vs. pressure head.

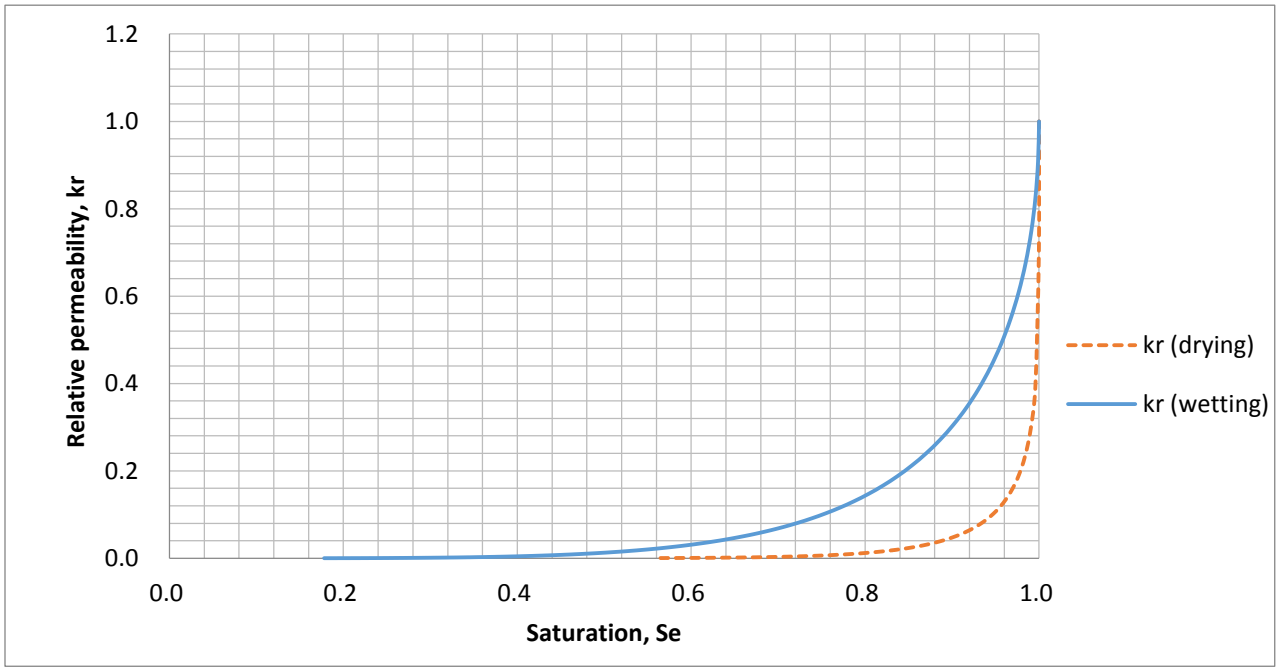

Figure 5.8 Relative permeability vs. saturation.

5.5 1D natural crack representation

Natural cracks introduced by three-point flexural loading essentially have a 3D morphology. In this 2D simulation model, they are represented based on the 1D crack lines. For each crack, three models (Front, Back and Average) were set up using front, back and averaged crack lines. Saturation distribution plots for natural cracks with surface openings of 0.3 mm, N03, and 1.0 mm, N10, at 695 hours and 2855 hours are shown in Figure 5.9 for all three crack-representations used (Front, Back and Average). These three representations are compared by the difference between the results from the averaged crack line model and the numerically averaged value of front and back crack line models as illustrated in Figure 5.10.

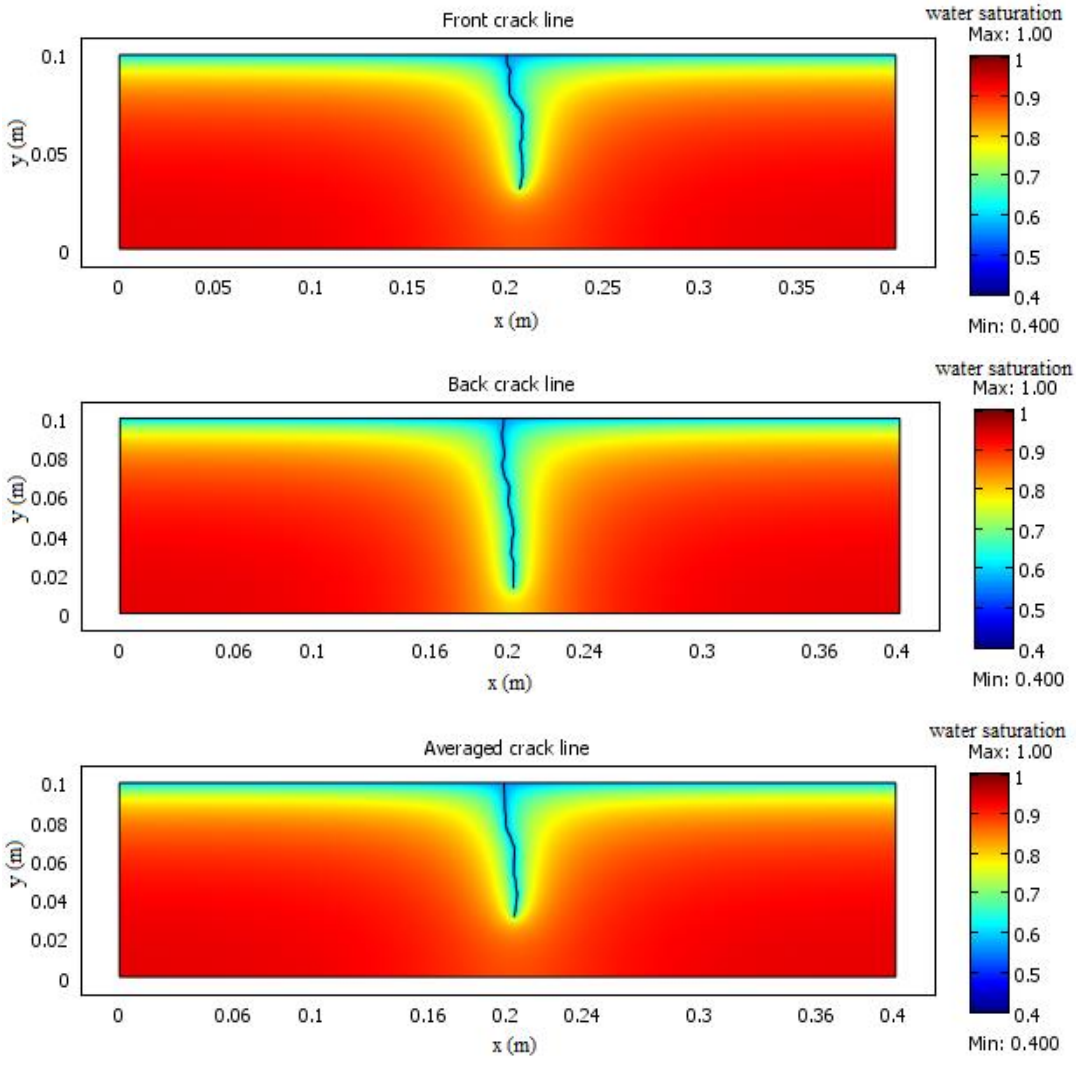

(a) Water saturation plot: N03 saturation at 695 hours of exposure to drying.

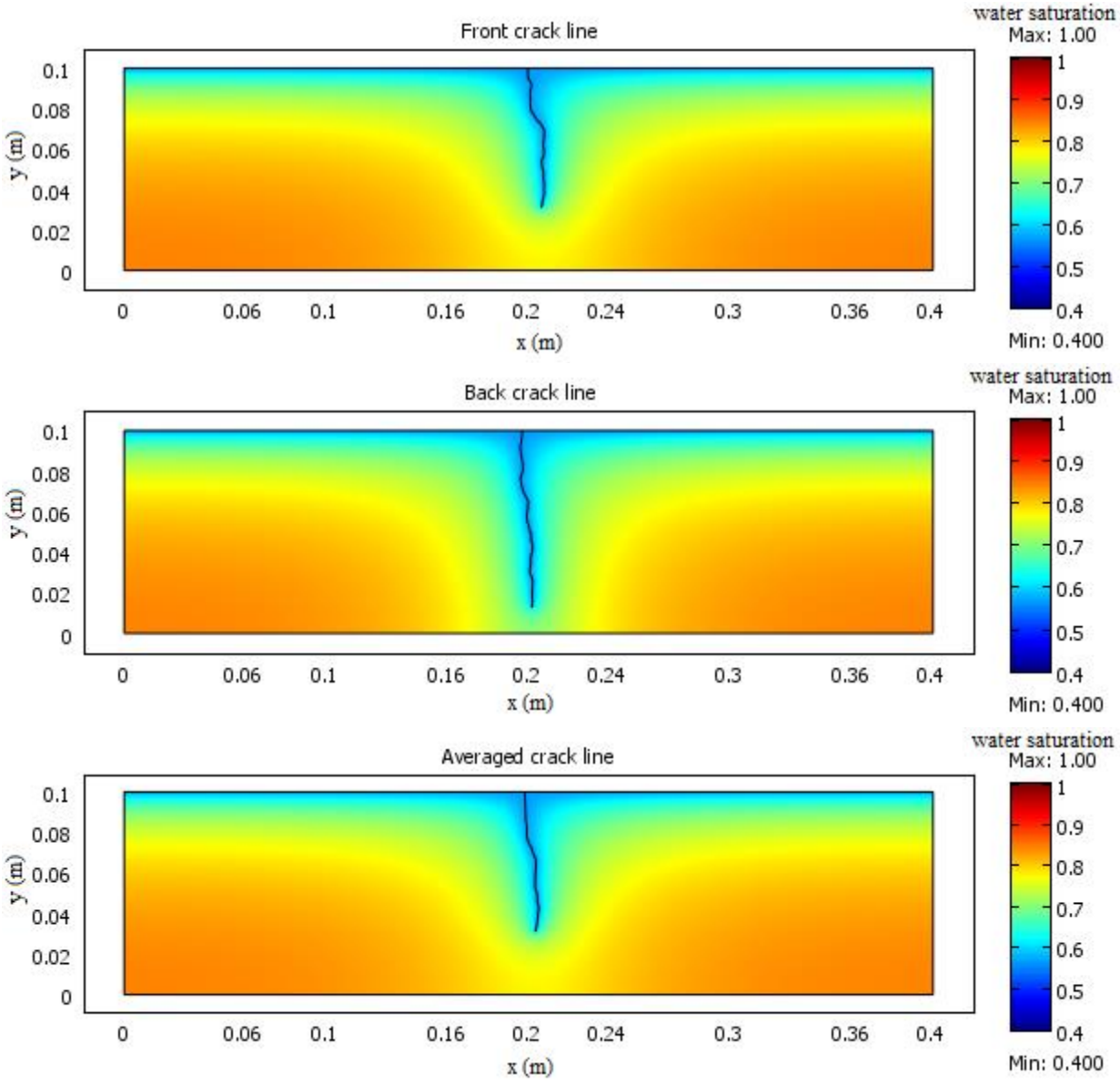

(b) Water saturation plot: N03 saturation after 2855 hours of exposure to drying.

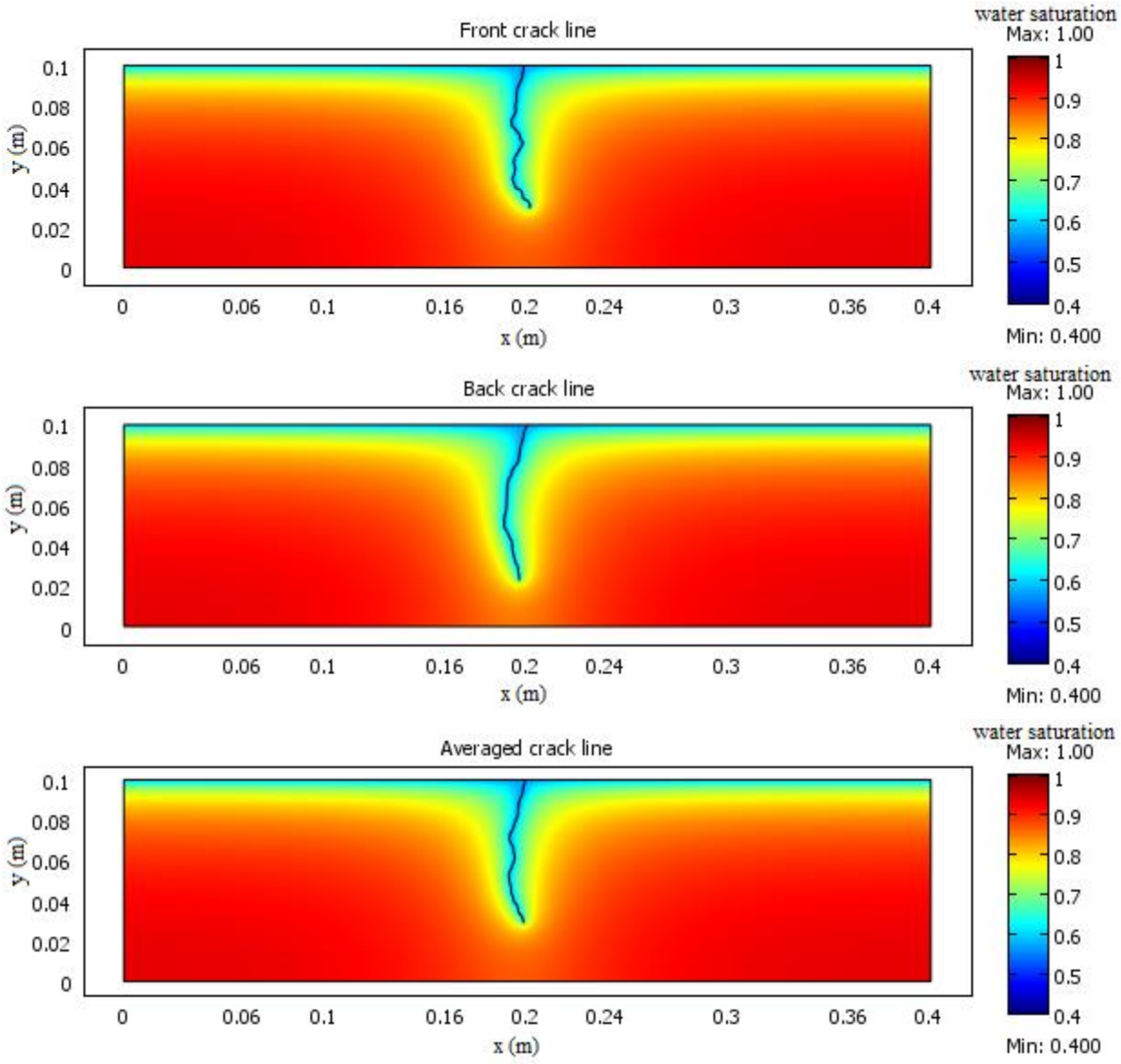

(c) Water saturation plot: N10 saturation after 695 hours of exposure to drying.

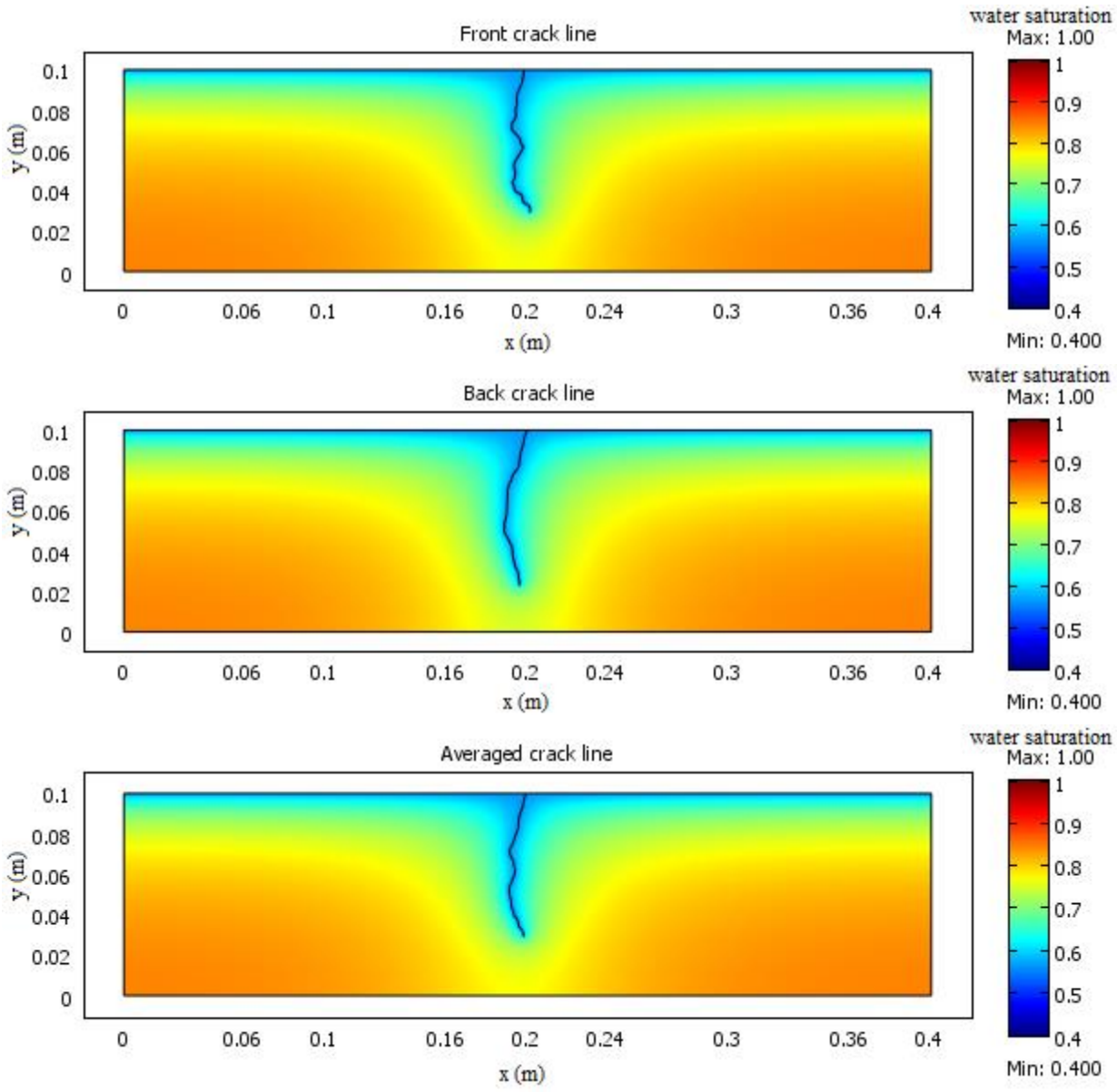

(d) Water saturation plot: N10 saturation after 2855 hours of exposure to drying.

Figure 5.9 Water saturation surface plots of N03 and N10 for all three crack representations (front back and averaged) at 695 hours and 2855 hours. N03: concrete specimen has a surface crack width equal to 0.3 mm; N10: concrete specimen has a surface crack width equal to 1.0 mm).

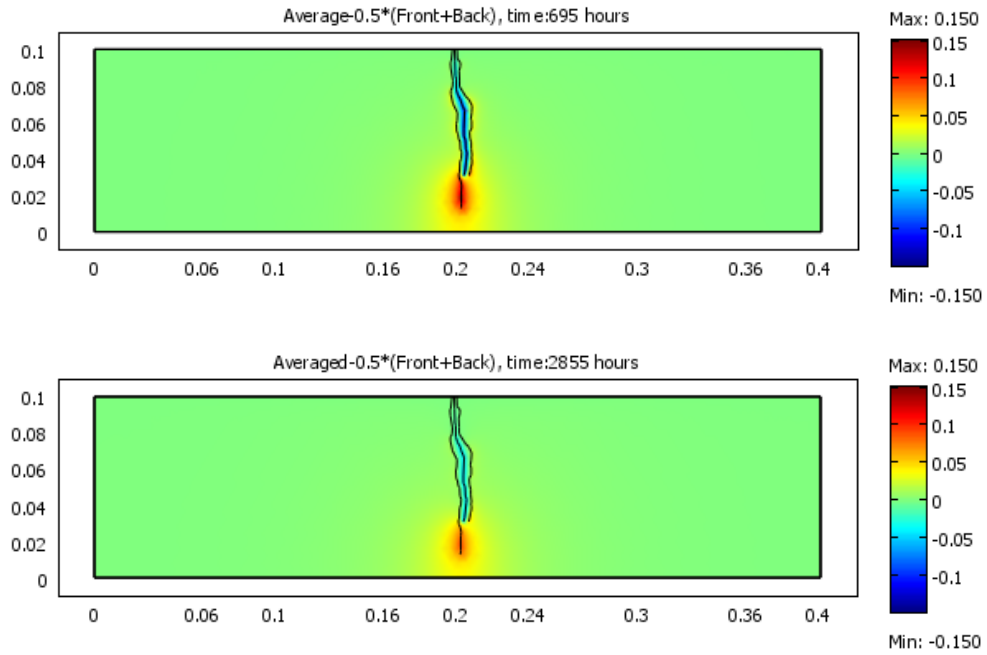

(a) N03, plotting of value of [Averaged-0.5×(Front+Back)] at 2855 hours

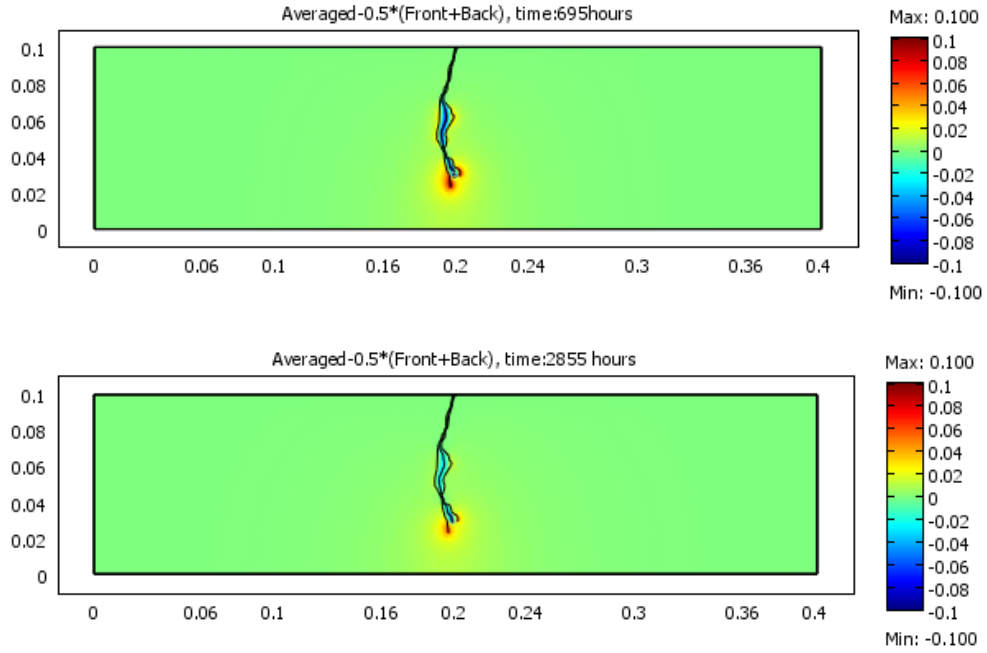

(b) N10, plotting of value of [Averaged-0.5× (Front+Back)] at 2855 hours

Figure 5.10 Difference between averaged crack model and averaged value of front and back crack models. (N03: concrete specimen has a surface crack width equal to 0.3 mm; N10: concrete specimen has a surface crack width equal to 1.0 mm; "Averaged", "Front" and "Back" represents the water saturation results from the Averaged, Font and Back crack line models).

The substantial differences between the averaged crack model and the averaged value of the front and back crack models [i.e. Averaged vs. 0.5× (Front+Back)] are generally confined within the area between the front and back crack line; while outside of that region, errors brought by using averaged crack line instead of using the averaged results from the front and back crack line models diminish to zero. The maximum error of [Averaged vs. 0.5× (Front+Back)] during the process of drying are listed In Table 5.4. From 695 hour to 2855 hour the saturation errors became smaller (from -0.146 to -0.078, from 0.137 to 0.094, from-0.157 to -0.082, from 0.104 to 0.068). The most positive deviation can be found at the tip of the front/back crack line, which is caused by the difference in the lengths of the crack. The most negative deviation is focused on the averaged crack line. For a certain point within the cracking area the error is due to the different distances away from the exposure surfaces (different crack lines) in each type of model.

This difference (or error) is plotted along the line, y = 0.05 m (at mid height of the cracked specimen) (Figure 5.11). These plots show that the difference between the various crack representations becomes less significant with time. The larger differences are within 0.01m from the averaged crack line; outside of that region, the saturation difference dramatically decreased down to less than 0.02. For the wetting phase, a similar trend is also observed, as can be seen in Figure 5.12.

Table 5.4 Maximum errors brought by crack line choice in the natural crack sample at 695 and 2855 hours

Time (hour)	max/min value of [Averaged-0.5× (Front+Back)]			
	N03		N10	
695	-0.146	+0.137	-0.157	+0.104
2855	-0.078	+0.094	-0.082	+0.068

"Averaged", "Front" and "Back" represents the water saturation results from the Averaged, Font and Back crack line models.

It can be suggested that, for the simple flexural crack, the 1D averaged crack line is capable of representing the crack in the wetting and drying scenarios. The introduced error diminishes with time and with the distance away from the crack.

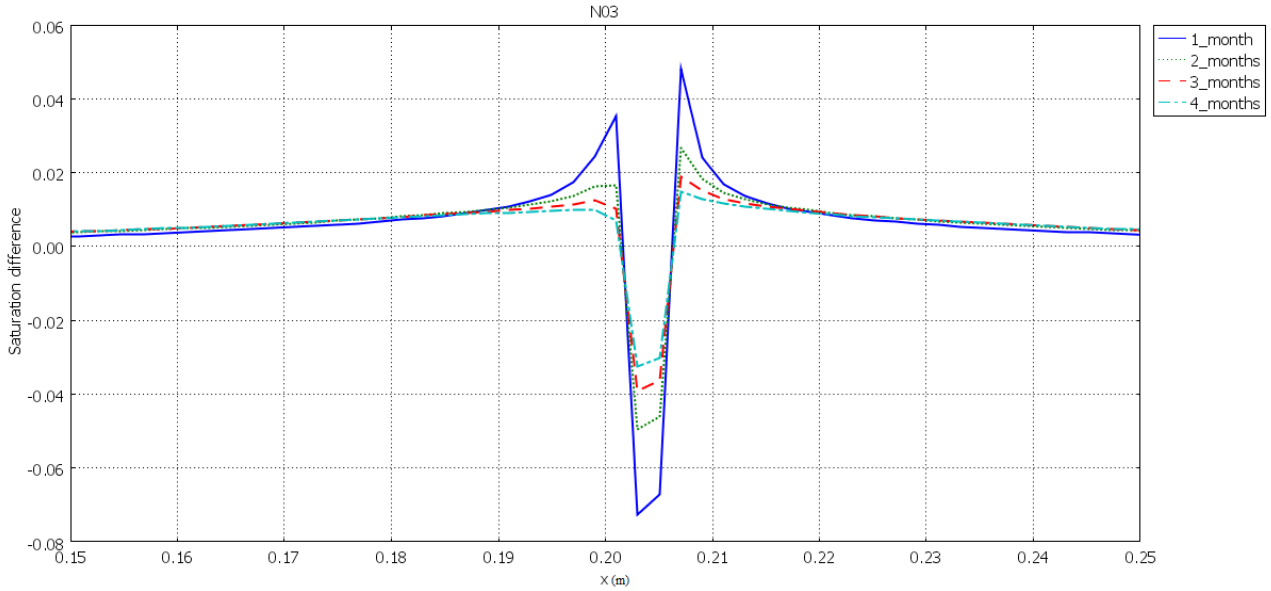

(a)

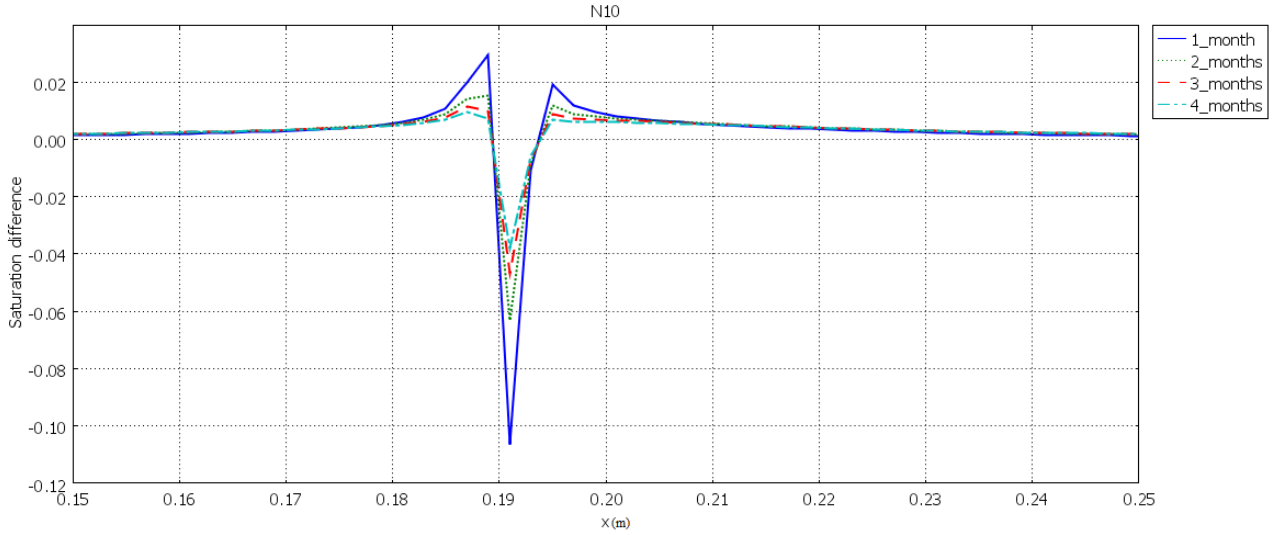

(b)

Figure 5.11 Water saturation difference [Averaged-0.5×(Front+Back)] change with time at mid-height of the specimen (y = 0.05 m), in the drying phase (a) for the 0.3 mm crack specimen (b) for the 1.0 mm crack specimen.

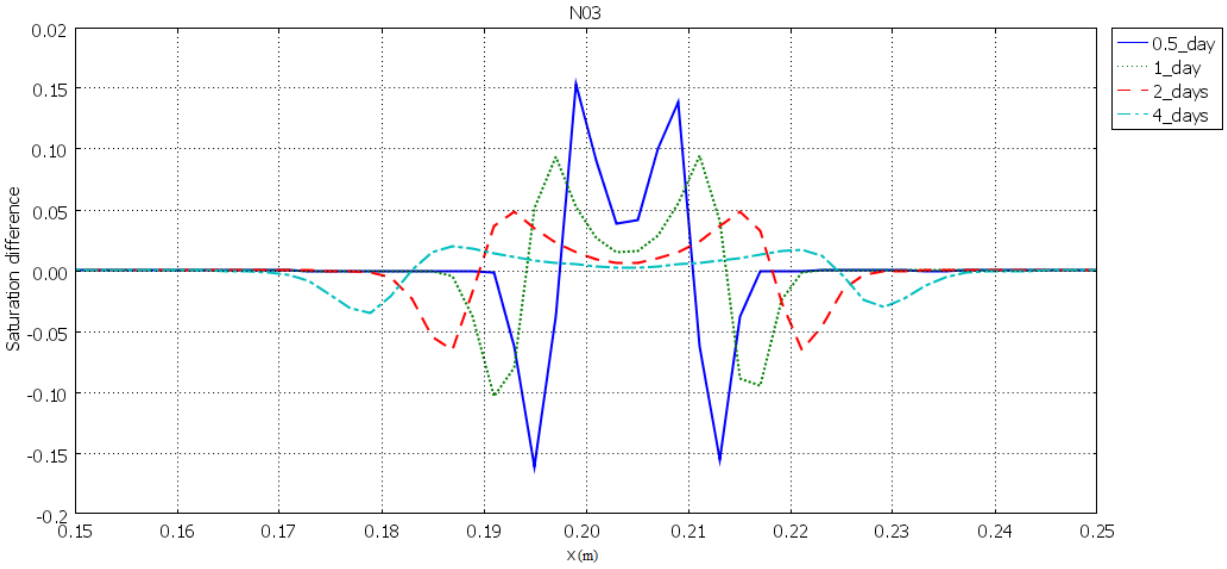

(a)

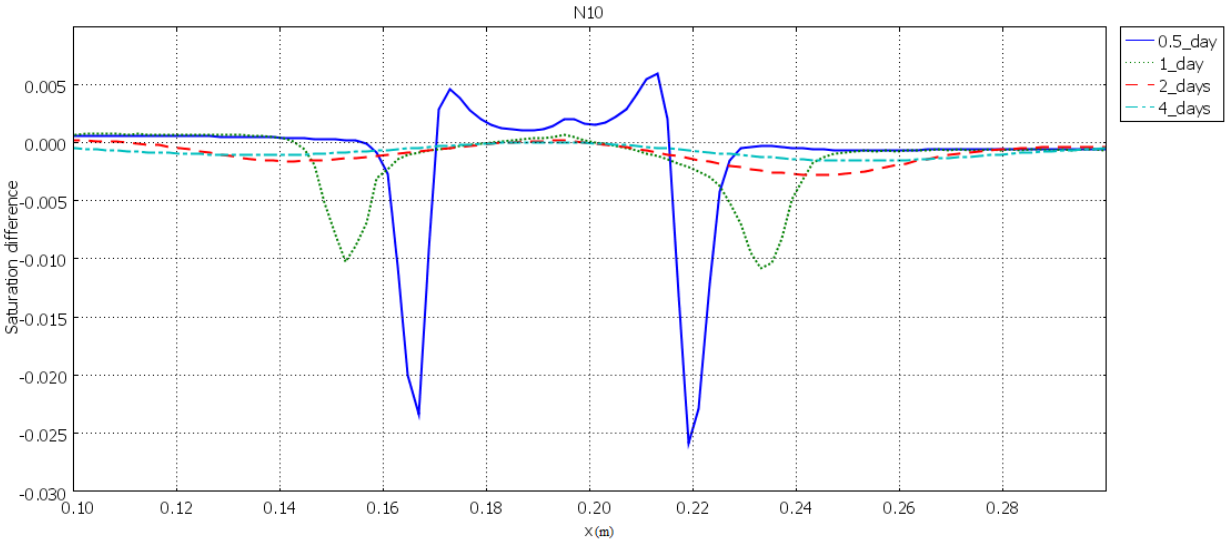

(b)

Figure 5.12 Water saturation difference [Averaged-0.5×(Front+Back)] change with time at mid-height of the specimen (y = 0.05 m), in the wetting phase (a) for the 0.3 mm crack specimen (b) for the 1.0 mm crack specimen.

5.6 Free surface model vs. equivalent porous medium model

The 1D crack model discussed above treated the crack as an external surface boundary. This approach was used based on the conclusion that the crack surface behaved like the free surface (see Section 4.4). However, the infiltration test has shown that the crack size does have an effect on the hydraulic conductivity in the cracking area. Therefore, it would be interesting to investigate how much error would be induced by modelling a crack as an external surface (free surface) exposed to wetting/ drying cycles as opposed to modelling it as an equivalent porous medium. To this end, a second FE model was built where the crack was represented as an equivalent porous medium according to the theory presented in Section 5.2. As shown in Figure 5.13, the line mark by "x" is the representation of the crack, which has a 1D geometry and at the same time has hydraulic properties of a porous medium. The hydraulic conductivity of the crack at a certain saturation level is defined by the product of the saturated hydraulic conductivity, *K*, and the relative permeability, K_r^{cr}. The saturated hydraulic conductivity, *K* was calculated according to Equation 5.6. The relative permeability, K_r^{cr} was expressed as a function of pressure head, Hp, shown in Equation 5.9, where the most probable value of crack width, w_0 was the crack opening size (0.3 mm and 1.0 mm). Based on the previous work (Boulfiza et al. 2003) where this parameter was determined according to an image analysis of a natural crack, the standard deviation, σ of the logarithm crack width distribution was assumed to be 0.43. The logarithm distributions of the cracks are plotted in Figure 5.13.

In order to compare the free surface model and equivalent porous medium model, the "straight crack line" (artificial crack model) geometry was used to represent both crack models. The difference between the free surface model and equivalent porous medium model is expressed by subtracting the results of the free surface model (0.3 mm crack and 1.0 mm crack) from the results of equivalent porous medium models.

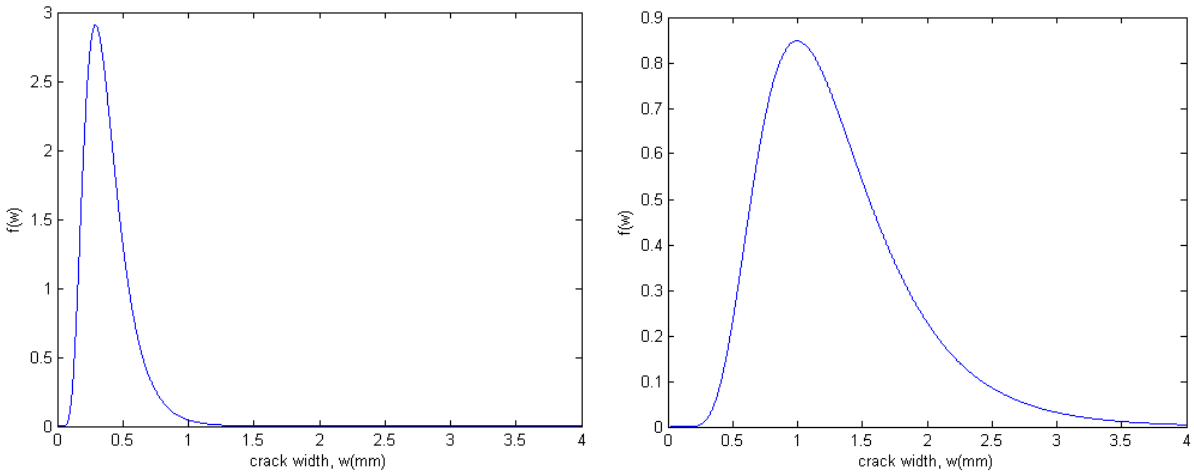

Figure 5.13 Logarithm distribution of the crack width (a) most probable crack width: 0.3 mm (b) most probable crack width: 1.0 mm.

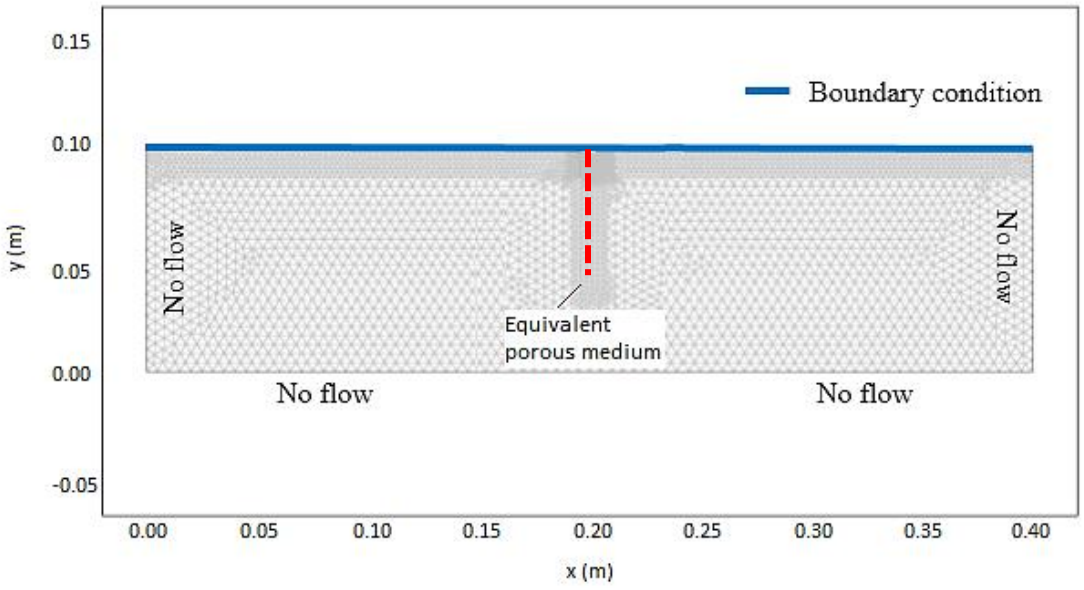

Figure 5.14 Equivalent porous medium model.

For the drying phase, as shown in Figure 5.15, the largest difference between the two model simulations were mainly located near the crack. The difference between the predictions of the equivalent porous medium model and the predictions of the free surface model was small for both crack openings considered in this study (0.3 mm and 1.0 mm). For the simulation results, after 1 month and 4 months of exposure, the positive difference and negative difference value (saturation) have a magnitude of 10^{-4} to 10^{-5} in saturation. This difference can be neglected as in the drying phase the saturation level ranged between 0.4-1.0.

For the wetting phase, both the "free surface" crack model and the "equivalent porous medium" crack models (0.3 mm and 1.0 mm) had a similar behaviour. The differences in saturation level over time between the two models are plotted in Figure 5.16. The major differences were located at the water front line both near and far from the crack. The positive difference and negative difference (in saturation) had a magnitude between 10^{-2} to10^{-3} in day one; after two days in wetting phase, the differences were further reduced to a magnitude between 10^{-3} to10^{-4}. This differences were probably caused by the model error, because even same meshing was applied to both types of models and the differences could still be observed away from the crack.

In conclusion, the crack could be modelled either as a "free surface" or as an "equivalent porous medium" in the wetting and drying scenarios without introducing any large errors. The variations brought by applying the two different approaches are limited within 0.01 saturation level.

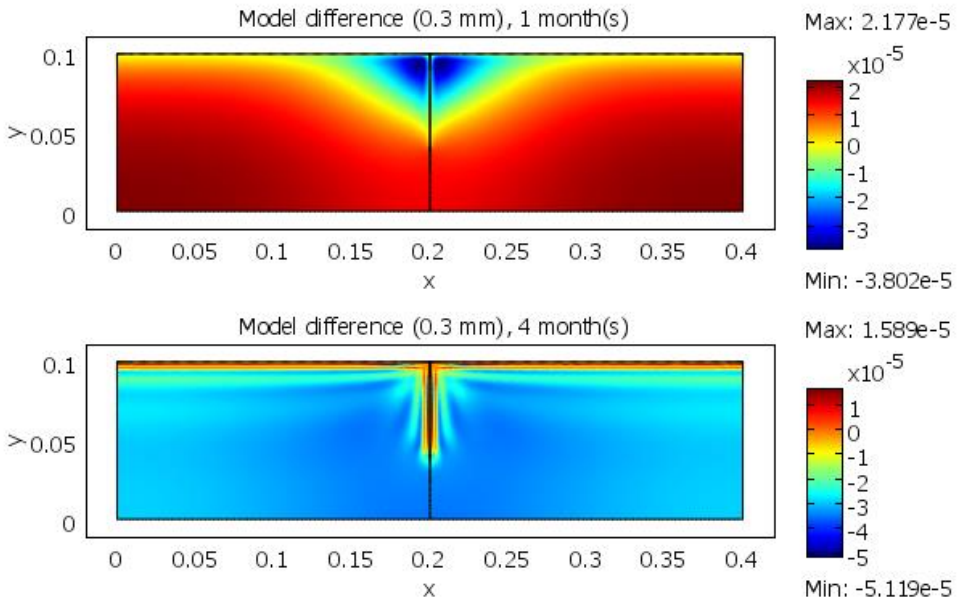

(a)

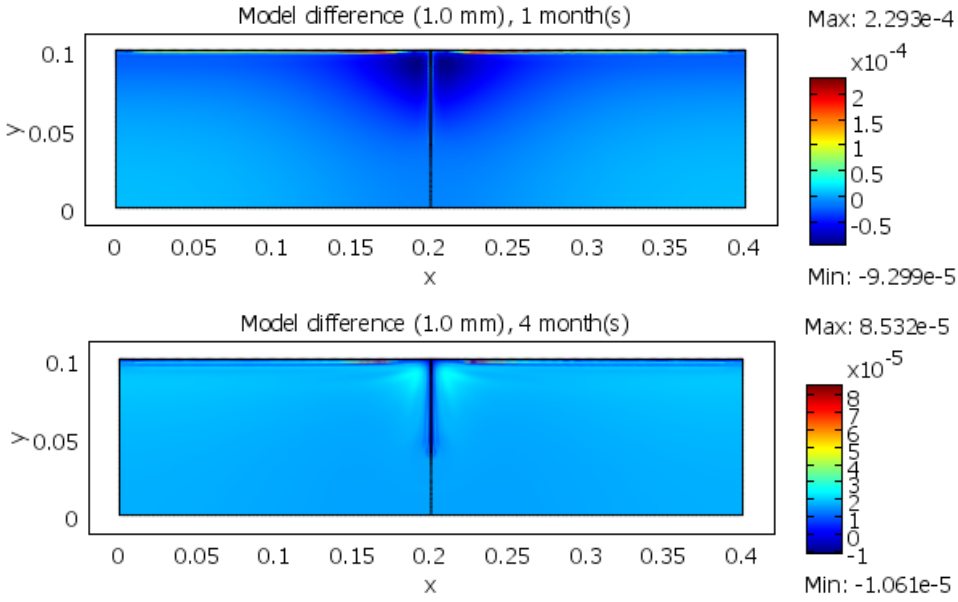

(b)

*x,y coordinate unit: meter
**crack line: x: 0.2, y: [0.06, 0.1]

Figure 5.15 Difference in water saturation level predictions between the "equivalent porous medium" models and the "free surface" crack model in the drying phase: (a) equivalent porous medium for natural crack with 0.3 mm opening; (b) equivalent porous medium for natural crack with 1.0 mm opening.

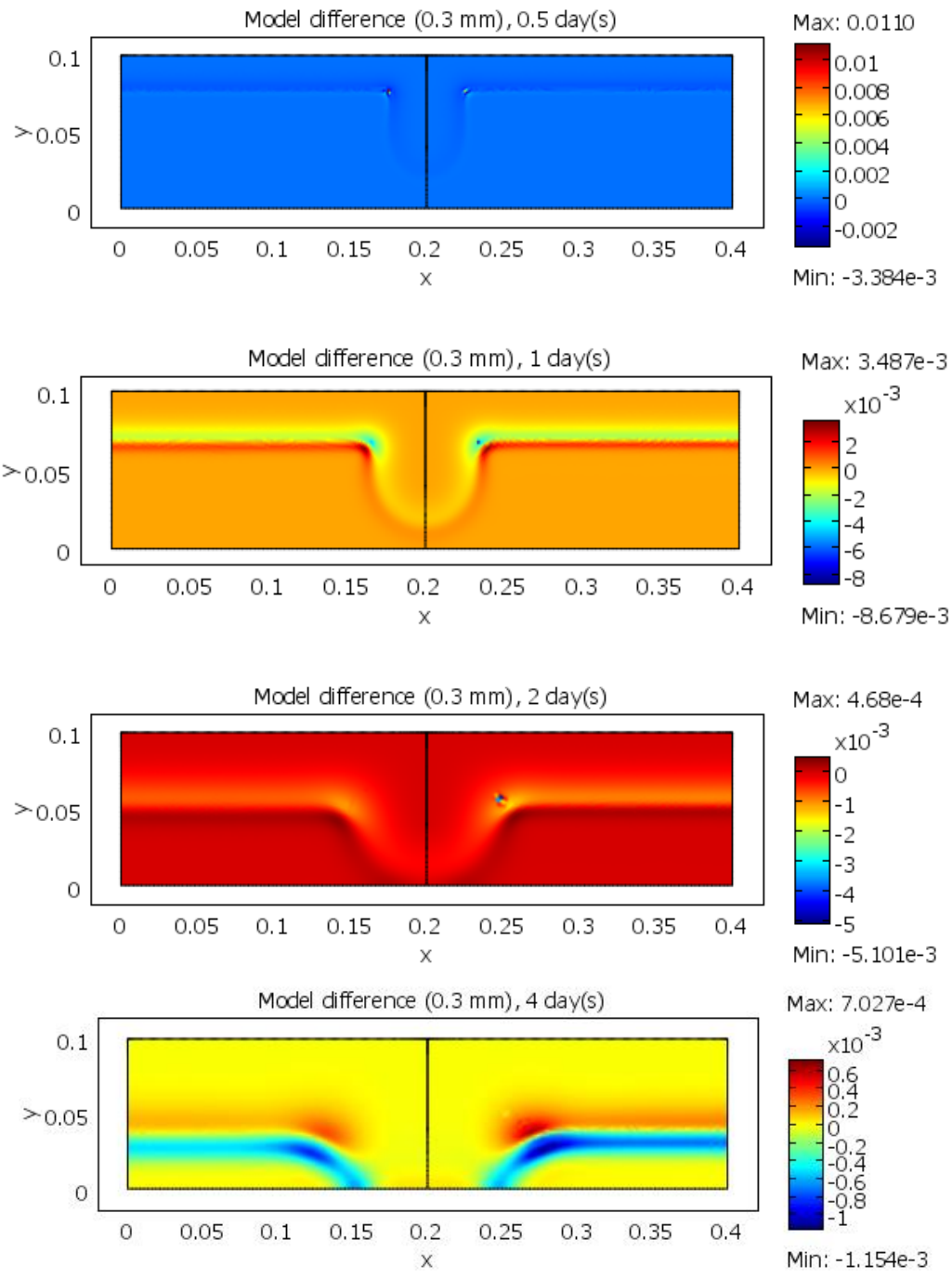

(a)

*x,y coordinate unit: meter

**crack line: x: 0.2, y: [0.06, 0.1]

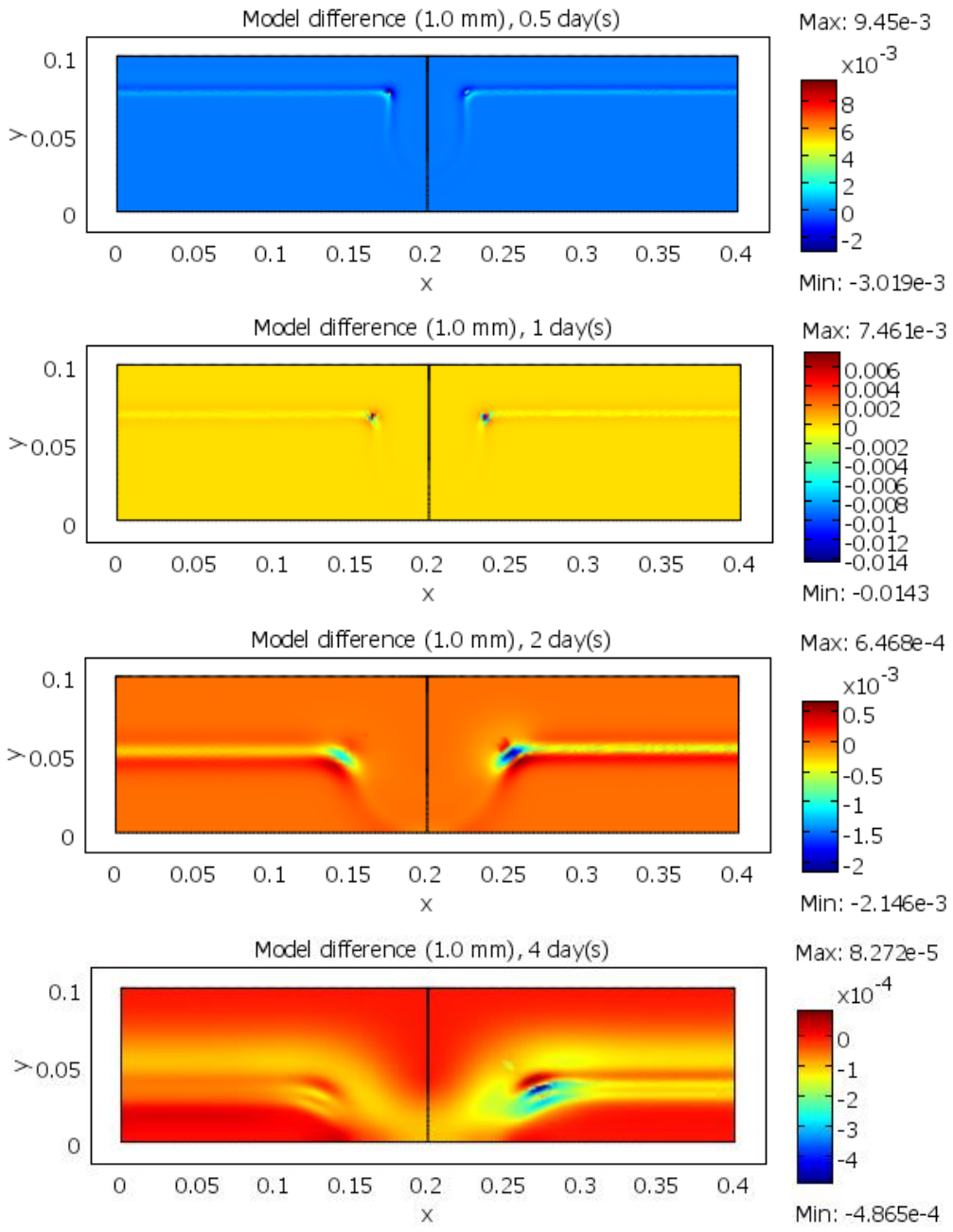

(b)

*x,y coordinate unit: meter

**crack line: x: 0.2, y: [0.06, 0.1]

Figure 5.16 Difference in water saturation predictions between the "equivalent porous medium" crack models and "free surface" crack model in wetting phase: (a) equivalent porous medium for natural crack with 0.3 mm opening; (b) equivalent porous medium for natural crack with 1.0 mm opening.

6 Conclusions and recommendations

This chapter provides a summary of the work and conclusions based on the findings in this research. Recommendations are also provided for future research on this subject.

6.1 Summary of work

Two types of cracks (an artificial crack and a natural crack) and two crack opening levels were generated with flexural loading and the shim-pullout technique in concrete beams. An infiltration test was performed on the cracked beams, and the apparent hydraulic conductivity of the cracked concrete was measured for the natural cracks and the artificial cracks with cracks openings of 0.3 mm and 1.0 mm.

A time domain reflectometry (TDR) technique was employed and customized for the measurement of water content and chloride ion concentration around the concrete cracking region during the wetting and drying scenarios. The dielectric constant was calibrated to the water content, but the electrical conductivity could not be calibrated to measure the chloride ion content in concrete, because the high ionic strength of the concrete pore solution due to the presence of various ionic species in relatively high concentrations reduce the sensitivity to the Ec change brought by chloride ions.

A finite element model was developed to simulate the water flow in variably saturated cracked concrete under wetting and drying conditions. The Van Genuchten parameters were evaluated based on the experimental results. A strong hysteresis phenomenon was observed and a relatively simple model was proposed to represent it. Two model approaches, “free surface” and “equivalent porous medium”, were used to represent the cracks, and the results from both models were compared.

6.2 Conclusions

1. The presence of cracks (0.3 mm and 1.0 mm) dramatically increased the value of the hydraulic conductivity of concrete (by up to 5 orders of magnitude). Both larger crack sizes and smoother texture would increase the hydraulic conductivity of concrete. The

effect of crack roughness is significant on concrete with small size cracks. However for concrete with large cracks, this effect does not have a significant impact on the hydraulic conductivity.

2. A Time Domain Reflectometry (TDR) test was developed for monitoring the evolution of water saturation around the crack over time. A linear regression model was used to relate the volumetric water content and dielectric constant in concrete.

3. The evolution of water saturation of the cracked concrete under wetting and drying conditions was analyzed as colour-scaled images and the water saturation contours were compared for different crack openings. For the artificial crack samples, a deviation from the expected "perfectly symmetric" flow regime around a straight crack was observed. This was probably caused by the micro cracks induced during the shim pull-out process or a non-uniform compaction around the shim insertion. For the natural cracks, in the drying phase, smaller cracks seemed to have better water storage. Hence, the water saturation decreased at a slightly slower rate as compared to larger natural cracks.

4. The electrical conductivity (Ec) measured by TDR was insensitive to the chloride concentration in the pore solution. This may have been caused by the high ionic strength in the concrete pore solution, which may act as background noise that overshadows the Ec change brought about by the chloride ions.

5. The crack surface of both crack types (artificial and natural) and sizes (0.3 mm and 1.0 mm) had a similar influence as the open surface on the water transport The crack could be modelled as an open free surface without inducing a very large error in water saturation levels.

6. A strong hysteresis phenomenon was found during the inverse modelling process of the Van Genuchten parameters. It was not proper to model both the wetting and drying flow regimes using a single retention curve and a single relative permeability curve. The optimal values of the inverse analysis were: $K_s=5\times10^{-10}$ m/s, $\alpha=4.33\times10^{-4}$ for both phases; n=1.32 for the wetting phase and n=2.0 for the drying phase

7. For the flexural cracks, the 1D crack line averaged from the front and back crack lines was capable of representing the crack in the wetting and drying scenarios. The introduced error diminished with time and with the distance from the crack. It was also noticed that the errors induced when using the back of the crack, its front, or an average of both to represent the crack in a 2D model, were so small that it did not really matter with one was used.

8. The crack could be modelled as a "free surface" or an "equivalent porous medium" in the wetting and drying scenarios. The variations brought by applying the two different approaches were limited to within 0.01 saturation level.

6.3 Recommendations for future work

1. The TDR technique gave very good results in the lab, and hence should be tried with larger scale field structures.

2. A more general hysteresis model, with more than a fixed curve for wetting and another fixed curve for drying, is needed to accommodate more general wetting/ drying cycles in a more accurate way.

3. The numerical model should be extended to include the transport of chloride ions by advection and diffusion in cracked concrete.

4. It is suggested that oxygen, as one of the main corrosion inducing factors, be studied in the cracked concrete structure.

5. The experimental program should be extended by including a direct measurement of corrosion rates in cracked concrete.

References

Aldea, C., Shah, S. P., & Karr, A. (1999). Effect of cracking on water and chloride permeability of concrete. *Journal of Materials in Civil Engineering, 11*(3), 181-187.

Alekseev, S.N., Ivanov, F.M., Modry, S., Schiessl, P. (1993). Durability of reinforced concrete in aggressive media. (ed. M. Majithia & S.K. Mallick), Russian Translation Series 96, A.A. Balkema/Rotterdam/Brookfield, p. 164-247,305-349.

Aligizaki, K. K. (1999). *Modeling of concrete cracking due to corrosion of embedded reinforcement.* (Order No. 9937915, The Pennsylvania State University). ProQuest Dissertations and Theses, 166-166 p. Retrieved from http://search.proquest.com/docview/304537502?accountid=14739. (304537502).

Angst, U., Elsener, B., Larsen, C. K., & Vennesland, Ø. (2009). Critical chloride content in reinforced concrete—a review. *Cement and Concrete Research, 39*(12), 1122-1138.

Arya, C., & Vassie, P. R. W. (1995). Influence of cathode-to-anode area ratio and separation distance on galvanic corrosion currents of steel in concrete containing chlorides. *Cement and Concrete Research*, 25(5), 989-998.

Arya, C., & Ofori-Darko, F. (1996). Influence of crack frequency on reinforcement corrosion in concrete. *Cement and Concrete Research, 26*(3), 345-353.

Baker, J. M., & Spaans, E. J. (1993). Comments on "time domain reflectometry measurements of water content and electrical conductivity of layered soil columns". *Soil Science Society of America Journal*, 57(5), 1395-1396.

Bakhshi, M. (2011). *Characterization and Modeling of Moisture Flow through hydrating Cement-Based Materials under Early-Age Drying and Shrinkage Conditions*. Arizona State University.

Bear, J., & Cheng, A. H. D. (2010). *Modeling groundwater flow and contaminant transport*. Dordrecht, Heidelberg, London, New York: Springer.

Bi, M. (2008). *Corrosion of reinforcing steel in cracked concrete.* (Order No. 3325472, City University of New York). ProQuest Dissertations and Theses, 197. Retrieved from http://search.proquest.com/docview/304670978?accountid=14739. (304670978).

Boulfiza, M., Sakai, K., Banthia, N., & Yoshida, H. (2003). Prediction of chloride ions ingress in uncracked and cracked concrete. *ACI materials Journal*, 100(1).

Broomfield, J. P. (2007). *Corrosion of steel in concrete: understanding, investigation and repair*. Taylor & Francis.

Brooks, R. H. (1966). Properties of porous media affecting fluid flow. *In Journal of the Irrigation and Drainage Division, Proceedings of the American Society of Civil Engineers* (Vol. 92, pp. 61-88).

Bruce, R. R., & Klute, A. (1956). The measurement of soil moisture diffusivity. *Soil Science Society of America Journal*, 20(4), 458-462.

Cemica, J. N. (1995). *Geotechnical engineering: Foundation design*. Wiley.

Curtis, H., & Defandorf, F. (1929). Dielectric constant and dielectric strength of elementary substances, pure inorganic compounds, and air. Washburn (Ed.) *International Critical Tables of Numerical Data. Physics, Chemistry, and Technology*, 6, 73-107.

Dalton, F., Herkelrath, W., Rawlins, D., & Rhoades, J. (1984). Time-domain reflectometry: Simultaneous measurement of soil water content and electrical conductivity with a single probe. *Science*, 224(4652), 989-990.

Decagon Device. (2003). Mini disk infiltrometer user's manual. Retrieved from http://www.decagon.com/education/minidisk-infiltrometer-manual.

Drchalová, J., & Černý, R. (1998). Non-steady-state methods for determining the moisture diffusivity of porous materials. *International communications in heat and mass transfer*, 25(1), 109-116.

Ervin, B. L. (2007). Monitoring corrosion of rebar embedded in mortar using guided ultrasonic waves. (Order No. 3290229, University of Illinois at Urbana-Champaign). ProQuest Dissertations and Theses,330. Retrieved from http://search.proquest.com/docview/304858430?accountid=14739. (304858430).

Frederiksen, J. (1993). *Chloride binding in concrete surfaces. Nordic Mini Seminar on Chlorides Pentration into Concrete Structures*, Chalmers University, Goetberg, Sweden.

Gjorv, O. E., Vennesland, O., & El-Busaidy, A. (1987). Diffusion of dissolved oxygen through concrete. *Mater.Performance;(United States), 25*(12).

Gowripalan, N., Sirivivatnanon, V., & Lim, C. (2000). Chloride diffusivity of concrete cracked in flexure. *Cement and Concrete Research, 30*(5), 725-730.

Heimovaara, T. J. (1992). Comments on "Time domain reflectometry measurements of water content and electrical conductivity of layered soil columns". *Soil Science Society of America Journal, 56*(5), 1657-1658.

Hall, C., & Hoff, W. D. (2009). *Water transport in brick, stone and concrete*. CRC PressI Llc.

Heimovaara, T. (1993). Design of triple-wire time domain reflectometry probes in practice and theory. *Soil Science Society of America Journal*,57(6), 1410-1417.

Henryk, S., & Zbigniew, S. (2005). Calibration of TDR instruments for moisture measurement of aerated concrete. *Monitoring and Modelling the Properties of Soil as Porous Medium*, 158.

Hodgkiess, T., Arthur, P., & Earl, J. (1983). Corrosion fatigue of reinforced concrete in sea water. *Corrosion*, 83.

Ismail, M., Toumi, A., Francois, R., & Gagné, R. (2004). Effect of crack opening on the local diffusion of chloride in inert materials. *Cement and Concrete Research, 34*(4), 711-716.

Jaffer, S. J., & Hansson, C. M. (2009). Chloride-induced corrosion products of steel in cracked-concrete subjected to different loading conditions. *Cement and Concrete Research, 39*(2), 116-125.

Jacobsen, O. H., & Schjønning, P. (1993). Field evaluation of time domain reflectometry for soil water measurements. *Journal of Hydrology,151*(2), 159-172.

Jacobsen, O. H., & Schjønning, P. (1993). A laboratory calibration of time domain reflectometry for soil water measurement including effects of bulk density and texture. *Journal of Hydrology,151*(2), 147-157.

Jones, S. B., Wraith, J. M., & Or, D. (2002). Time domain reflectometry measurement principles and applications. *Hydrological Processes,16*(1), 141-153.

Knight, J. (1992). Sensitivity of time domain reflectometry measurements to lateral variations in soil water content. *Water Resources Research,28*(9), 2345-2352.

Koch, G. H., Brongers, M. P. H., Thompson, N. G., Virmani, Y. P., & Payer, J. H. (2001). *Corrosion costs and preventive strategies in the United States. Report by CC Technologies Laboratories, Inc. to Federal Highway Administration (FHWA), Office of Infrastructure Research and Development*. Report FHWA-RD-01-156.

Korhonen, C. J., Janoo, V. C., & Berini, C. M. (1997). *Time-Domain Reflectometry of Water Content in Portland Cement Concrete*, No. CRREL-SP-97-27). Cold regions research and engineering lab, Hanover, NH, USA.

Kumar, A. (2010). *Water Flow and Transport of Chloride in Unsaturated Concrete* (Master's thesis. University of Saskatchewan, Saskatoon, Canada). Retrieved from http://hdl.handle.net/10388/etd-07132010-144542.

Macdonald, D. D. (1992). The point defect model for the passive state. *Journal of the Electrochemical Society*, *139*(12), 3434-3449.

Malan, F., & Ahmet, K. (2002). *Monitoring moisture in concrete with an embedded transmission line (9DBMC-2002 Paper 141).* University of Luton, England.

Matano, C. (1933). On the relation between the diffusion-coefficients and concentrations of solid metals (the nickel-copper system). *Jpn. J. Phys*, 8(3), 109-113.

Mehta, P. K., & Monteiro, P. J. (2006). *Concrete: microstructure, properties, and materials.* McGraw-Hill New York.

Mindess, S., & Young, J. F. (1981). Concrete, Prentice Hall. *Englewood Cliffs, NJ*, 481.

Moskvin, V. M. (1983). *Concrete and reinforced concrete deterioration and protection.* Mir Publishers.

Mualem, Y. (1976). A new model for predicting the hydraulic conductivity of unsaturated porous media. *Water Resources Research*,*12*(3), 513-522.

Munson, B. R., Young, D. F., & Okiishi, T. H. (1990). *Fundamentals of fluid mechanics.* New York.

Nilsson, L. O. (1993). Penetration of chlorides into concrete structures—an introduction and some definitions. *Nordic Miniseminar on Chloride Penetration Into Concrete Structures, Chalmers University of Technology, Göteborg, Sweden*, 7-17.

Noborio, K. (2001). Measurement of soil water content and electrical conductivity by time domain reflectometry: A review. *Computers and Electronics in Agriculture, 31*(3), 213-237.

Miyagawa, K. O. T. (1980). Chloride Corrosion of Reinforcing Steel in Cracked Concrete. *ACI Special Publication*, 65.

Page, C. L., & Treadaway, K. W. J. (1982). Aspects of the electrochemistry of steel in concrete.

Persson, M., Berndtsson, R., Nasri, S., Albergel, J., Zante, P., & Yumegaki, Y. (2000). Solute transport and water content measurements in clay soils using time domain reflectometry. *Hydrological Sciences Journal, 45*(6), 833-847.

Pettersson, K. (1996). Criteria for cracks in connection with corrosion in high-strength concrete, 4th int. *Symp. Utilisation of High-Strength/High-Performance Concrete, Paris*, 509-517.

Ramadani, T. (2013). *Effect of Silica Fume on Moisture Flow and the Advective-Dispersive Transport of Ionic Species in Unsaturated Concrete* (Master's thesis, University of Saskatchewan, Saskatoon, Canada). Retrieved from http://hdl.handle.net/10388/ETD-2013-04-977.

Rhoades, J., Raats, P., & Prather, R. (1976). Effects of liquid-phase electrical conductivity, water content, and surface conductivity on bulk soil electrical conductivity. *Soil Science Society of America Journal, 40*(5), 651-655.

Richards, L. A. (1931). Capillary conduction of liquids through porous mediums. *Physics,*1(5), 318-333.

Rodriguez, O. G., & Hooton, R. D. (2003). Influence of cracks on chloride ingress into concrete. *ACI Materials Journal,* 100(2).

Savage, B. M., & Janssen, D. J. (1997). Soil physics principles validated for use in predicting unsaturated moisture movement in portland cement concrete. *ACI Materials Journal,* 94(1).

Schiessl, P. (1988). *Corrosion of steel in concrete: Report of the technical committee 60 CSC, RILEM (the international union of testing and research laboratories for materials and structures)* Chapman & Hall.

Schiessl, P., & Raupach, M. (1997). Laboratory studies and calculations on the influence of crack width on chloride-induced corrosion of steel in concrete. *ACI Materials Journal*, 94(1).

Schneider, S., Mallants, D., & Jacques, D. (2011). Determining hydraulic properties of concrete and mortar by inverse modelling. MRS Proceedings. MRS Fall Meeting-Symposium NW–Scientific Basis for Nuclear Waste Management XXXV, Buenos Aires, Argentina, 2-7.

Skierucha, W., Malicki, M. A., & Walczak, R. T. (2004). *TDR method for the measurement of water content and salinity of porous media.* IA PAS.

Suchorab, Z., & Widomski, M. (2011). Determination of salinity changes in building materials using electric methods. *Proceedings of ECOpole*, *5*(1).

Topp, G., Davis, J., & Annan, A. P. (1980). Electromagnetic determination of soil water content: Measurements in coaxial transmission lines. *Water Resour.Res, 16*(3), 574-582.

Topp, G. C., Zebchuk, W. D., Davis, J. L., & Bailey, W. G. (1984). The measurement of soil water content using a portable TDR hand probe. Canadian Journal of Soil Science, 64(3), 313-321.

Topp, G., Yanuka, M., Zebchuk, W., & Zegelin, S. (1988). Determination of electrical conductivity using time domain reflectometry: Soil and water experiments in coaxial lines. *Water Resources Research*, 24(7), 945-952.

Transportation Research Board (1991). National Research Council (US). *Highway deicing: comparing salt and calcium magnesium acetate, special Report* 235, National Research Council, Washington, DC.

Van Genuchten, M. T. (1980). A closed-form equation for predicting the hydraulic conductivity of unsaturated soils. *Soil Science Society of America Journal*, 44(5), 892-898.

Vesikari, E. (1988). *Service life of concrete structures with regard to corrosion of reinforcement* Res. Reports, Espoo, Finland.

Wang, K., Jansen, D. C., Shah, S. P., & Karr, A. F. (1997). Permeability study of cracked concrete. *Cement and Concrete Research,* 27(3), 381-393.

Wilkins, N., & Lawrence, P. (1980). *Fundamental mechanism of corrosion of steel reinforcements in concrete immersed in sea water.* Cement and concrete association.

Wilkins, N., & Stillwell, J. (1986). The corrosion of steel reinforcement in cracked concrete immersed in seawater. *Proc.Marine Concrete,* 86.

Win, P. P., Watanabe, M., & Machida, A. (2004). Penetration profile of chloride ion in cracked reinforced concrete. *Cement and Concrete Research,* 34(7), 1073-1079.

Zhang, R. (1997). Determination of soil sorptivity and hydraulic conductivity from the disk infiltrometer. *Soil Science Society of America Journal,* 61(4), 1024-1030.

Appendix (A) Colour-scaled images in wetting phase

The volumetric water content around the crack was tested with TDR following the steps described in Section 3.6.4. The 8×8 or 6×8 dielectric constant data sets were collected and then converted to water content through the calibration equation (Equation 2.36). The distribution of saturation level in the probed area was presented by colour-scaled images; a linear interpolation was employed to improve the data visualization.

The full records of plots for saturation from time 0 to 296 hours for all sample are shown in this appendix. At 296 hour, all the samples were assumed to be fully saturated, and it is not shown here for better figure arrangement. In these figures, the artificial cracks are shown as a straight line at the middle position and the natural cracks are shown with two lines digitized from the real crack shape, a solid line for the front face, a dotted line for the back face, and a dash-dotted line representing the averaged crack shape of the front and back cracks. The colour scale represents the saturation level.

These figures are labeled as “sample type (number)”,

where for the “sample type”,

A03: the 0.3 mm artificial crack
A10: the 1.0 mm artificial crack
N03: the 0.3 mm natural crack
N10: the 1.0 mm natural crack

For the “number”, 1-12 stand for the time steps (0 1 3 5 8 13 22 33 56 80 128 200) hour.

All the information designated by the label can also be found in title of each figure.

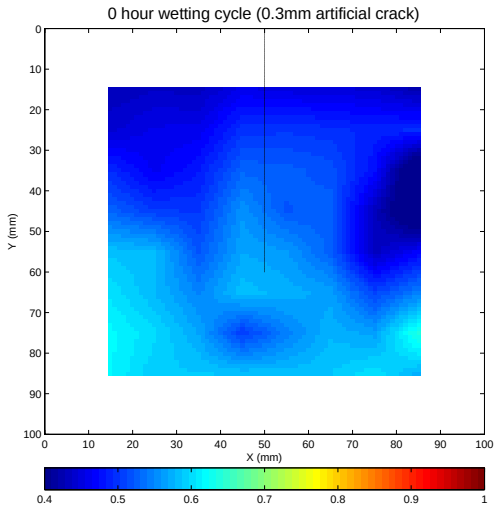

A03(1)

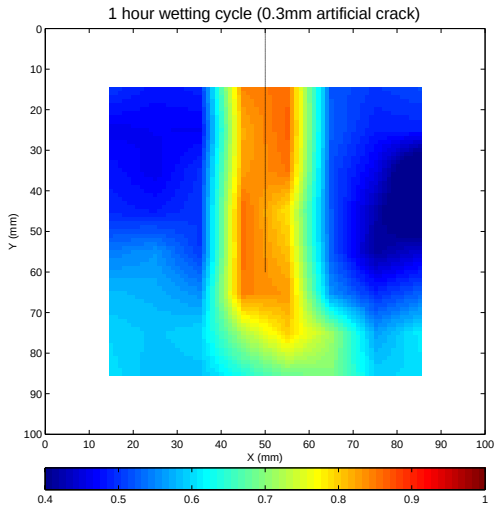

A03(2)

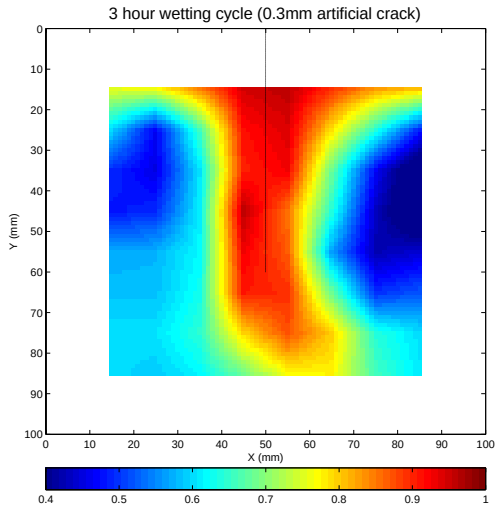

A03 (3)

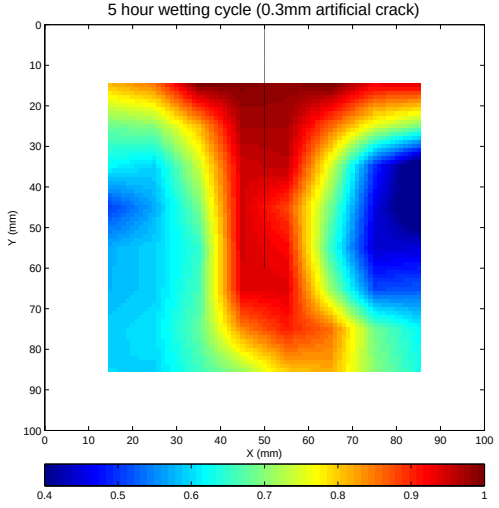

A03 (4)

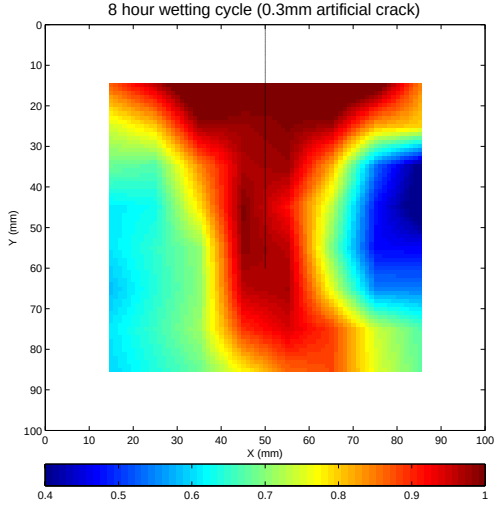

A03 (5)

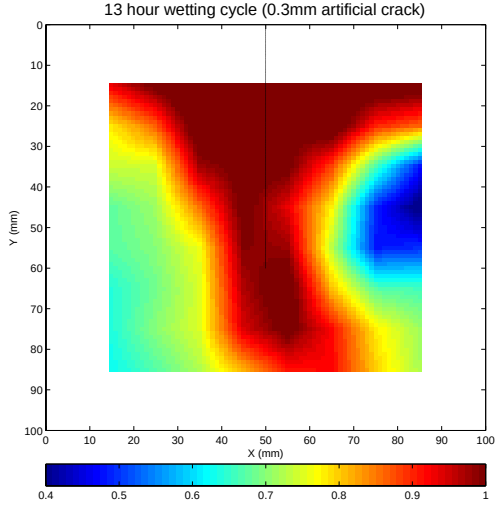

A03 (6)

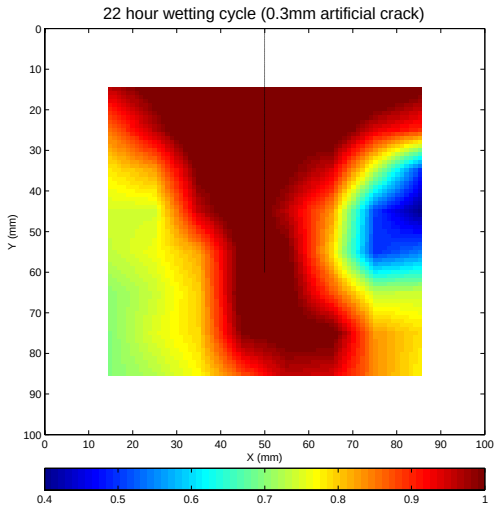

A03 (7)

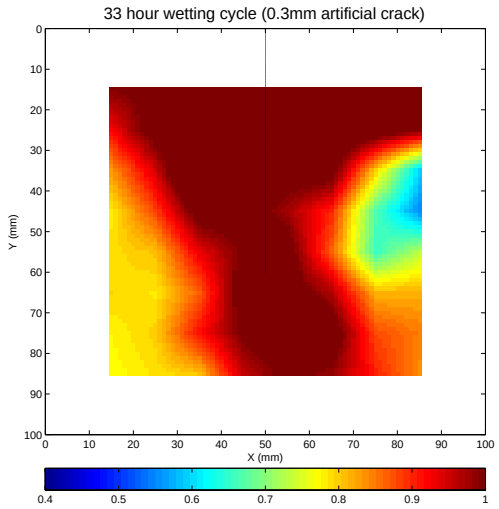

A03 (8)

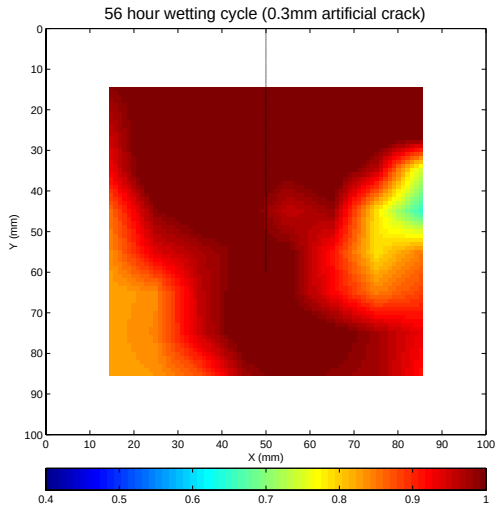

A03 (9)

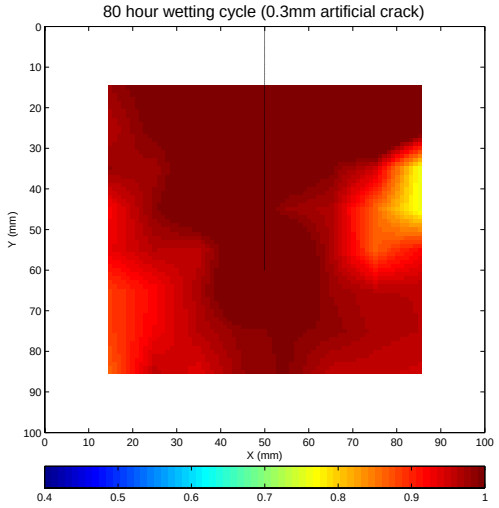

A03 (10)

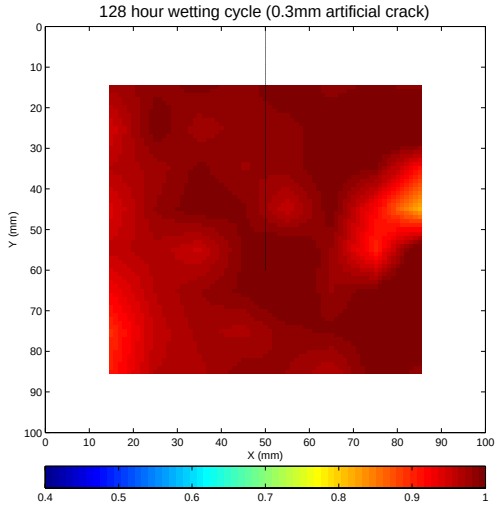

A03 (11)

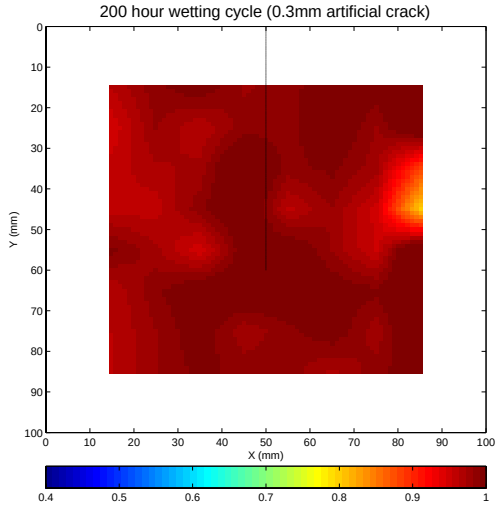

A03 (12)

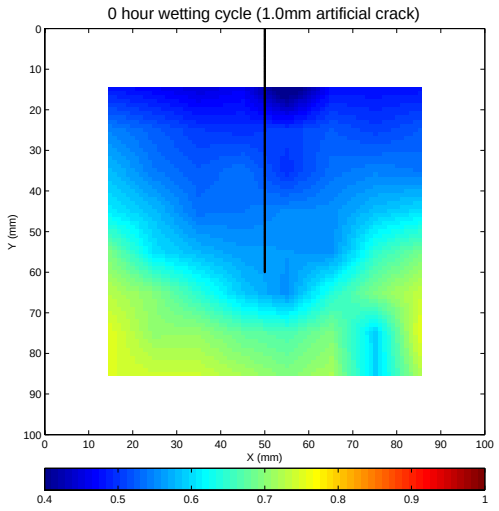

A10 (1)

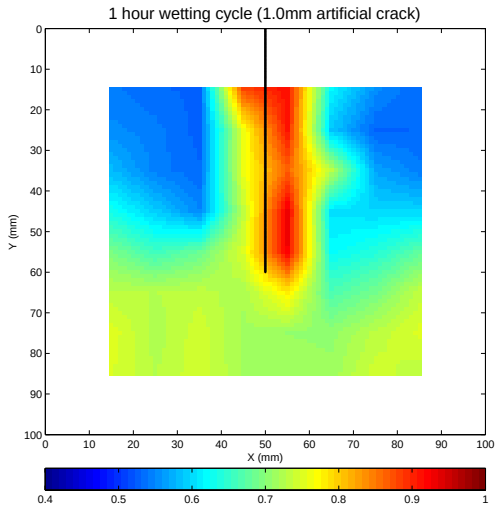

A10 (2)

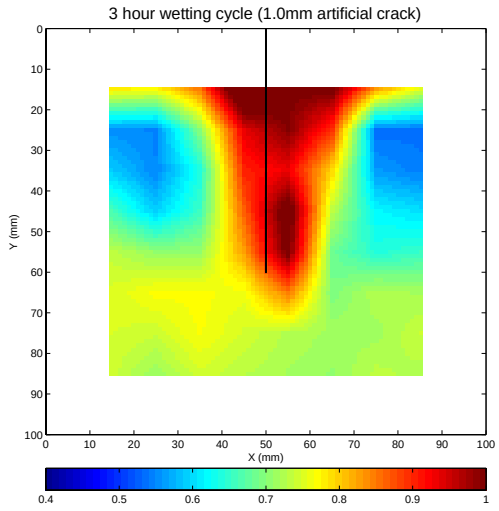

A10 (3)

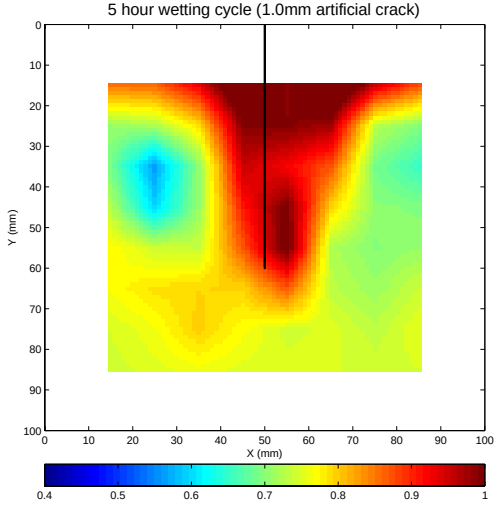

A10 (4)

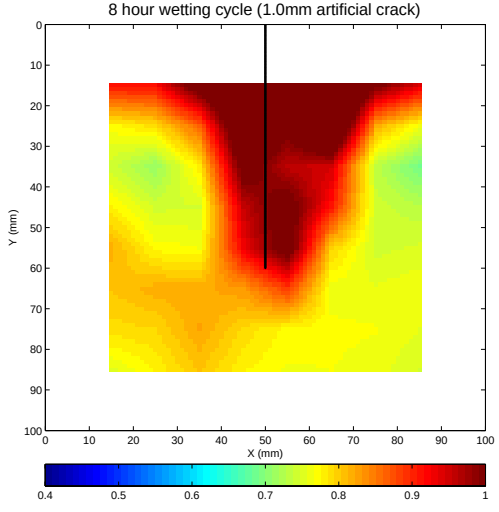

A10 (5)

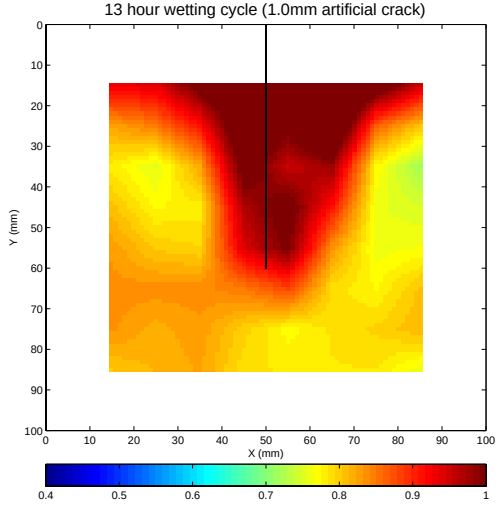

A10 (6)

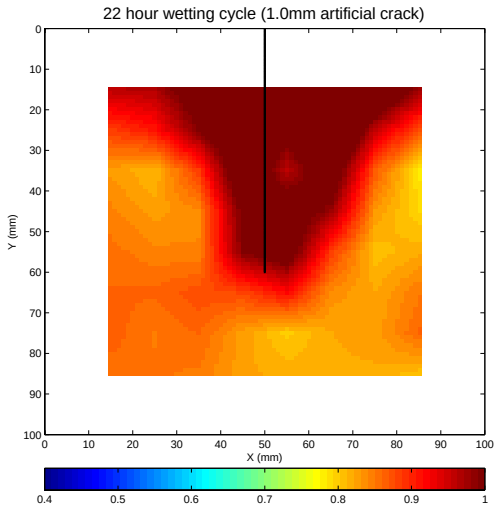

A10 (7)

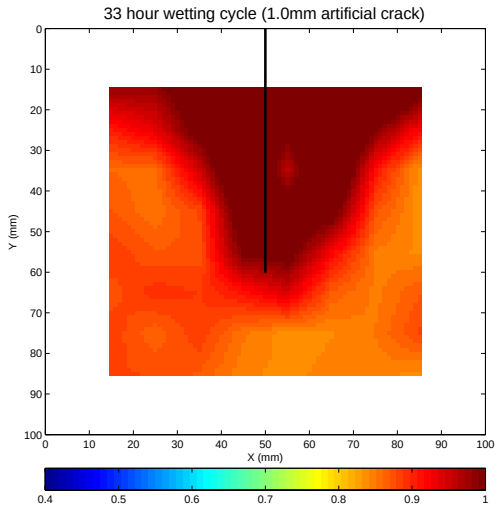

A10 (8)

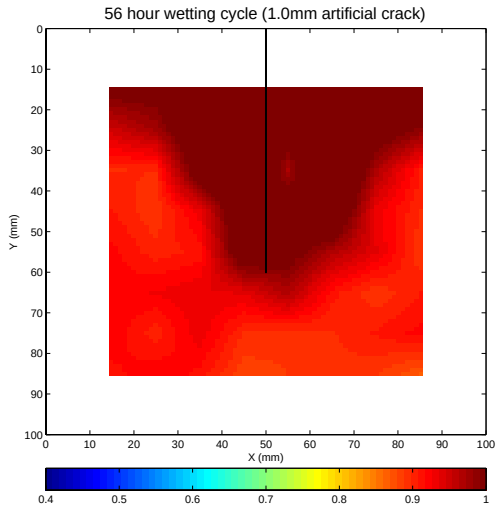

A10 (9)

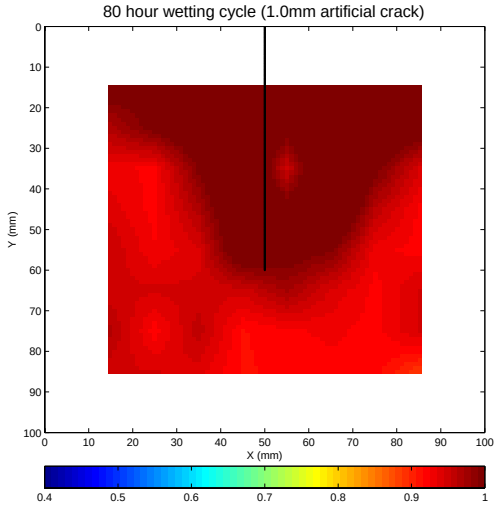

A10 (10)

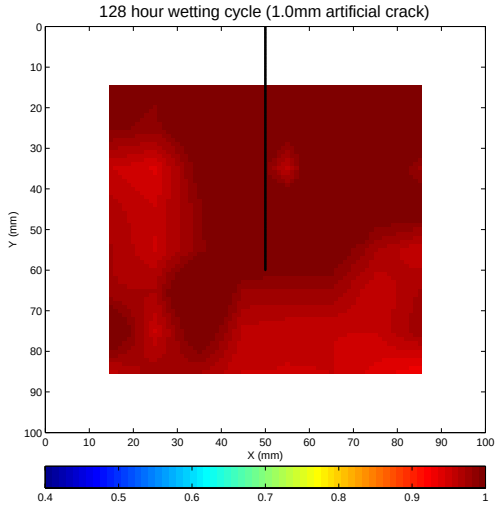

A10 (11)

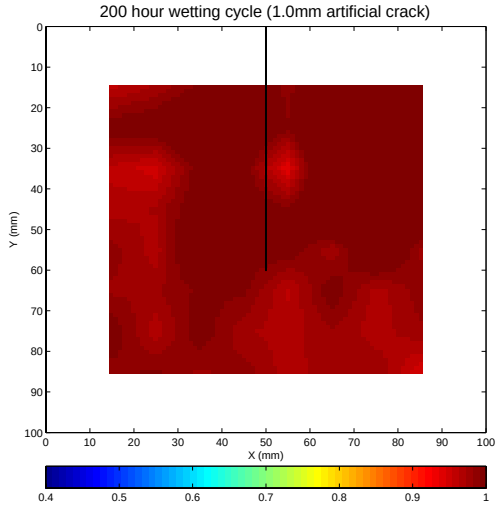

A10 (12)

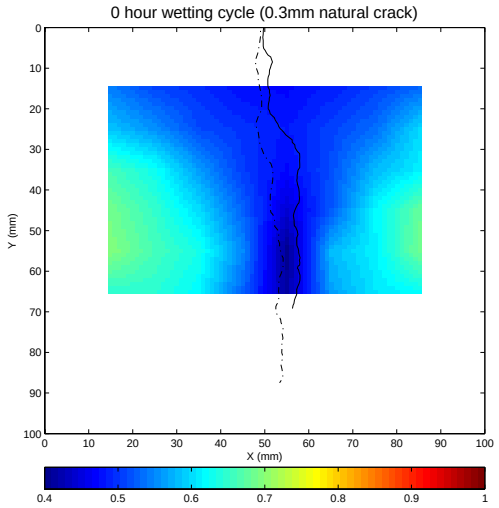

N03 (1)

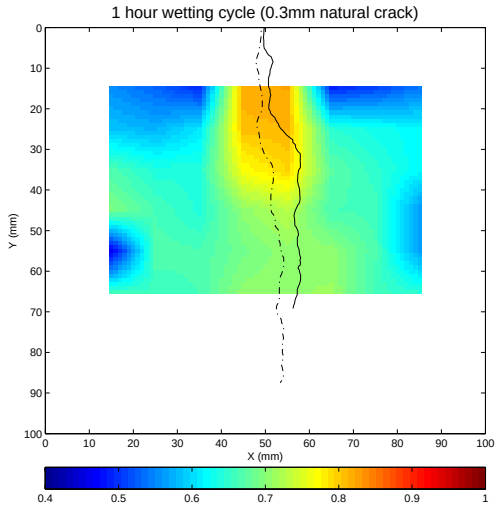

N03 (2)

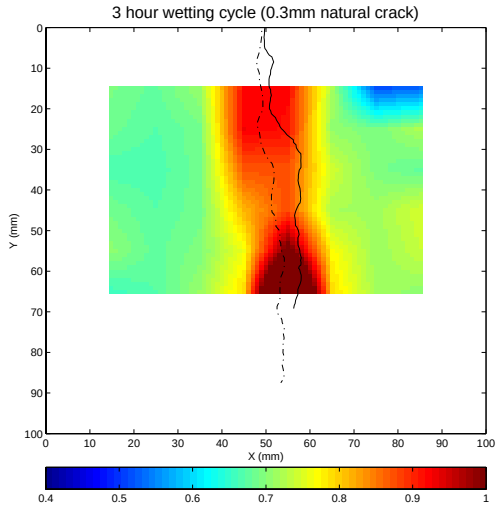

N03 (3)

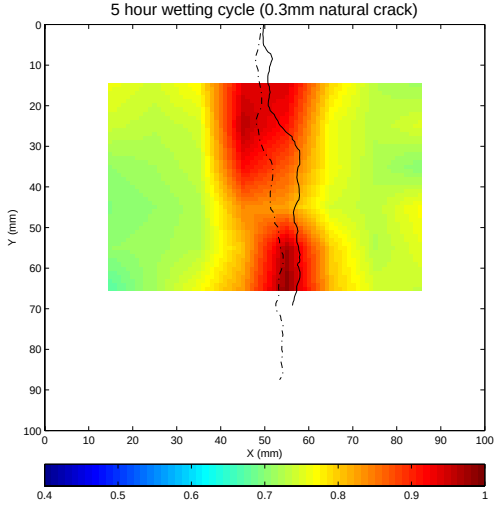

N03 (4)

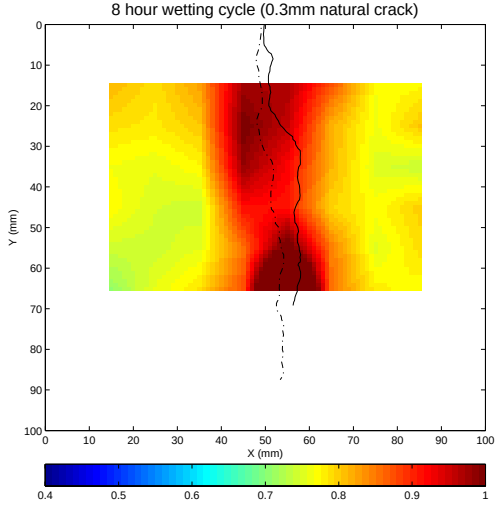

N03 (5)

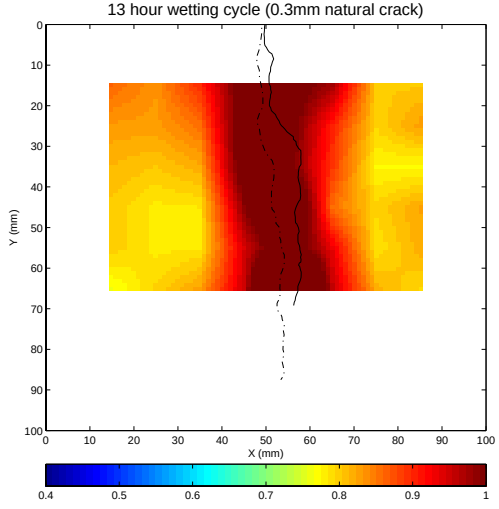

N03 (6)

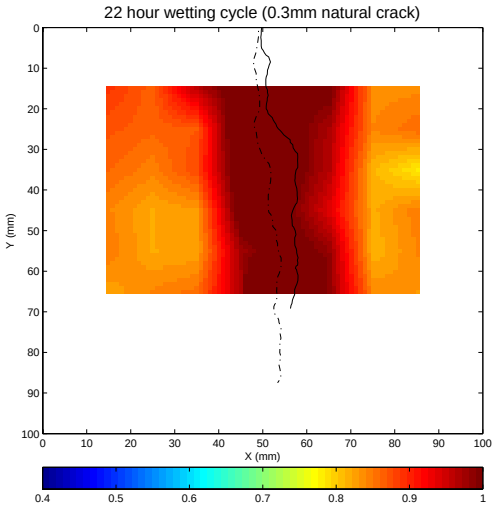

N03 (7)

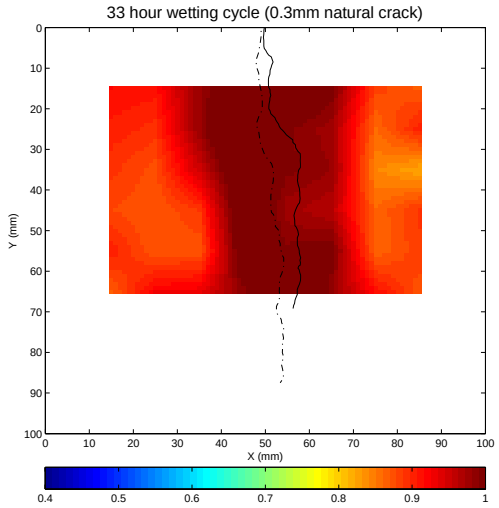

N03 (8)

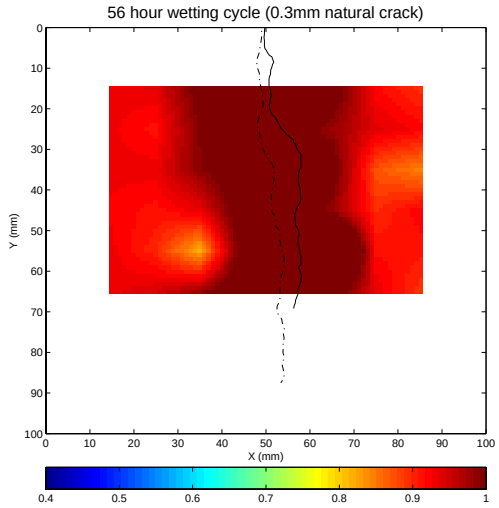

N03 (9)

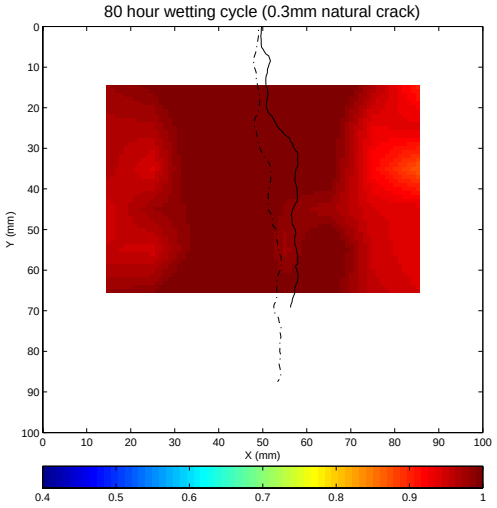

N03 (10)

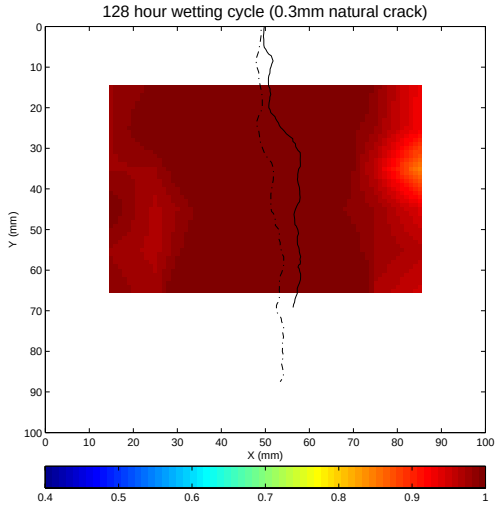

N03 (11)

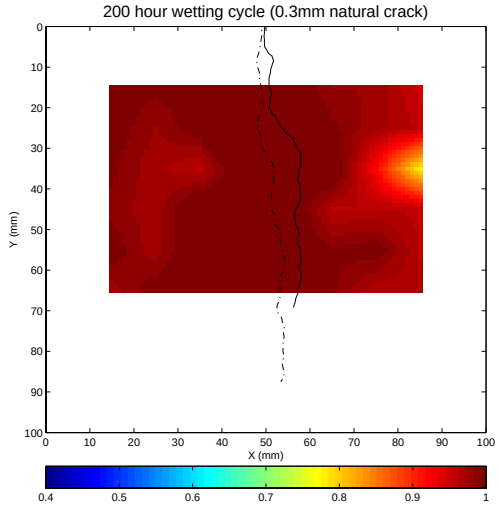

N03 (12)

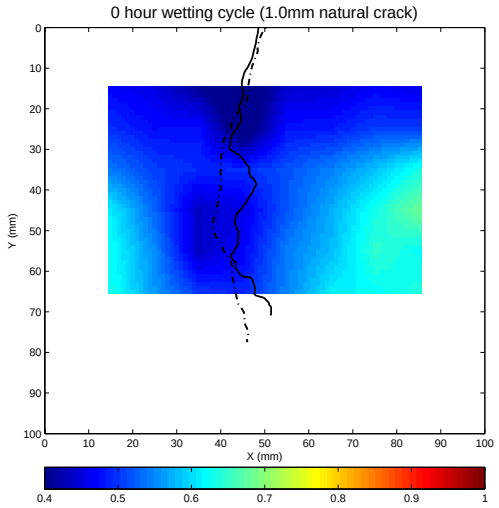

N10 (1)

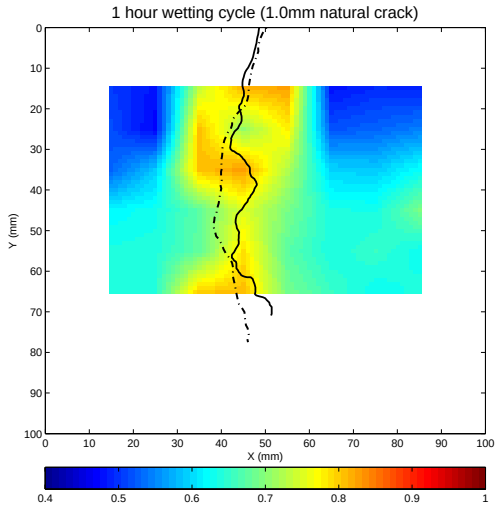

N10 (2)

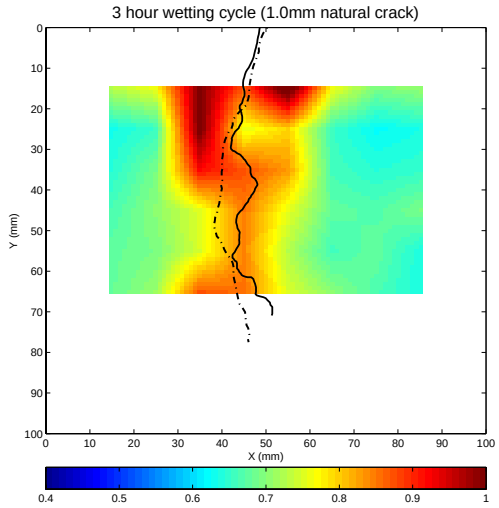

N10 (3)

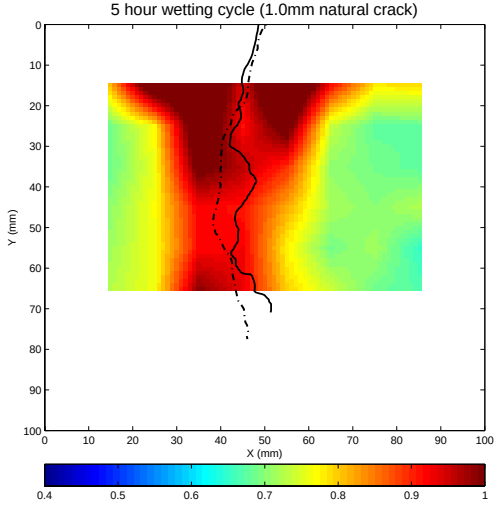

N10 (4)

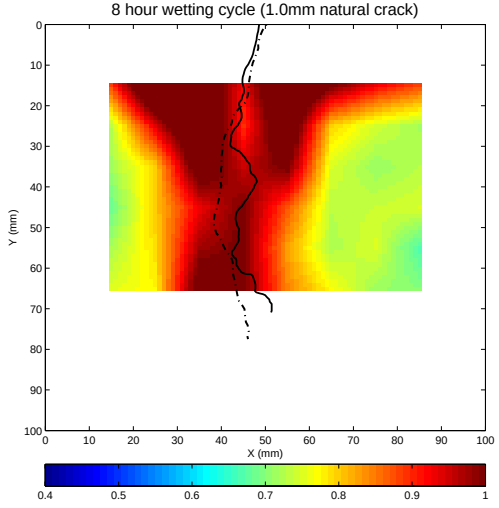

N10 (5)

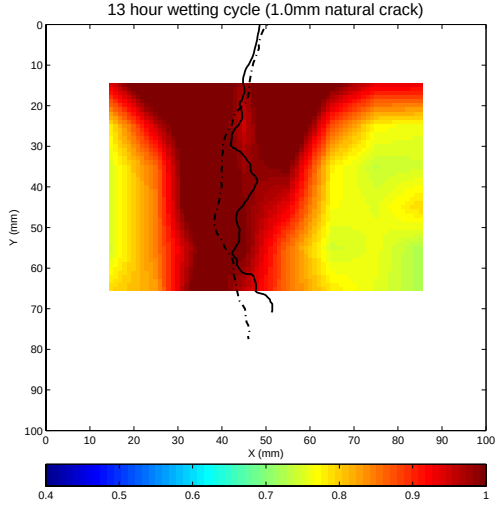

N10 (6)

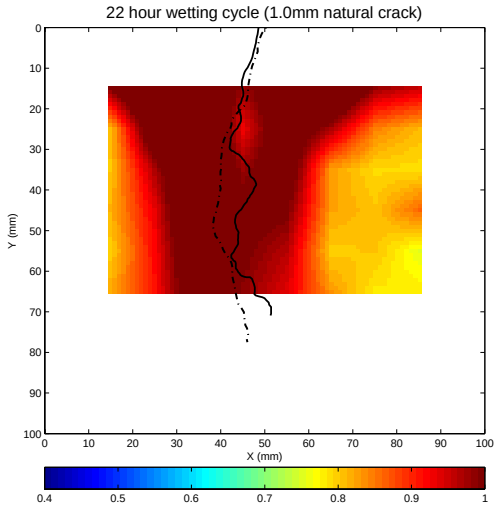

N10 (7)

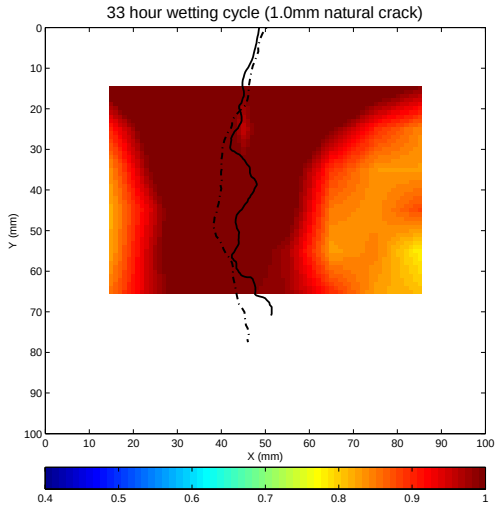

N10 (8)

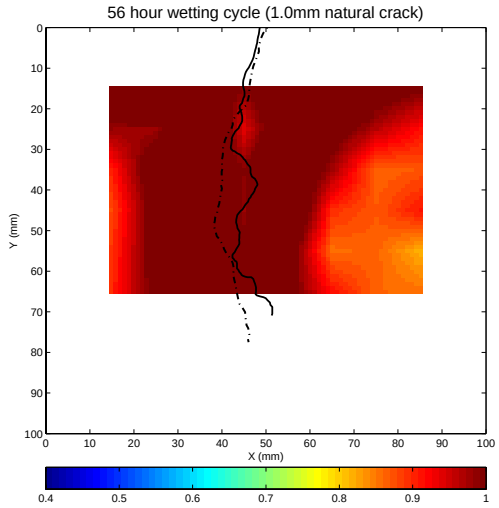

N10 (9)

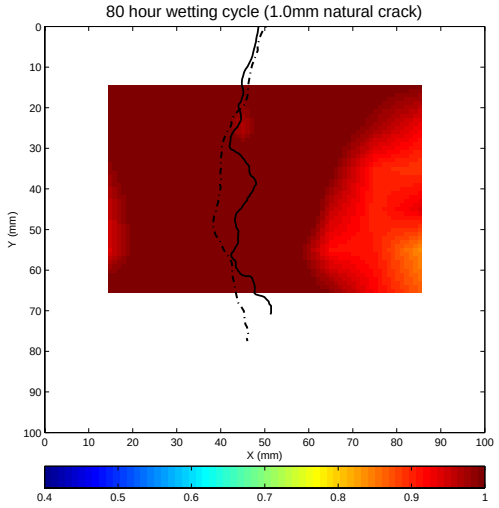

N10 (10)

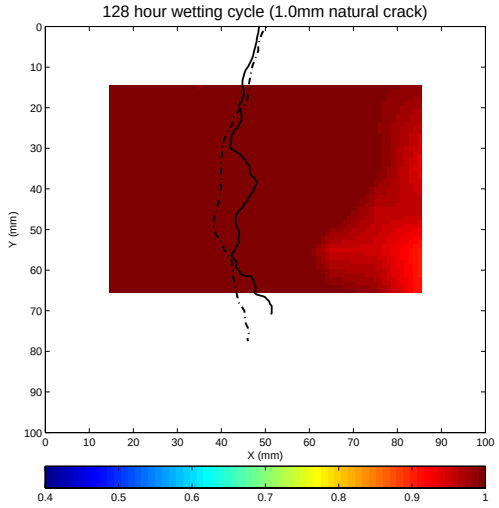

N10 (11)

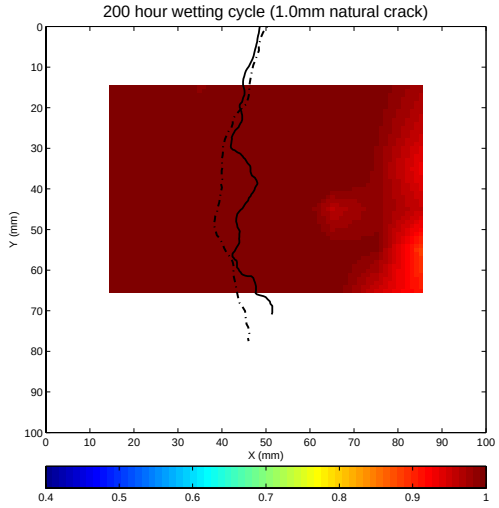

N10 (12)

Appendix (B) Colour-scaled images in drying phase

The volumetric water content around the crack was tested with TDR following the steps described in Section 3.6.4. The 8×8 or 6×8 dielectric constant data sets were collected and then converted to water content through the calibration equation (Equation 2.36). The distribution of saturation level in the probed area was presented by colour-scaled images; a linear interpolation was employed to improve the data visualization.

The full records of plots for saturation from time 0 to 2855 hours for all sample are shown in this appendix. In these figures, the artificial cracks are shown as a straight line at the middle position and the natural cracks are shown with two lines digitized from the real crack shape, a solid line for the front face, a dotted line for the back face, and a dash-dotted line representing the averaged crack shape of the front and back cracks. The colour scale represents the saturation level.

These figures are labeled as “sample type (number)”,

where for the “sample type”,

A03: the 0.3 mm artificial crack
A10: the 1.0 mm artificial crack
N03: the 0.3 mm natural crack
N10: the 1.0 mm natural crack

For the “number”, 1-11 stand for the time steps (0 4 11 23 47 95 167 263 407 695 2855) hour.

All the information designated by the label can also be found in title of each figure.

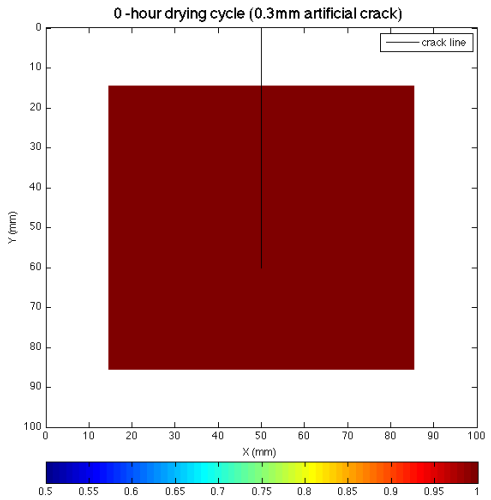

A03 (1)

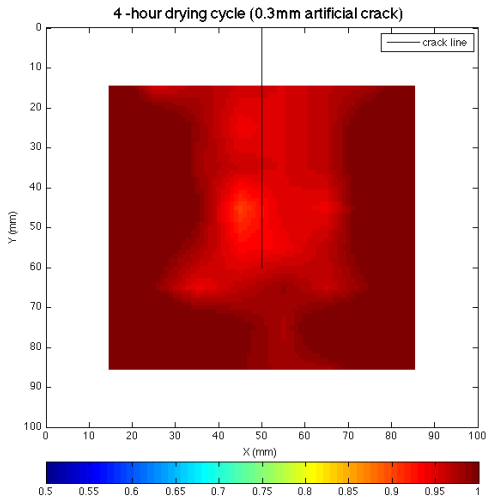

A03 (2)

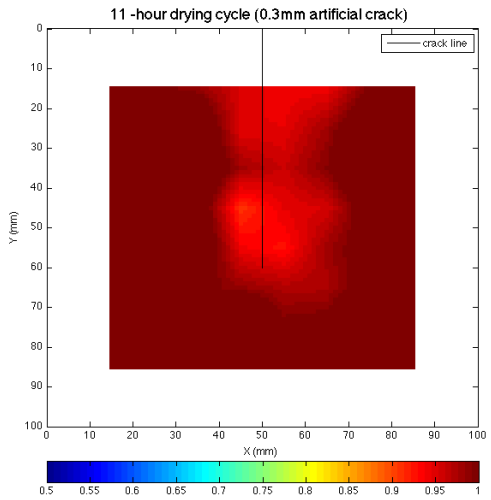

A03 (3)

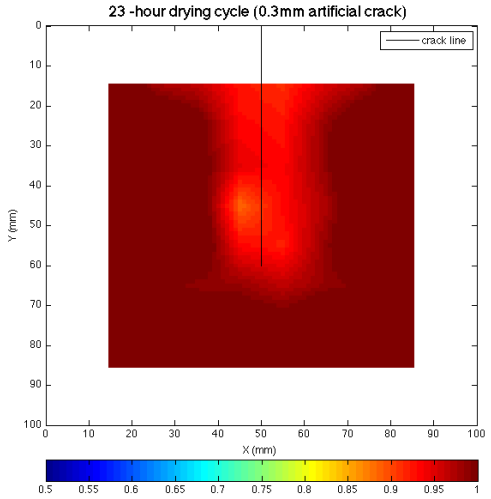

A03 (4)

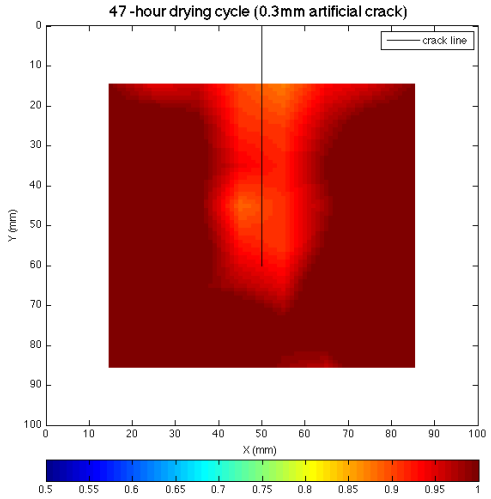

A03 (5)

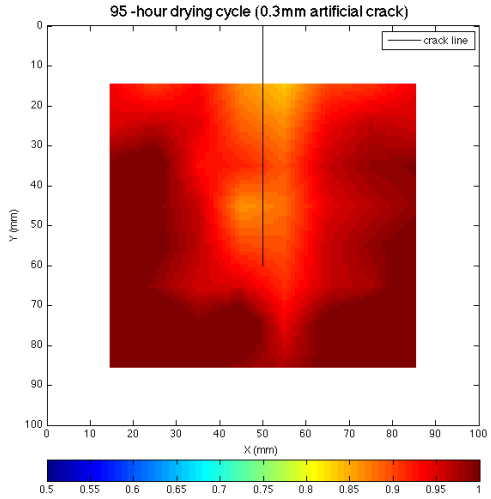

A03 (6)

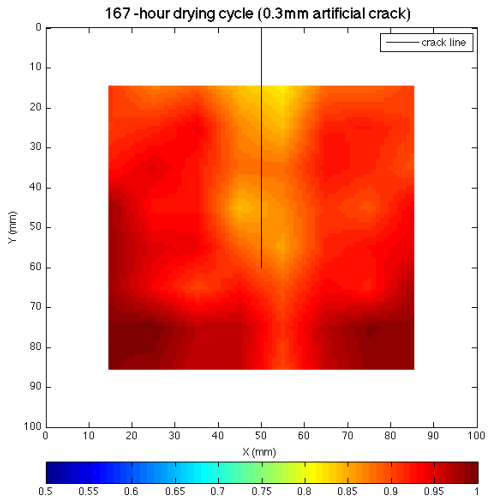

A03 (7)

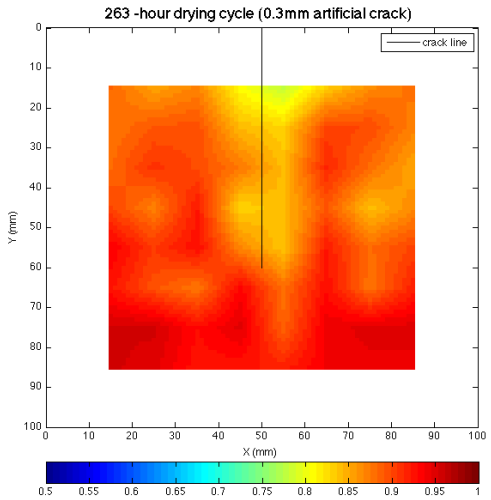

A03 (8)

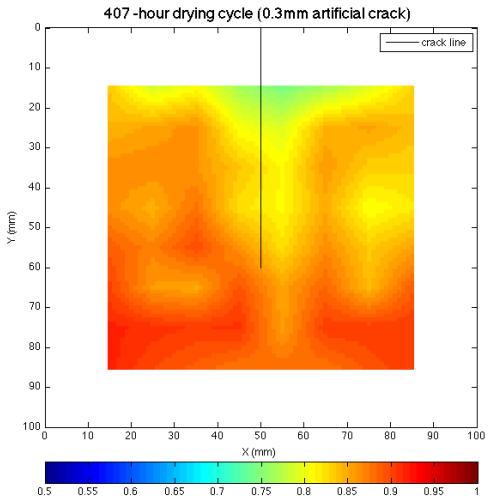

A03 (9)

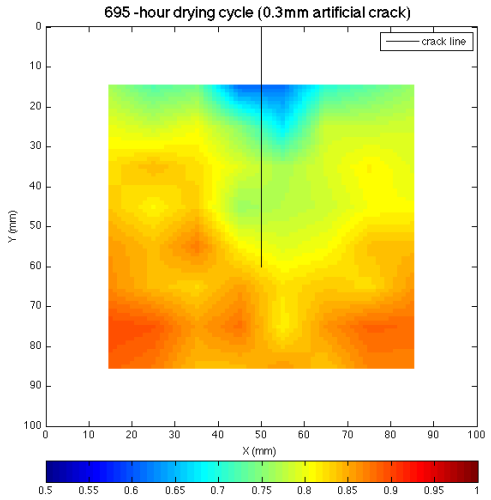

A03 (10)

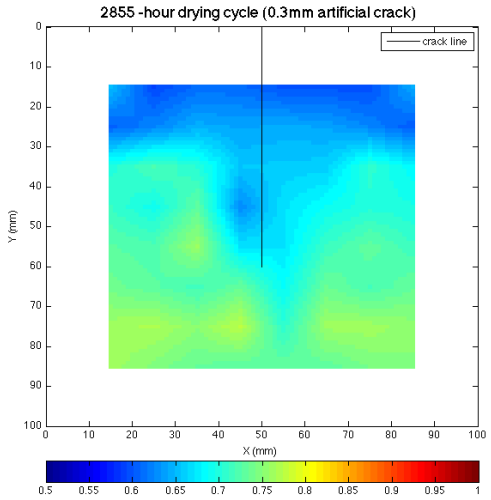

A03 (11)

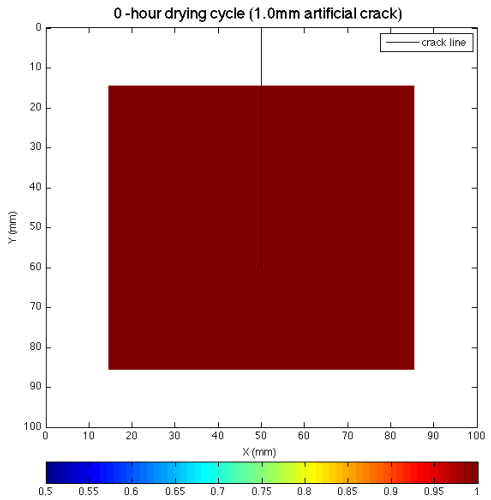

A10 (1)

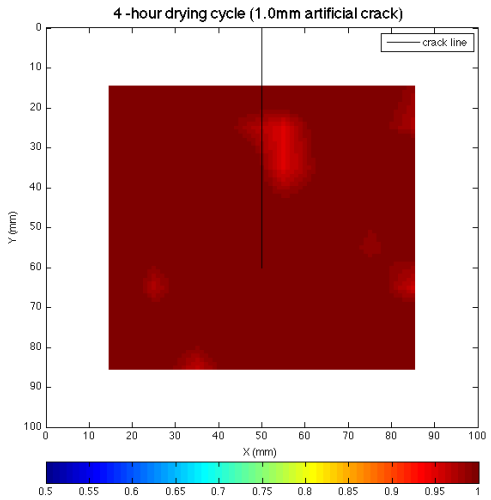

A10 (2)

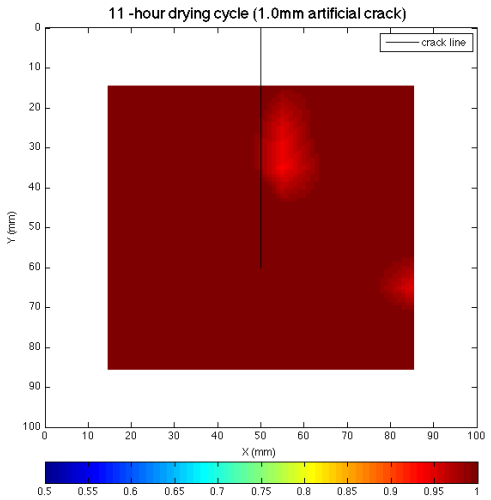

A10 (3)

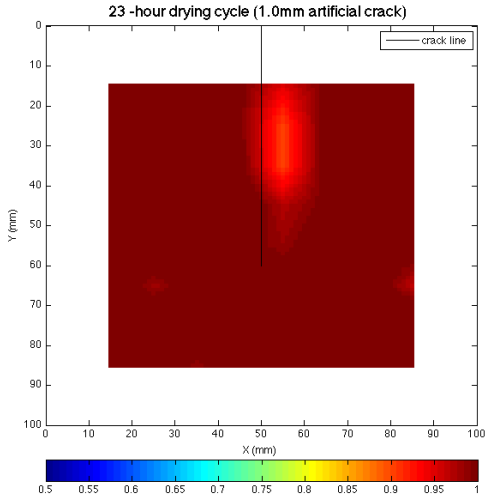

A10 (4)

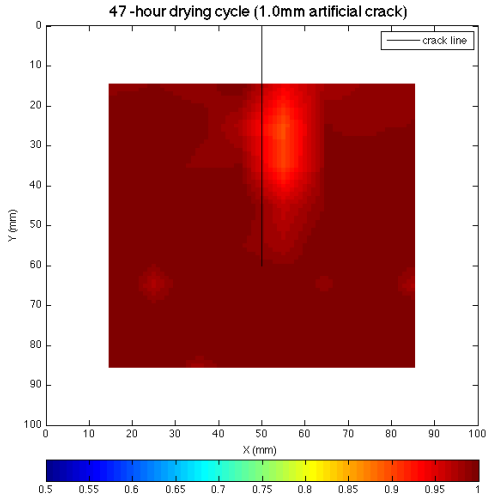

A10 (5)

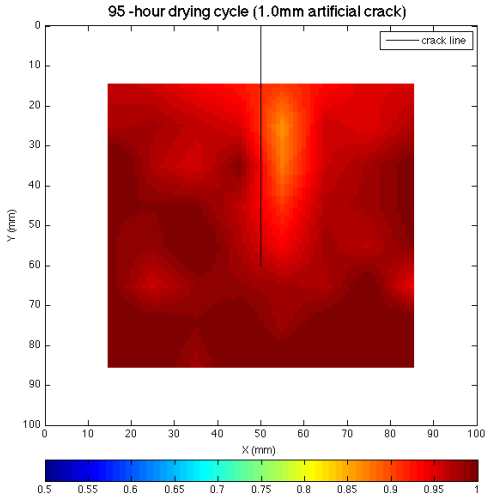

A10 (6)

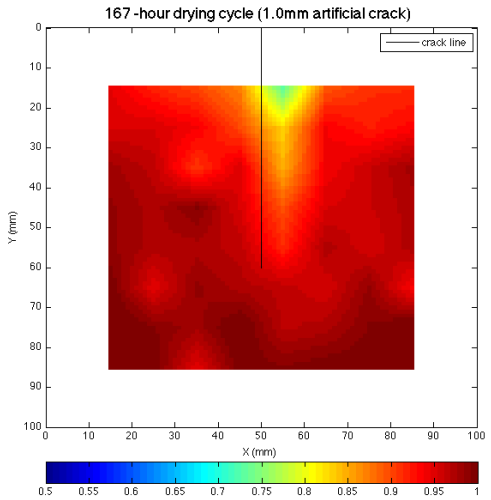

A10 (7)

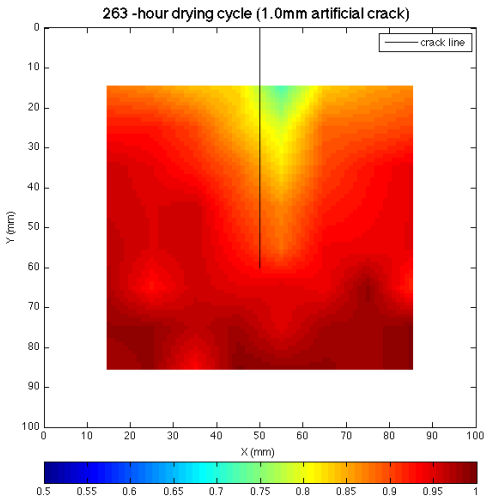

A10 (8)

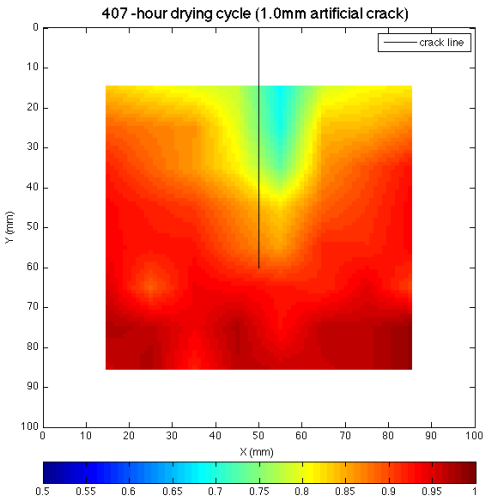

A10 (9)

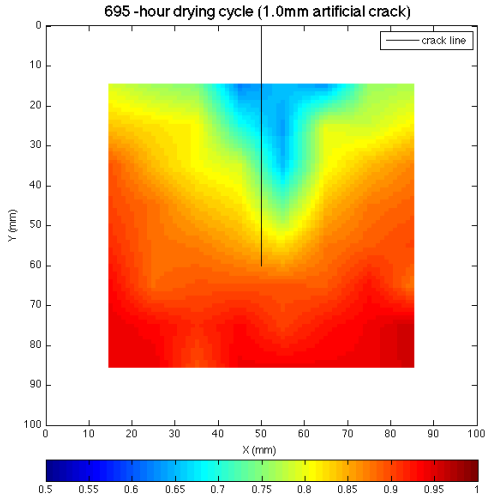

A10 (10)

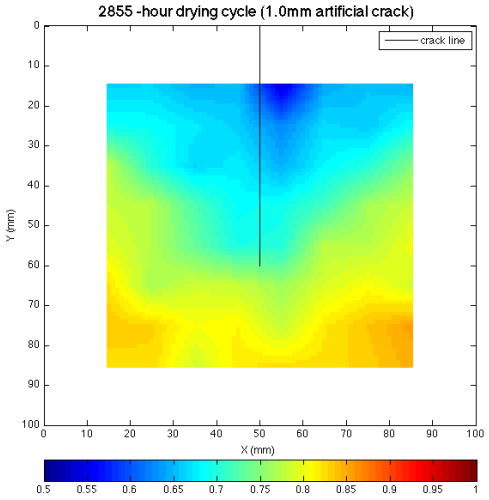

A10 (11)

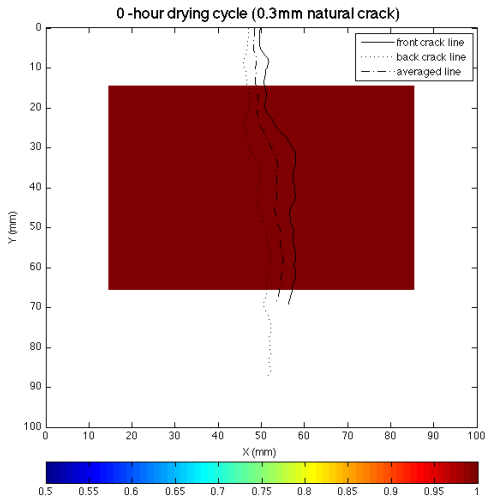

N03 (1)

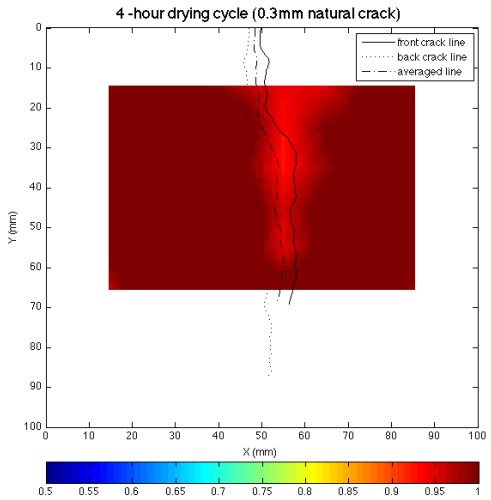

N03 (2)

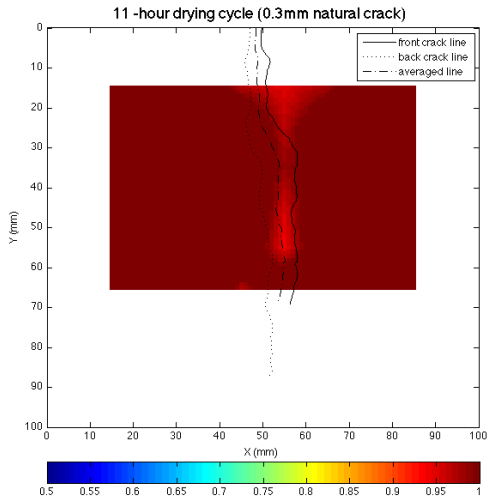

N03 (3)

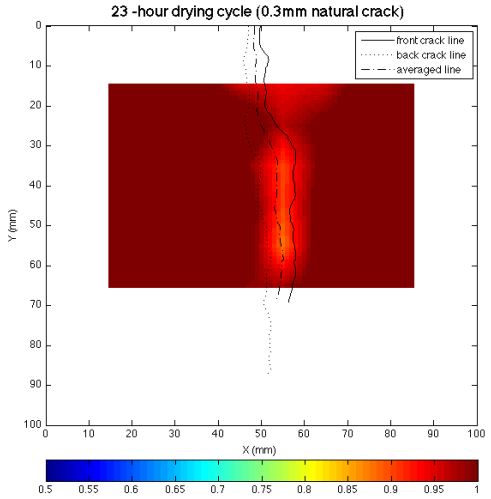

N03 (4)

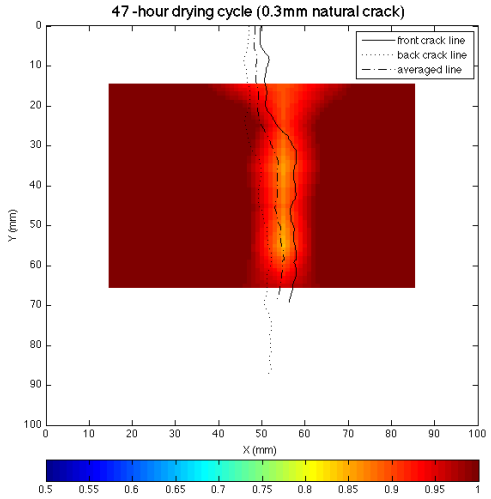

N03 (5)

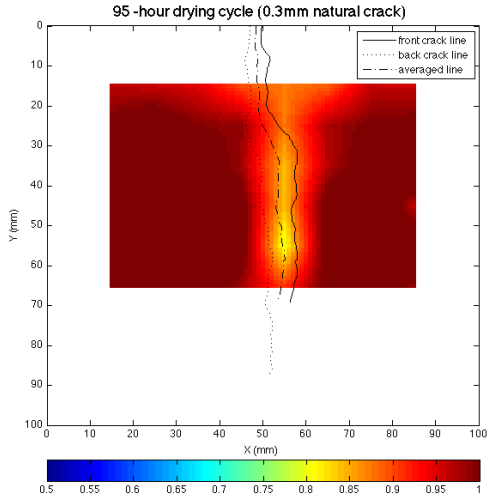

N03 (6)

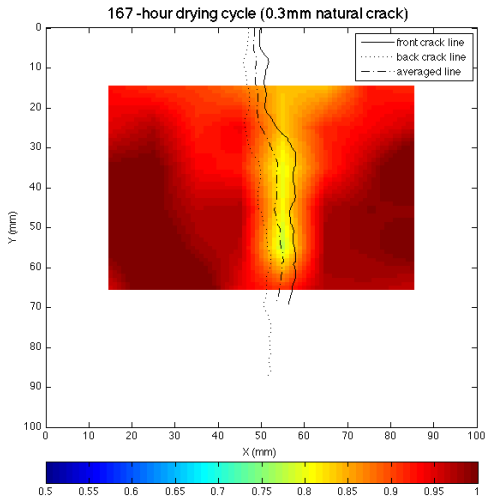

N03 (7)

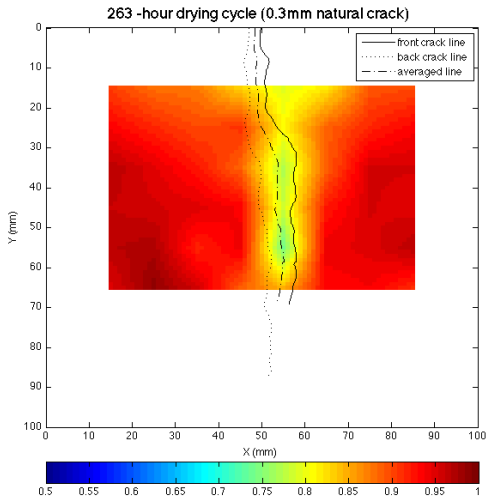

N03 (8)

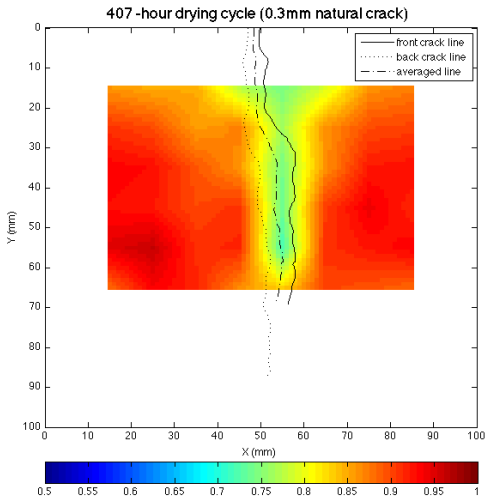

N03 (9)

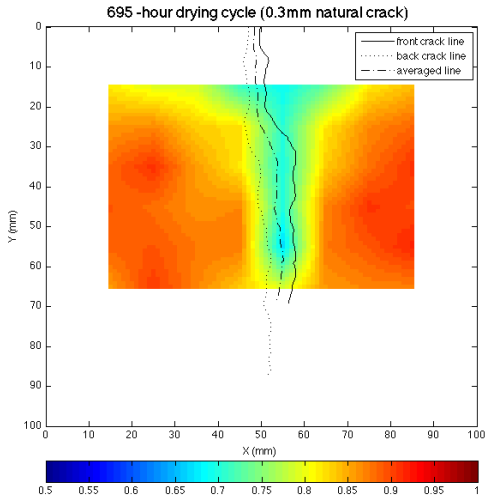

N03 (10)

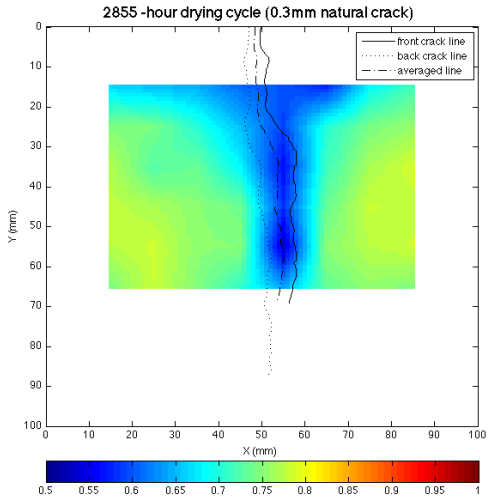

N03 (11)

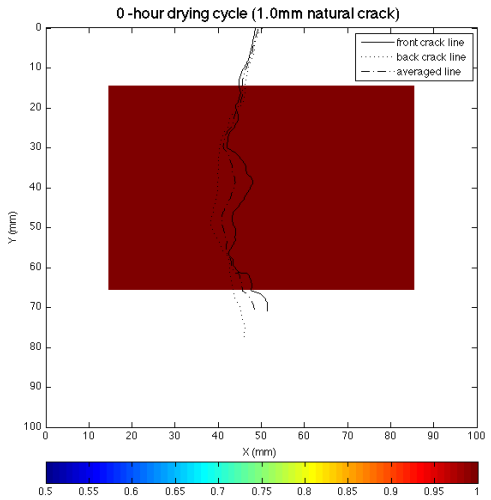

N10 (1)

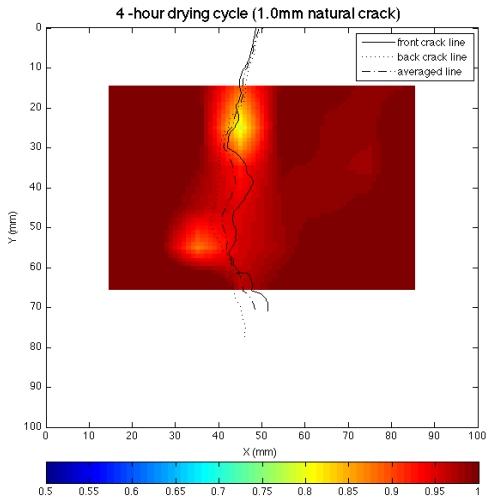

N10 (2)

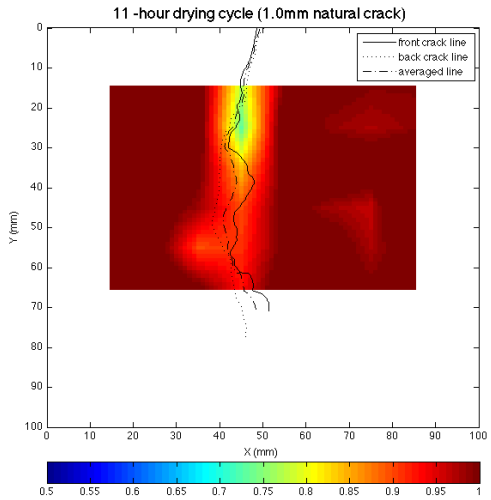

N10 (3)

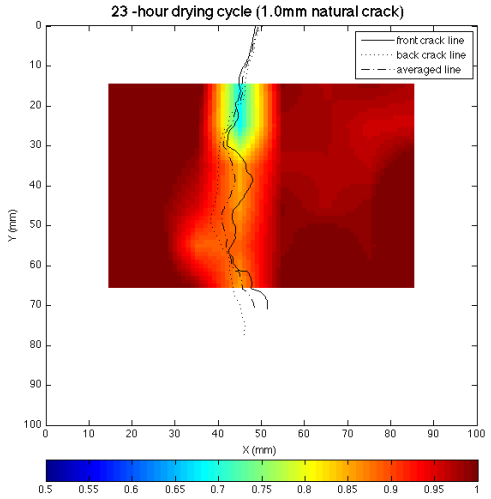

N10 (4)

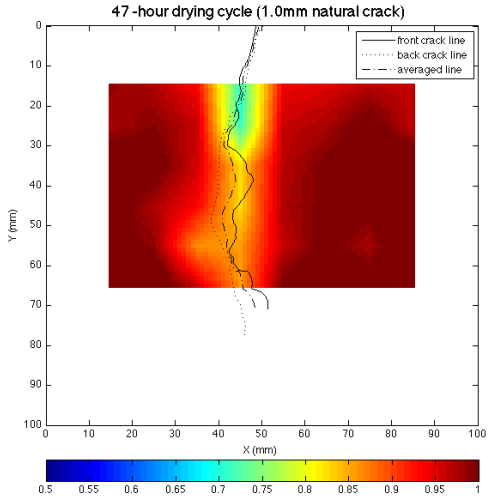

N10 (5)

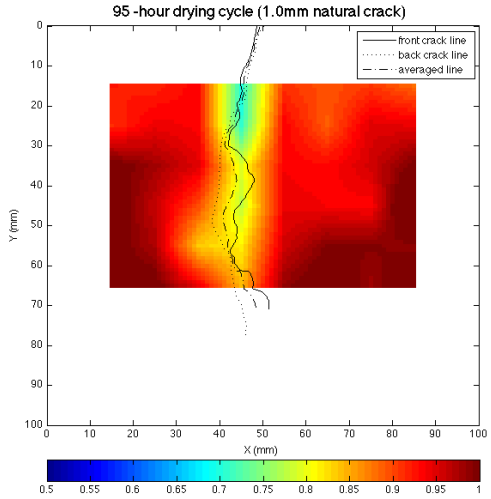

N10 (6)

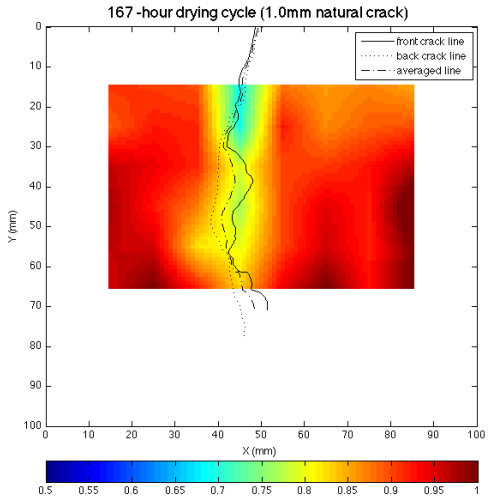

N10 (7)

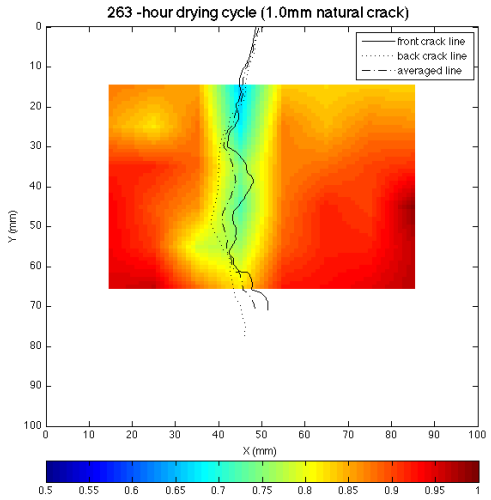

N10 (8)

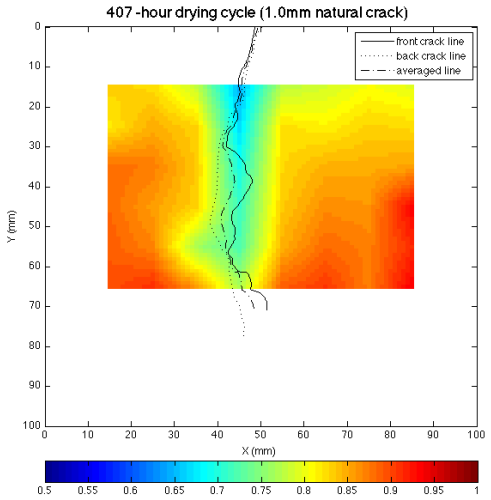

N10 (9)

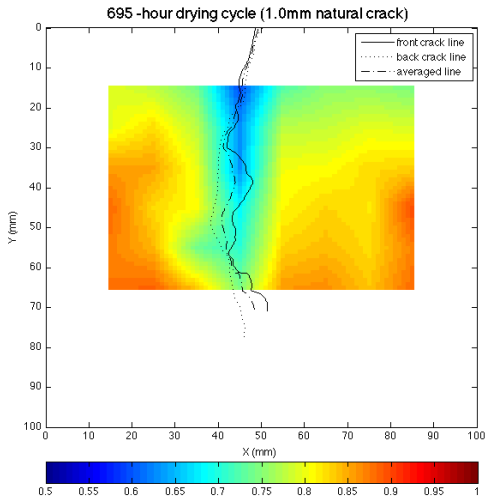

N10 (10)

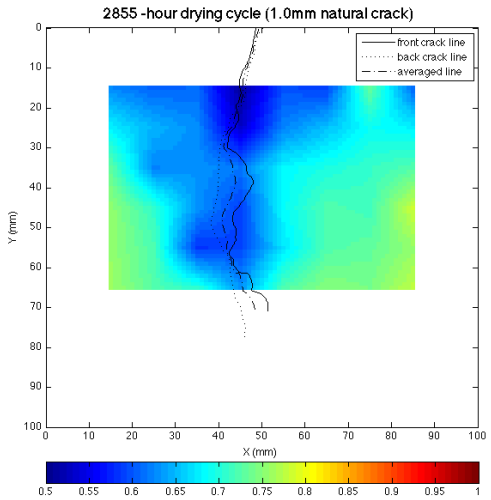

N10 (11)

Appendix (C) Model parameter fitting

An inverse modelling analysis was carried out by adjusting Ks, α and n to match the experimental data for water saturation change 3.5 cm away from the midspan at different depths, where the evolution of water saturation were least affected by the variation of the crack line. It was found that there is no single set of Van Genutchten parameters could be identified to satisfactorily simulate the saturation change in both wetting and drying phases. Therefore usage of different hydraulic properties was necessary in order to match the experimentally measure water saturation values distribution in space and time using an inverse modeling analysis. The trial and error was conducted for Ks between 2×10^{-10} m/s and 7×10^{-10} m/s for "n" between 1.3 and 1.4 for drying, and between 1.8 and 2.5 for wetting.

Ks should be the same value for both wetting and drying. "α" was found not sensitive in the data matching. The "n" is the main contributor to the hysteresis behaviour. In this appendix some typical trial examples are summarized as follows.

Wetting Ks= 2e-10 m/s n= 1.52

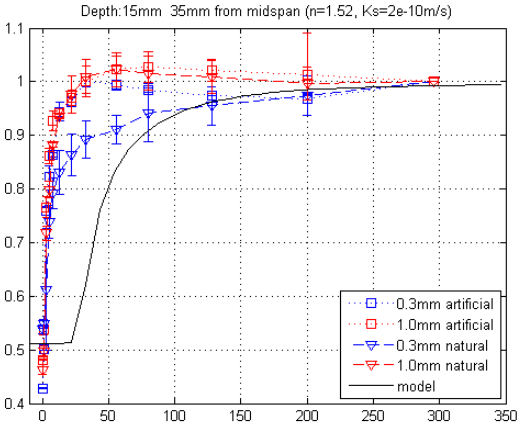

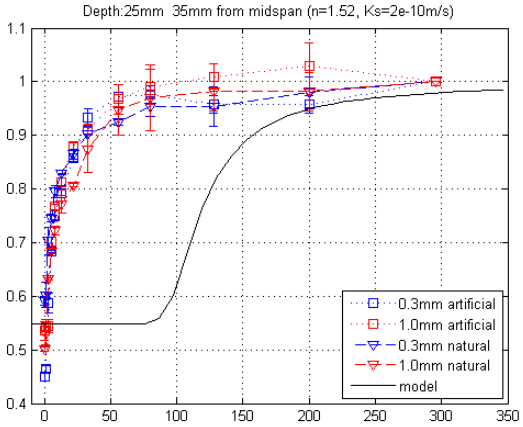

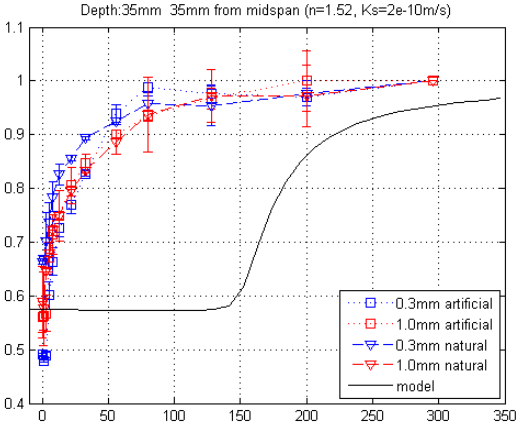

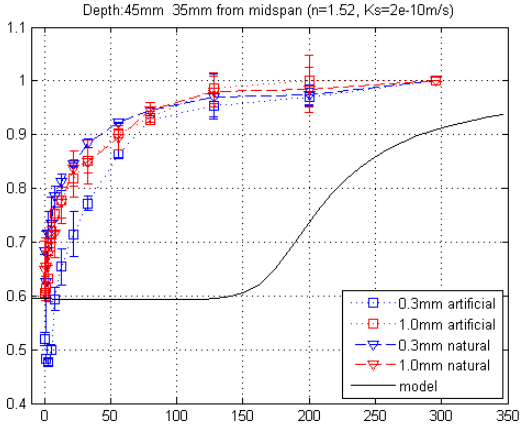

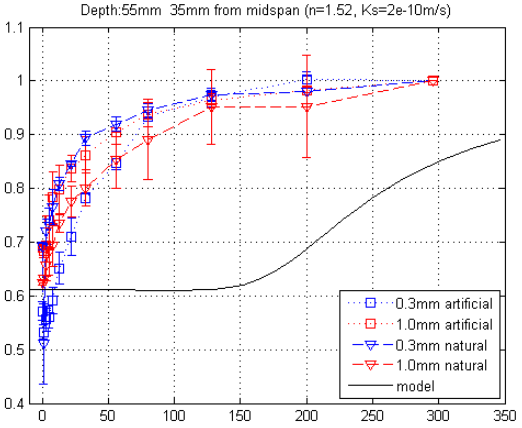

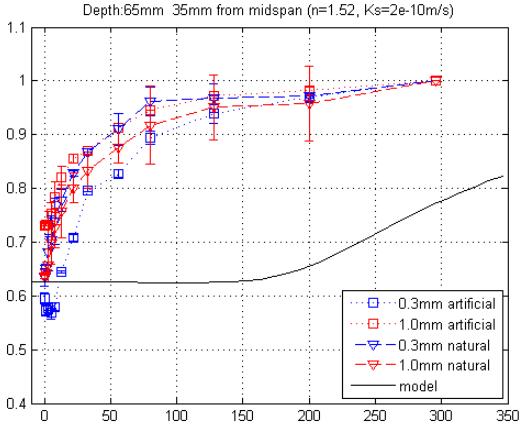

Wetting Ks= 2e-10 m/s n= 2.8

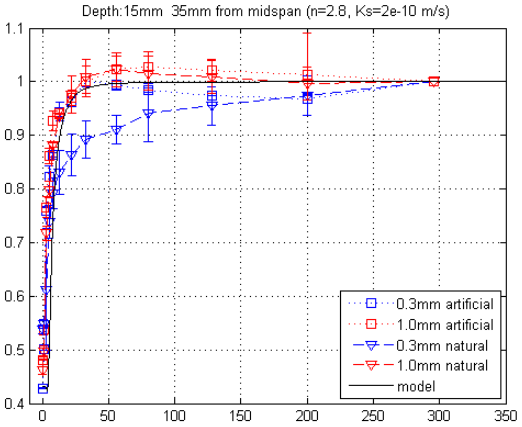

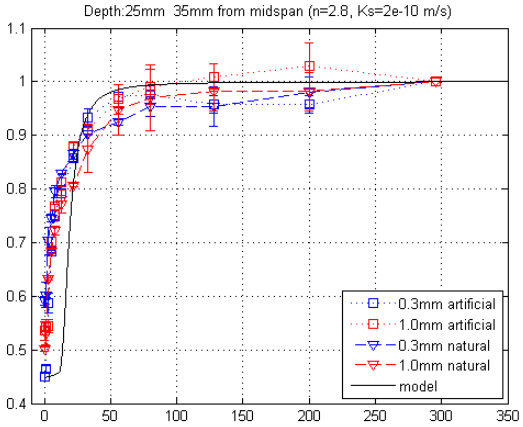

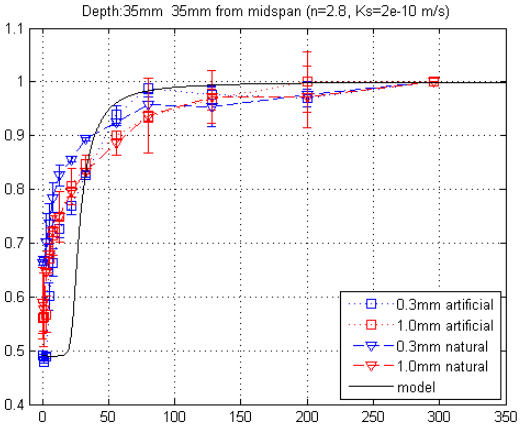

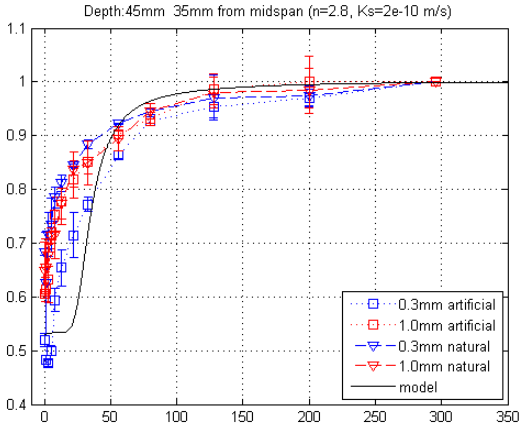

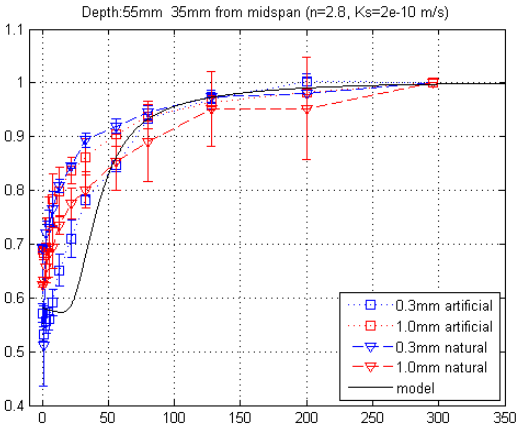

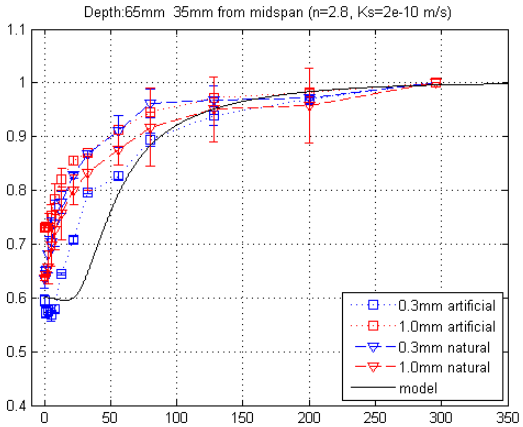

Wetting Ks= 7e-10 m/s n= 1.52

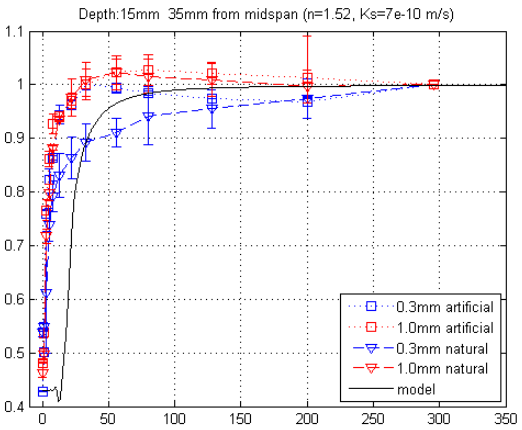

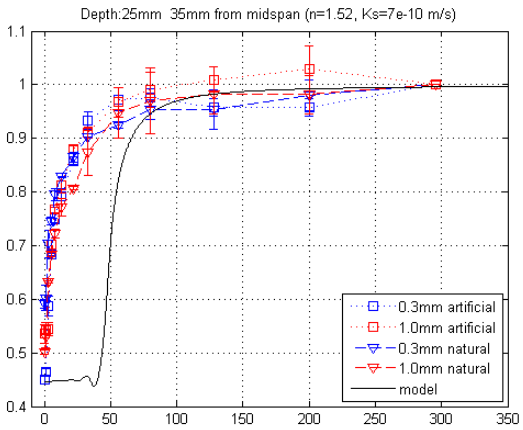

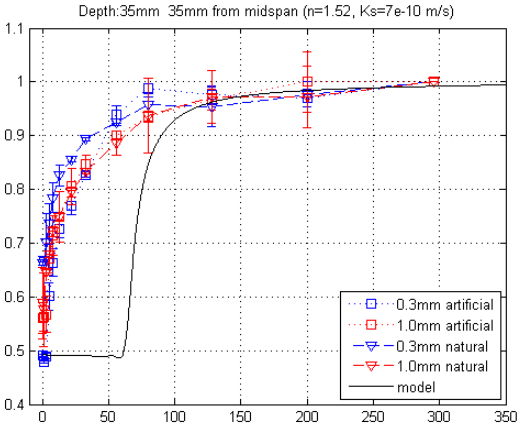

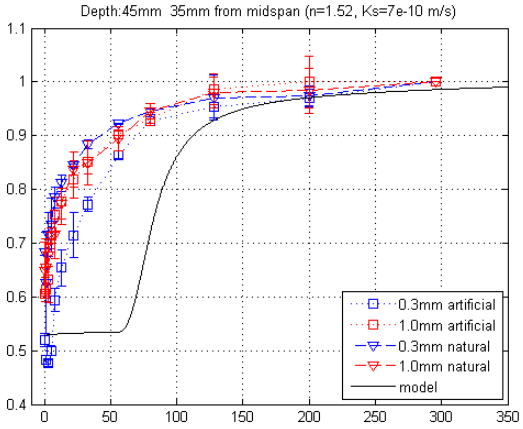

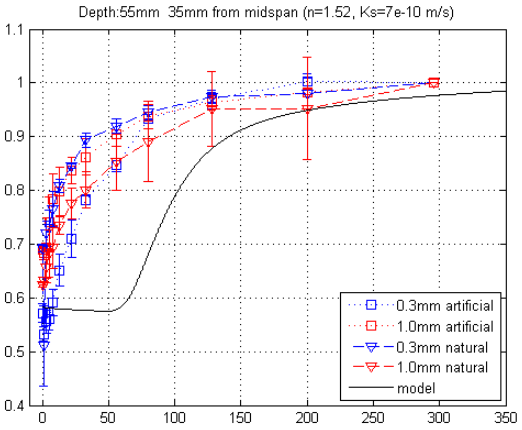

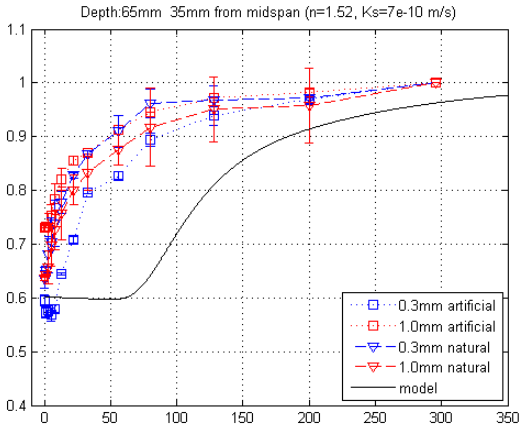

Wetting Ks=5e-10 m/s n=1.8

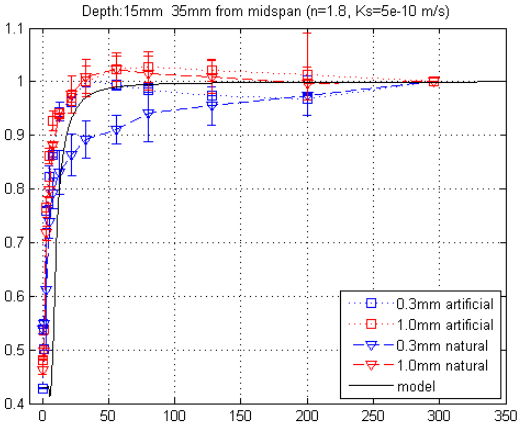

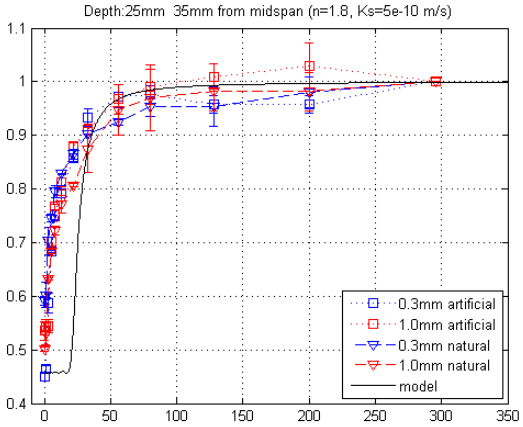

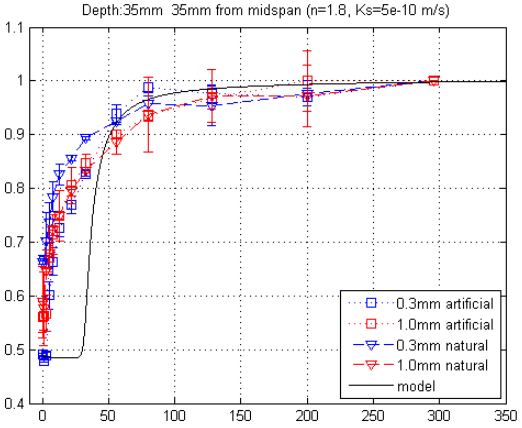

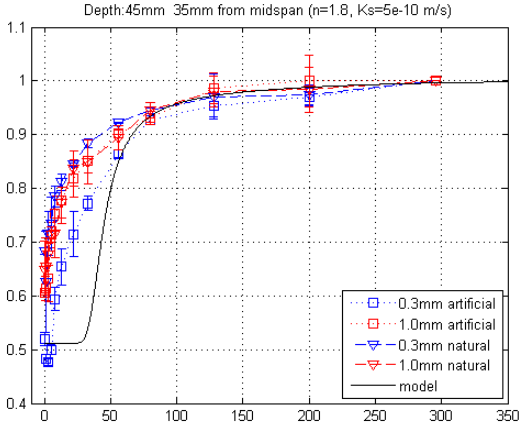

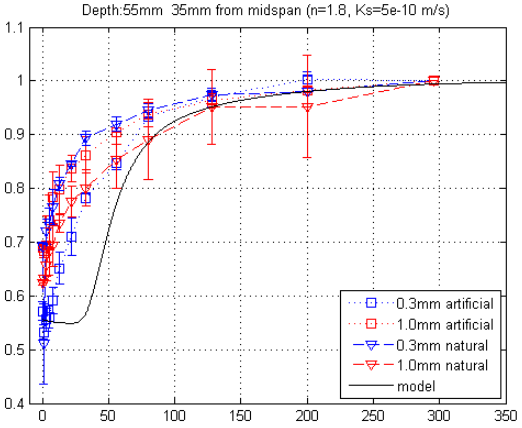

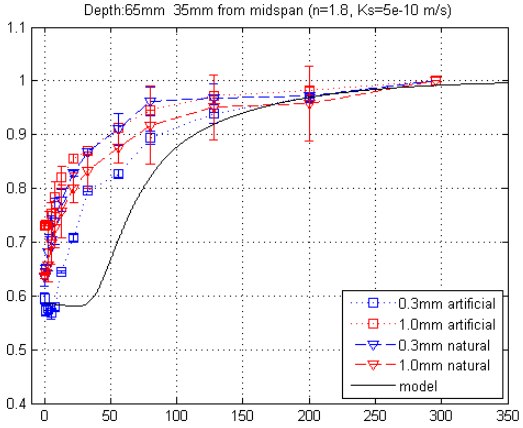

Wetting Ks=5e-10 m/s n=2.2

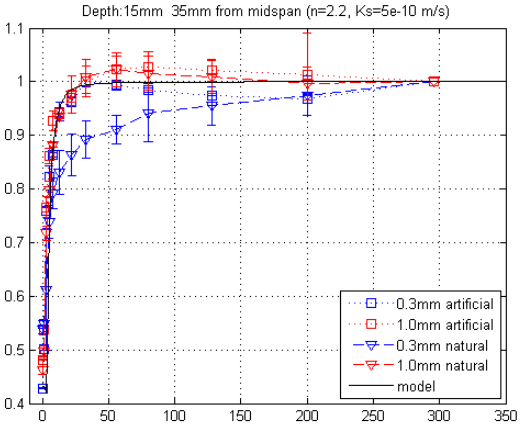

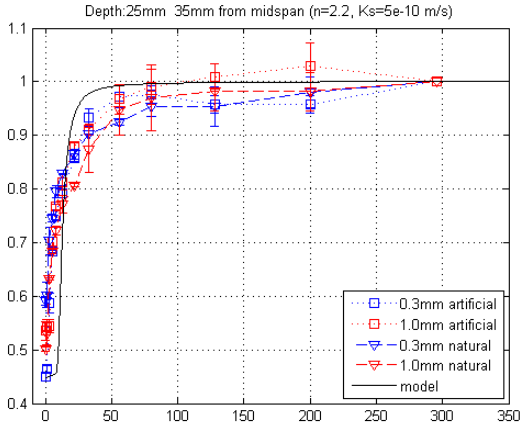

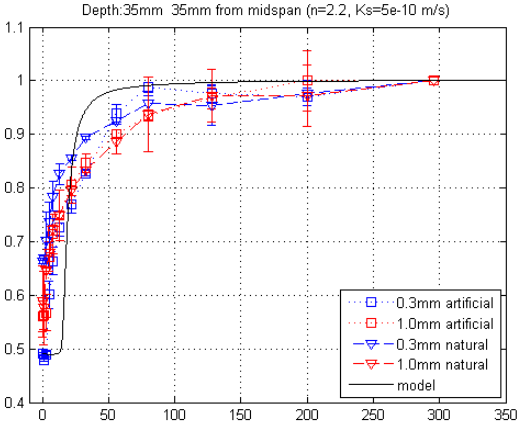

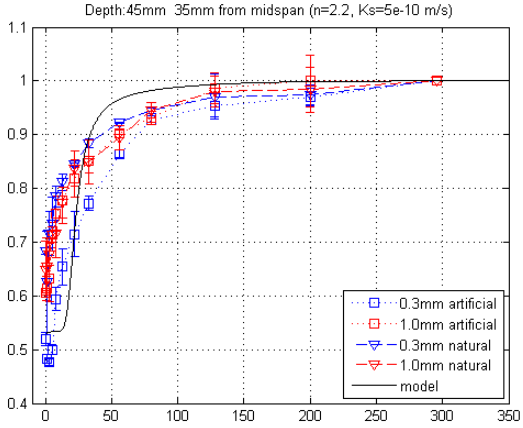

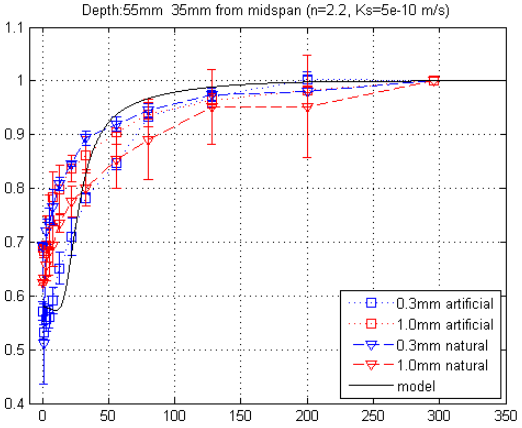

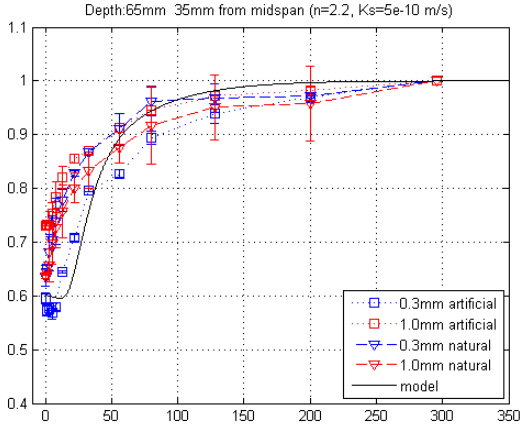

Wetting Ks=5e-10 m/s n=2.0

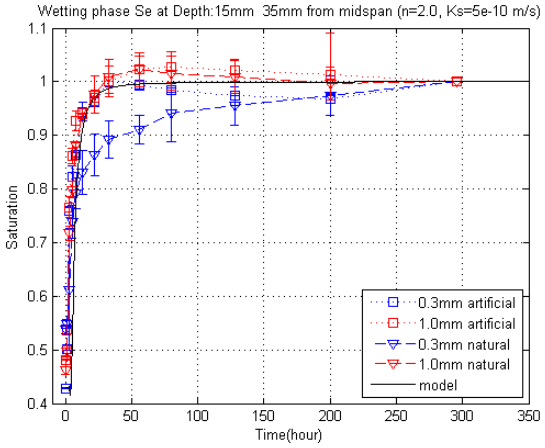

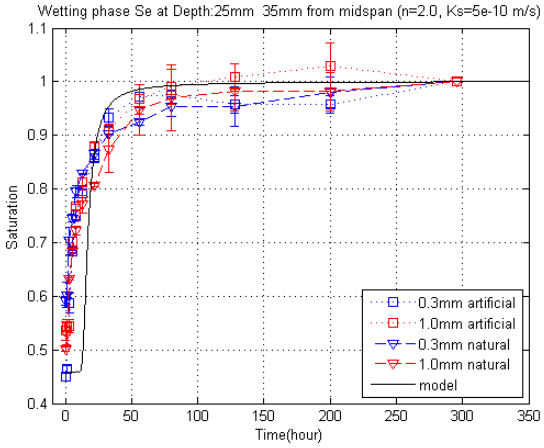

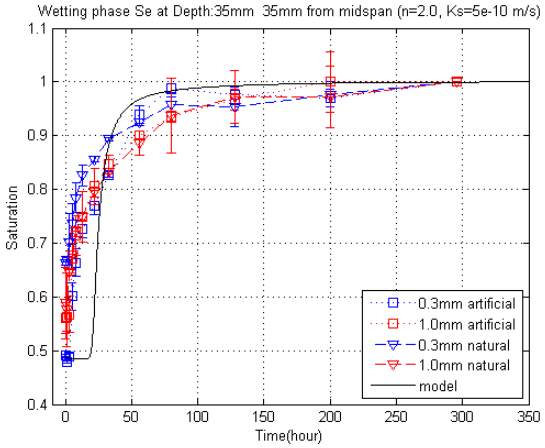

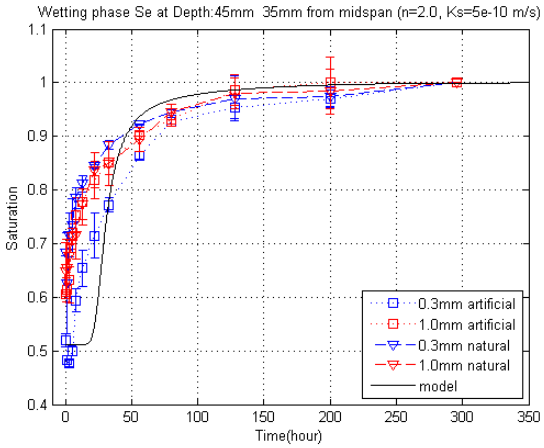

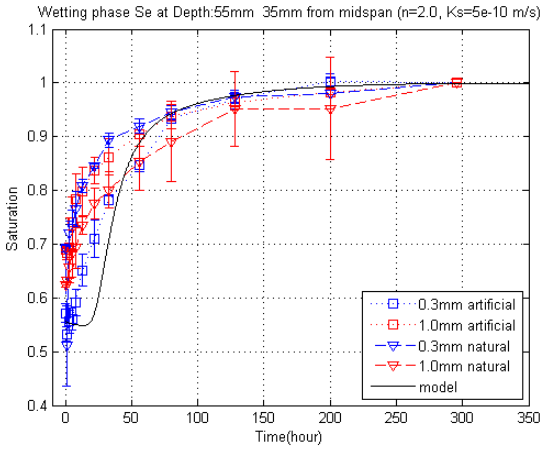

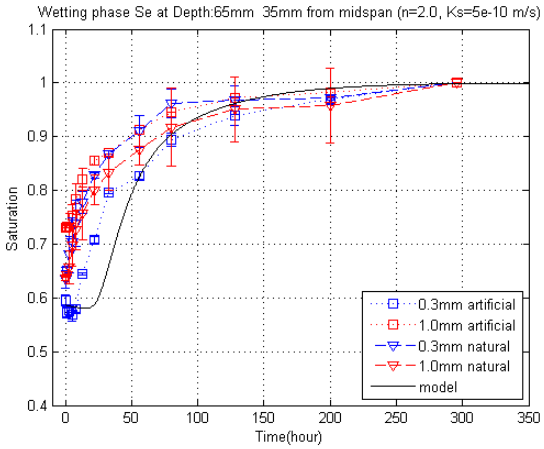

Drying Ks=2e-10 m/s n=1.52

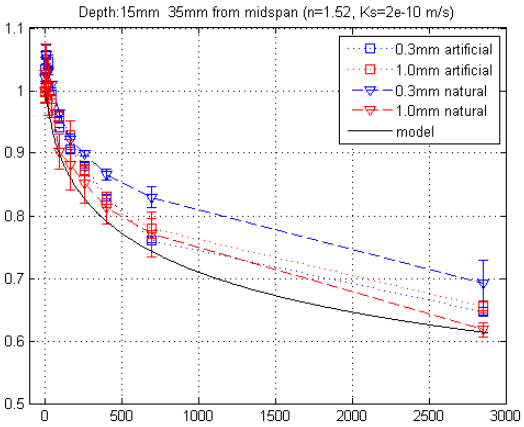

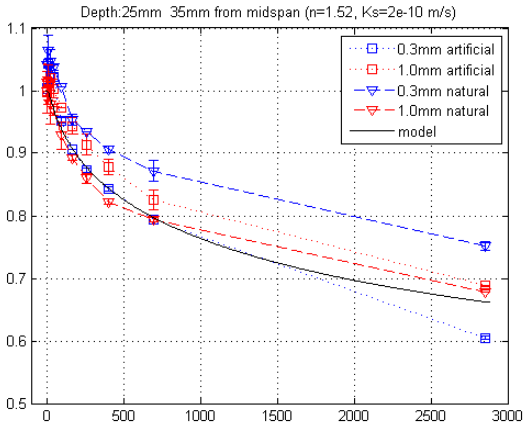

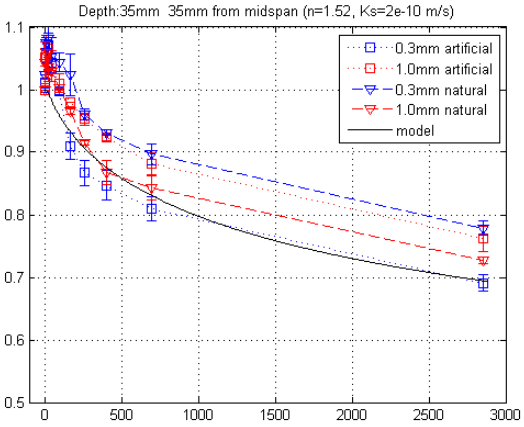

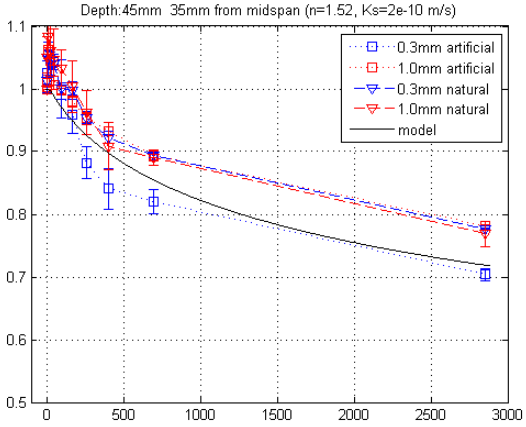

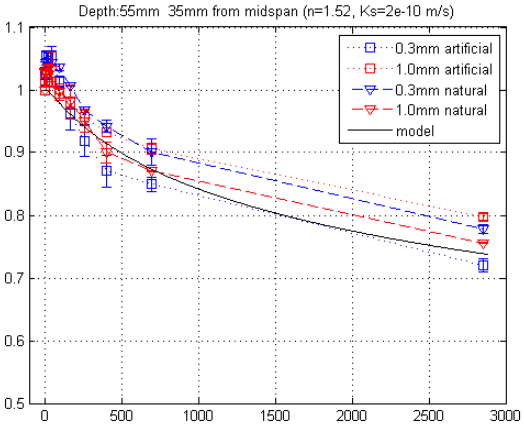

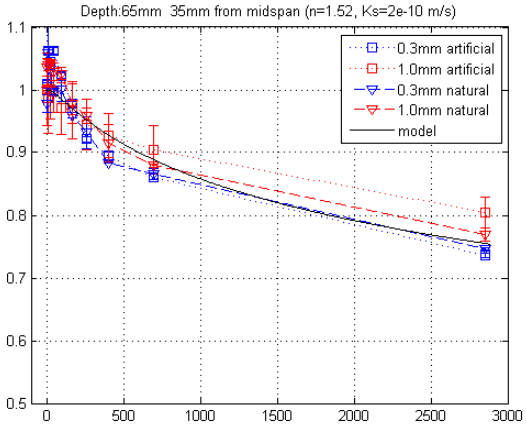

Drying Ks=2e-10 m/s n=1.4

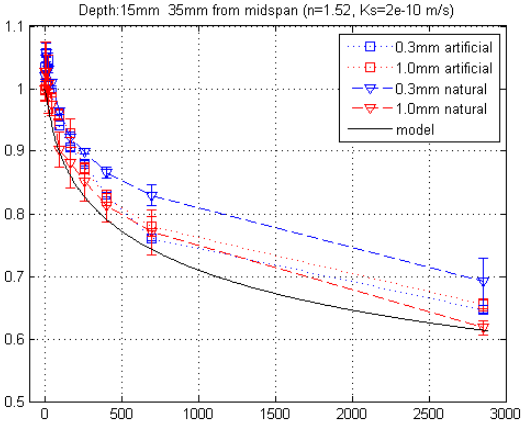

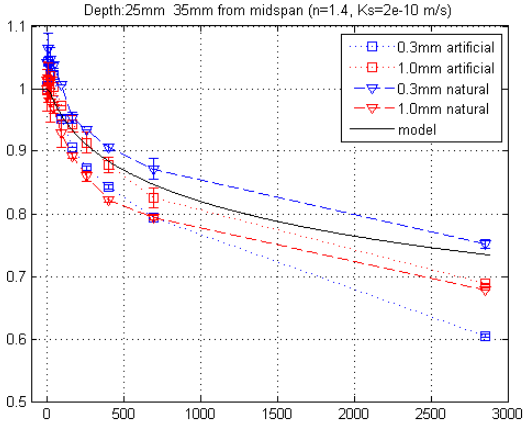

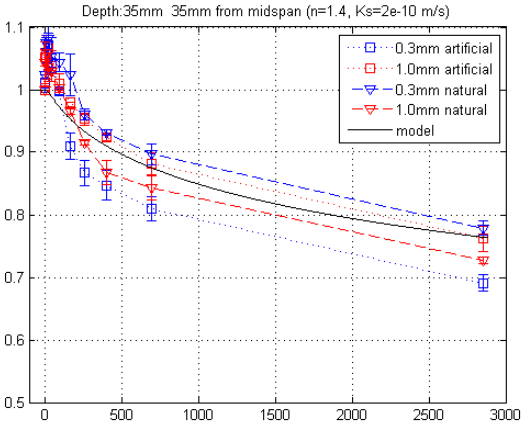

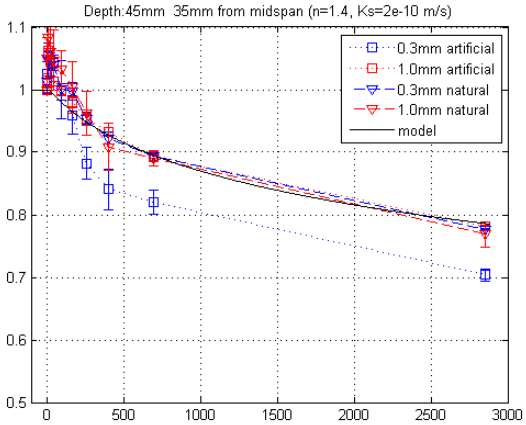

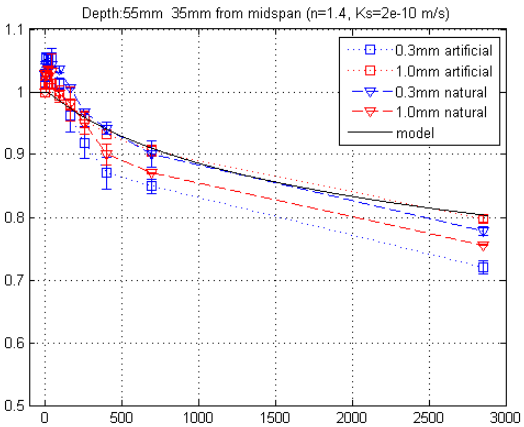

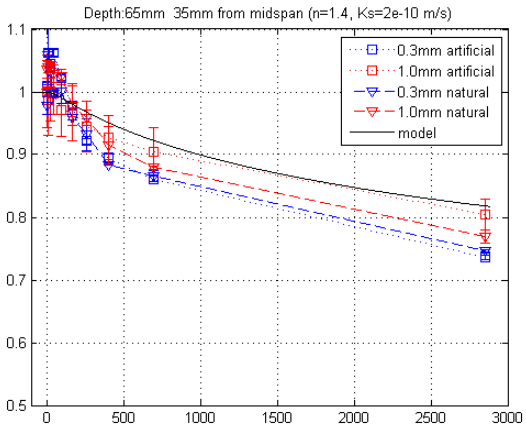

Drying Ks=5e-10 m/s n=1.30

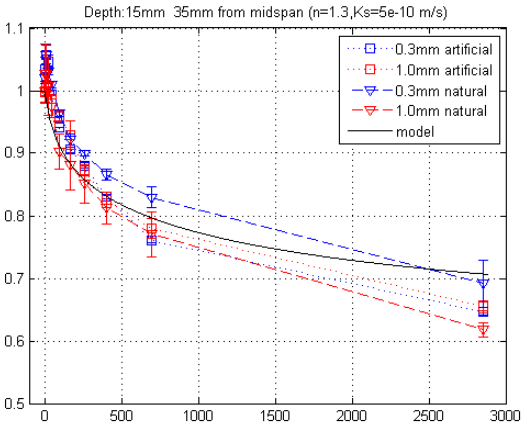

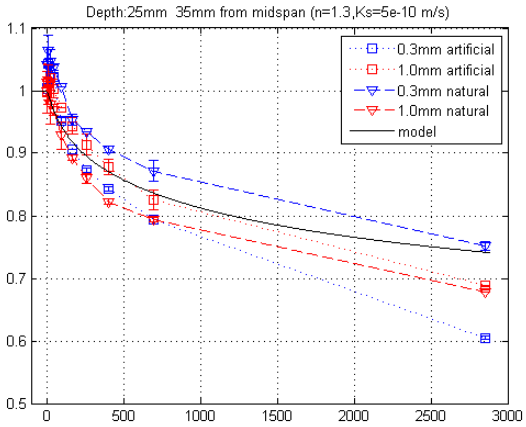

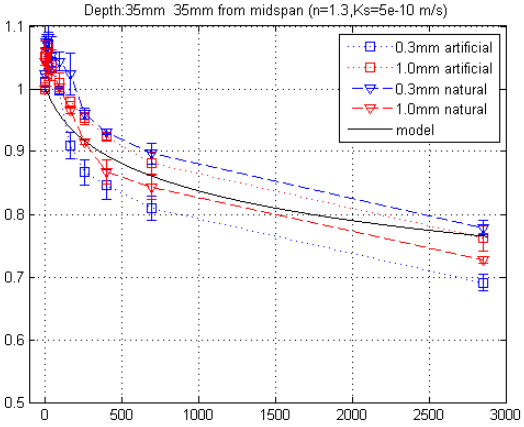

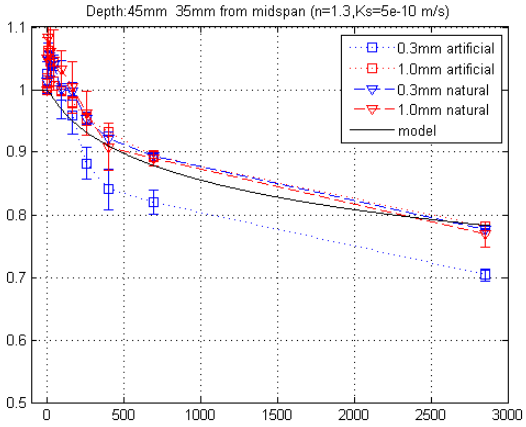

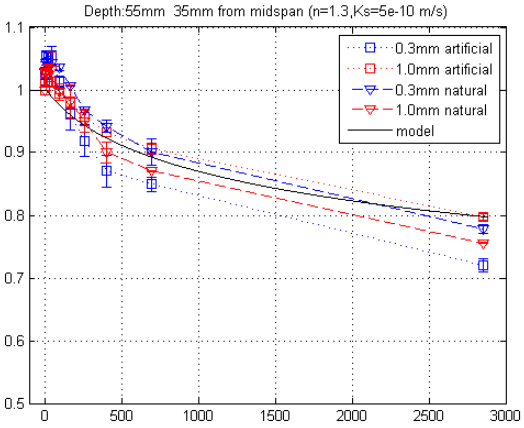

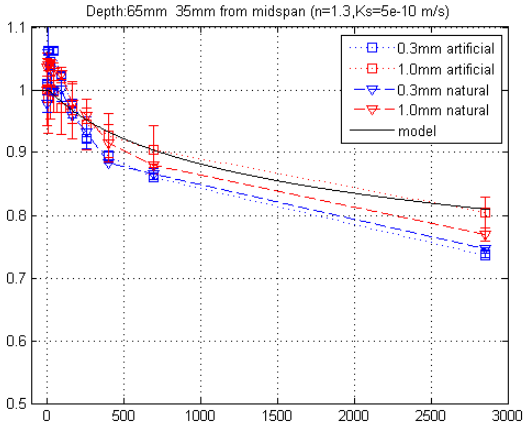

Drying Ks=5e-10 m/s n=1.35

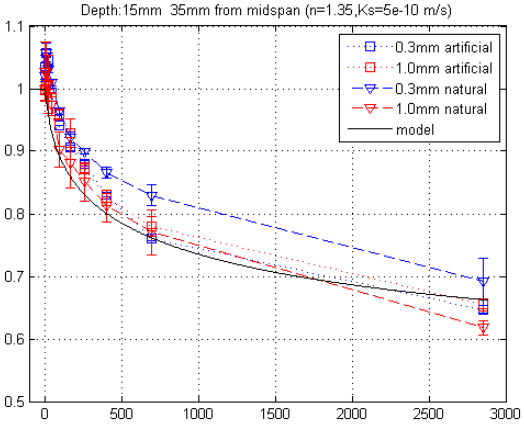

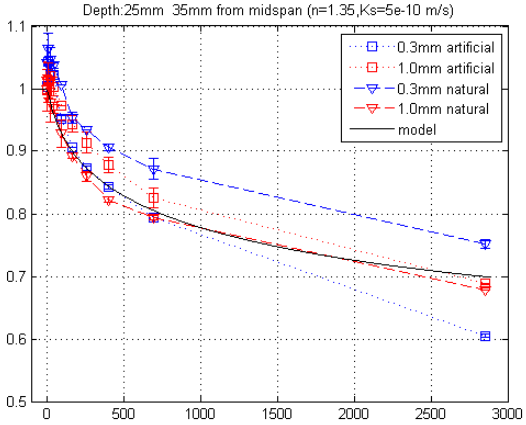

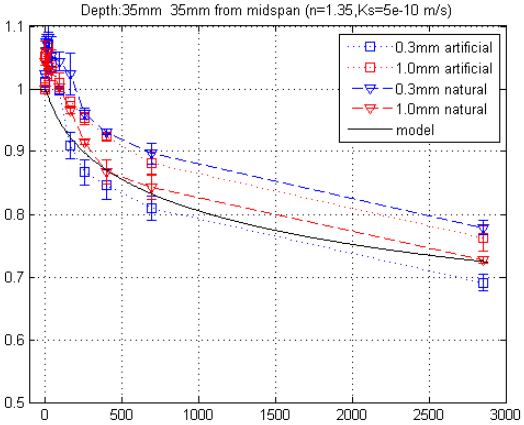

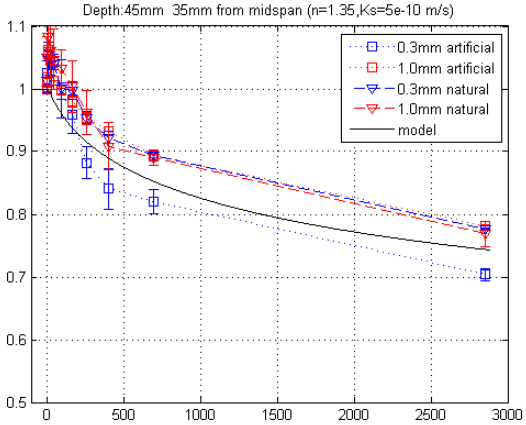

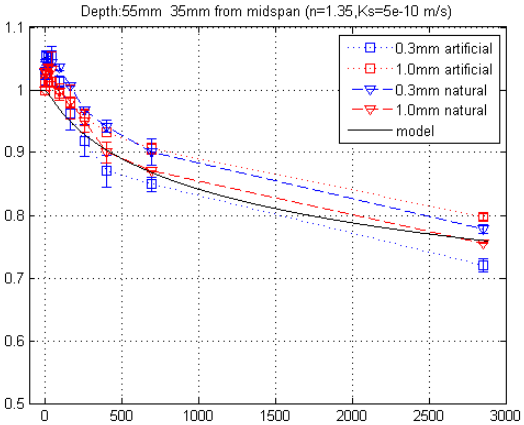

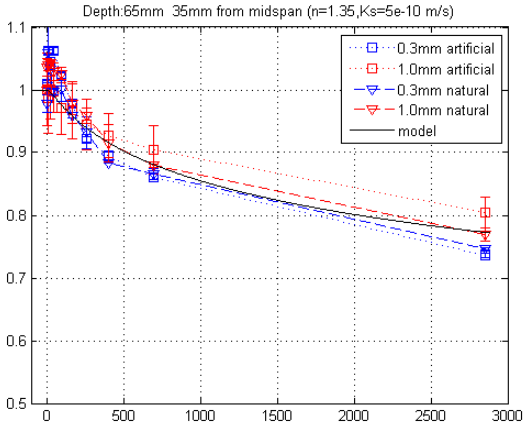

Drying Ks=5e-10 m/s n=1.32